Multiscale characterisation of chimneys/pipes: Fluid escape structures within sedimentary basins

Adam H. Robinson[1*], Ben Callow[1*], Christoph Böttner[2], Naima Yilo[1], Giuseppe Provenzano[1,3], Ismael H. Falcon-Suarez[4], Hector Marin-Moreno[4,5], Anna Lichtschlag[4], Gaye Bayrakci[4], Romina Gehrmann[1], Lou Parkes[6], Ben Roche[1], Umer Saleem[7], Bettina Schramm[2], Malin Waage[8], Aude Lavayssière[1], Jianghui Li[1], Farid Jedari-Eyvazi[1], Sourav Sahoo[4], Christian Deusner[2], Elke Kossel[2], Timothy A. Minshull[1], Christian Berndt[2], Jonathan M. Bull[1], Marcella Dean[9], Rachael H. James[1], Mark Chapman[6], Angus I. Best[4], Stefan Bünz[8], Baixin Chen[7], Douglas P. Connelly[4], Judith Elger[2], Matthias Haeckel[2], Timothy J. Henstock[1], Jens Karstens[2], Calum Macdonald[6], Juerg M. Matter[1], Laurence North[4], Benedict Reinardy[10].

[1]University of Southampton, School of Ocean and Earth Science, Southampton, SO14 3ZH, UK.
[2]GEOMAR Helmholtz-Centre for Ocean Research Kiel, Kiel, Germany.
[3]University of Grenoble Alpes, ISTerre, Grenoble, France.
[4]National Oceanography Centre, Waterfront Campus, Southampton, SO14 3ZH, UK.
[5]Norwegian Geotechnical Institute, PB 3930 Ullevål Stadion, NO-08906 Oslo, Norway.
[6]University of Edinburgh School of Geosciences, Grant Institute, Edinburgh EH9 3JW, UK.
[7]Institute of Mechanical, Process and Energy Engineering, Heriot-Watt University, Edinburgh, EH14 4AS, UK.
[8]UiT The Arctic University of Norway, Department of Geosciences, Tromsø, Norway.
[9]Shell Global Solutions International BV, Grasweg 31, 1031 HW Amsterdam, Netherlands.
[10]Stockholm University and Bolin Centre for Climate Research, Stockholm, Sweden.

*These authors contributed equally

Corresponding authors:
Adam Robinson (A.H.Robinson@soton.ac.uk) and Ben Callow (Ben.Callow@noc.soton.ac.uk)

ABSTRACT

Evaluation of seismic reflection data has identified the presence of fluid escape structures cross-cutting overburden stratigraphy within sedimentary basins globally. Seismically-imaged chimneys/pipes are considered to be possible pathways for fluid flow, which may hydraulically connect deeper strata to the seabed. The properties of fluid migration pathways through the overburden must be constrained to enable secure, long-term subsurface carbon dioxide (CO_2) storage. We have investigated a site of natural active fluid escape in the North Sea, the Scanner pockmark complex, to determine the physical characteristics of focused fluid conduits, and how they control fluid flow. Here we show that a multi-scale, multi-disciplinary experimental approach is required for complete characterisation of fluid escape structures. Geophysical techniques are necessary to resolve fracture geometry and subsurface structure (e.g., multi-frequency seismics) and physical parameters of sediments (e.g., controlled source electromagnetics) across a wide range of length scales (m to km). At smaller (mm to cm) scales, sediment cores were sampled directly and their physical and chemical properties assessed using laboratory-based methods. Numerical modelling approaches bridge the resolution gap, though their validity is dependent on calibration and constraint from field and laboratory experimental data. Further, time-lapse seismic and acoustic methods capable of resolving temporal changes are key for determining fluid flux. Future optimisation of experiment resource use may be facilitated by the installation of permanent seabed infrastructure, and replacement of manual data processing with automated workflows. This study can be used to inform measurement, monitoring and verification workflows that will assist policymaking, regulation, and best practice for CO_2 subsurface storage operations.

Key words: Chimneys, pipes, overburden, CO_2 sequestration, geological storage, North Sea

1   INTRODUCTION

1.1   Overview

Carbon dioxide (CO_2) capture and subsurface storage (CCS) within sedimentary basins has been identified as an effective solution for reducing anthropogenic CO_2 emissions in the atmosphere (IPCC, 2005; The Global CCS Institute, 2019). CCS must form a key component of present and future global climate policy, in order to meet anthropogenic greenhouse gas emission reductions of 80-95% by 2050, and limit model predictions of likely warming of <2°C relative to pre-industrial levels (IPCC, 2014). Requirements for wide-scale implementation of CCS include: 1) cost-effective CCS technologies; 2) government policy/incentives for negative emissions technologies; and 3) the need for public acceptance/confidence, all of which are intrinsically linked. The primary technological requirement to widespread implementation of CO_2 storage is subsurface site characterisation and containment assurance. Legal regulations governing CCS in Europe exist in the form of the EU CCS Directive on Geological Storage of Carbon Dioxide 2009/31/EC (2009), which defines requirements for CO_2 storage across the lifetime of a storage site, including closure and post-closure obligations. Factors that must be considered for the characterisation and assessment of potential CO_2 storage complexes and their surroundings include the role and impacts of potential fluid migration pathways causing loss of containment, and the potential flux rates through these pathways.

CO_2 can be sequestered into porous and permeable subsurface sandstone reservoirs (Bachu, 2000; Benson and Cole, 2008), such as depleted oil and gas reservoirs and saline aquifers. Sandstone reservoirs of this type are commonly overlain by impermeable cap rocks and overburden stratigraphy, which together provide an effective seal that prevents the upward migration of CO_2, ensuring safe and permanent storage. Offshore CO_2 storage in sandstone reservoirs has been successfully demonstrated in Europe and globally (e.g., Sleipner, North Sea; Tomakomi, Japan). Several other commercial-scale offshore CO_2 storage projects are also in planning or development stages, such as the Northern Lights project (e.g., Furre et al., 2019a; Global CCS Institute, 2019).

The location and potential intensity of any possible loss of CO_2 containment from a storage reservoir is dependent on the distribution of fluid pathways in the cap rock and overburden, and the ability of these pathways to transmit dissolved, liquid, and/or gaseous CO_2, depending on the pressure-temperature conditions and presence of other fluids. Potential pathways may include anthropogenic sources, such as abandoned wells (e.g., Watson & Bachu, 2009), formation level inherent structures, including natural migration up-dip along permeable stratigraphic horizons (e.g., Tóth, 1980; Hindle, 1997), and the formation or reactivation of fluid escape structures (e.g., Nichols et al., 1994; Frey et al., 2009). Such fluid escape, or seal bypass, structures permit pressure-driven, focused fluid flow, which hydraulically connects deeper strata with the seafloor through inter-connected faults, fractures and porous-permeable sediment layers (Cartwright et al., 2007). Fluid escape can take place as single blow-out events, episodic/pulsed flow, or as continuous seepage flow. The type of flow can vary depending on the subsurface pressure, stress and lithological conditions. Therefore, the activity of a fluid escape structure may exhibit temporal variability, which may be cyclical over both short timescales such as tidal cycles (e.g., Boles et al., 2001) or longer-term sea level changes (e.g., Plaza-Faverola et al., 2011; Riboulot et al., 2014). Therefore, the combined understanding of the presence of fluid pathways and their fluid flow regime is critical for the risk assessment of potential subsurface CO_2 escape.

1.2   Aims & objectives

In this contribution we provide a broad overview of the integrated geophysical, geological and geochemical methods which can be applied to the characterisation of focused fluid conduits. In order to achieve this, we use as our context an examplar study of the fluid conduit beneath the Scanner pockmark, which we undertook as part of the European Union Horizon 2020 project **S**trategies for the **E**nvironmental **M**onitoring of **M**arine **C**arbon **C**apture and **S**torage (STEMM-CCS; http://www.stemm-ccs.eu), together with a partner project CHIMNEY (**Ch**aracter**i**sation of **m**ajor overburde**n** **le**akage pathwa**y**s above sub-seafloor CO_2 storage reservoirs in the North Sea; Bull et al., 2018). STEMM-CCS and CHIMNEY focussed on determining the permeability of subsurface fluid pathways, and developing better techniques to locate fluid escape structures, so that they can be better quantified and constrained, with relevance to potential fluid flow at CO_2 storage complexes.

The paper has three main aims: (1) Firstly, we describe the various methods which may be applied to the characterisation of focused fluid conduits, and which allow us to resolve the physical parameters of interest (Section 3). For each individual method, we describe their capabilities, consider their benefits, address uncertainties, and deduce any further developments that may be required. In order to contextualise the various techniques which may be used, we describe their application during our investigation of the Scanner pockmark. (2) Secondly, we discuss the scales of imaging and resolution of the various methods described here, and the co-dependencies which exist between them. This permits integration into a multi-scale approach, and demonstrates how the different techniques may be employed in combination, to ensure appropriate constraint and calibration of the different methods, for complete characterisation of the fluid escape structures (Section 4). (3) Thirdly, based on our findings from this study, we describe a framework which can be used to determine the approaches that are needed to understand potential fluid flow structures in marine environments, in the context of the risk assessment of potential future CO_2 geological storage sites (Section 5).

2   GEOLOGICAL BACKGROUND

2.1   Focused fluid conduits in seismic data

Seismic chimneys (e.g., Hustoft et al., 2010) or pipes (e.g., Moss & Cartwright, 2010a), referred to hereafter only as chimneys, are observed in seismic reflection data as vertical to sub-vertical anomalies with circular or elliptical planforms, displaying seismic blanking and discontinuous or chaotic reflections (e.g., Løseth et al., 2011). Where free gas is present in the chimney, high amplitude seismic

reflections, known as bright spots, with polarity reversals may be observed at discrete intervals, indicating gas accumulation during migration in layers of porous sediments (e.g., Ostrander, 1984). Pull-up of reflectors may also be observed, caused by high seismic velocities, which are commonly attributed to authigenic carbonate accumulations, or where located in the gas hydrate stability zone, to the presence of gas hydrate (e.g., Plaza-Faverola et al., 2010). If CO_2 migrates from a sub-seafloor storage reservoir and reaches the base of these chimneys, and if their permeability is sufficiently high, they could act as CO_2 pathways towards the seafloor and overlying water column. To provide a reliable prediction of potential seafloor seep sites, the degree to which these pathways are able to transmit fluids (i.e. permeability) needs to be better understood.

Chimneys have been globally observed by seismic imaging (e.g., Cartwright et al., 2007; Gay et al., 2007; Moss & Cartwright, 2010a,b; Løseth et al., 2011; Plaza-Faverola et al., 2017), including extensively in the North Sea (Hovland & Sommerville, 1985; Cole et al., 2000; Bünz et al., 2003; Karstens & Berndt, 2015; Böttner et al., 2019). A comprehensive analysis of 3D seismic reflection volumes in the South Viking Graben, North Sea (an area of 2850 km^2; Karstens & Berndt, 2015) identified 46 large-scale (~100-1000 m-wide) chimneys within the shallowest 1000 m of the overburden.

Chimney-like features can also be the result of seismic imaging artefacts. Seismic imaging artefacts may arise both as a result of data acquisition and/or processing (e.g., Tucker & Yorston, 1973). In particular, for locations where gas is present in the subsurface, the effect this has on seismic velocity determination can have a significant impact on both time and depth migration. An example locality where a seismic artefact was interpreted as a chimney is the Goldeneye field, a prospective CO_2 storage site in the Central North Sea. Following high resolution 3D seismic processing, a feature previously interpreted as a fluid escape conduit was later reinterpreted as a seismic imaging artefact caused by a glacial tunnel valley (Dean et al., 2015; Karstens and Berndt, 2015).

2.2   Formation of chimneys

Chimney formation was observed on a small scale during a controlled subsurface CO_2 release experiment known as QICS (Taylor et al., 2015; Cevatoglu et al., 2015). In this experiment, CO_2 was released into sediments at an increasing rate of 20 to 210 kg/day, at 12 m depth below the seabed in shallow water (5-30 m) in Ardmucknish Bay, Scotland. Repeated seismic reflection data acquisition prior to, during, and after the gas release showed the temporal development of a chimney, formed by gas propagating upwards by fracture generation and reactivation in fine grained sediment (Cevatoglu et al., 2015). Conditions for hydraulic fracture generation are favourable in shallow (low effective stress) unconsolidated, fine grained sediments, and may be considered a primary mechanism for chimney initiation (Fauria & Rempel, 2011). The upward propagation of fluids may also be facilitated by capillary driven invasion, most prevalent in conditions of high effective stress (Cathles et al., 2010). Further mechanisms for chimney genesis include: erosive fluidisation, localised subsurface volume loss and syn-sedimentary formation (Lowe, 1975; Sun et al., 2013; Cartwright & Santamarina, 2015).

Based on the observations from QICS, and other experiments (e.g., Fauria & Rempel, 2011; Räss et al., 2018), a conceptual model for the formation mechanism and structure of chimneys in the shallow overburden has been developed (Bull et al., 2018). In this model, the first phase of formation is the hydraulic fracturing of low permeability sediments due to high fluid overpressure (Arntsen et al., 2007; Cartwright et al., 2007; Løseth et al., 2009). Seal breaching occurs due to reduced effective stress and leads to either opening of new fractures and/or reactivation of pre-existing fractures, generating a localised connected fracture system. These pathways may permit vertical buoyancy-driven migration of gas-rich pore fluids through the fracture network. Large-scale chimneys (~100-1000 m wide) are therefore hypothesised to represent a series of interconnected sub-vertical or radial fractures, which allow the vertical flow of gas in the shallow subsurface (Bull et al., 2018) due to the elevated

173 permeability relative to the normal 'background' permeability of the host sediment (Cartwright et al.,
174 2007). A transition from fracture to capillary dominant flow behaviour may be observed with increasing
175 depth, due to increased overburden thickness (higher effective stress).
176   In addition to the role of the geometric structures of chimneys in governing fluid flow, coupled
177 physical and chemical processes act within fractures and pores, resulting in complex feedback
178 mechanisms between porosity-permeability and CO_2/CH_4 reactivity, which may affect the hydro-
179 mechanical response of the system. From a quantitative perspective, little is known regarding the impact
180 that chimneys have on the upwards migration of CO_2 and CH_4 to the seabed (Liu et al., 2019; Marin-
181 Moreno et al., 2019).
182
183 **2.3   Study area – Scanner pockmark**
184 We have investigated an exemplar natural fluid escape system located near the centre of the Witch
185 Ground Basin, located 190 km off the north-east coast of Scotland (Fig. 1a), within licence block 15/25
186 of the North Sea. Here, chimneys are observed, which underlie active natural methane venting sites at
187 the seabed, within ~150 m water depth (Fig. 1b) - the Scanner, Challenger and Scotia pockmark
188 complexes (Gafeira and Long, 2015). Pockmarks are seabed depressions, created by release of over-
189 pressured pore-water and gas from the subsurface (Hovland et al., 2010). In this area of the North Sea,
190 large pockmarks (>6 m deep, >250 m long, and >75 m wide; class 1, Böttner et al., 2019) are
191 continuously active. Evidence for active methane venting at the Scanner pockmark complex is provided
192 by water column imaging and the presence of methane derived authigenic carbonates (MDACs) at the
193 seabed (Judd et al., 1994; Judd & Hovland, 2009). The West Scanner pockmark (Fig. 1c) releases
194 methane at 1600-2600 kg/day (Li et al., in review), derived from a combination of biogenic and
195 thermogenic sources (Clayton & Dando, 1996). Smaller pockmarks (class 2) are also distributed across
196 the area (Fig. 1b) with a dominant NNE/SSW orientation (>1500 across 225 km^2) and are interpreted
197 as dewatering features attributed to localised pressure changes (Böttner et al., 2019). The Scanner
198 pockmark complex overlies an area that has been appraised for CO_2 storage potential, the East Mey
199 Storage Site (ACT Acorn Consortium, 2018).
200
201 *2.3.1   Stratigraphy and seismostratigraphic framework*
202 The lithostratigraphy and seismostratigraphic framework of the ~600 m-thick Quaternary sediment
203 succession containing the Scanner pockmark complex was described by Böttner et al. (2019) and Stoker
204 et al. (2011) (Fig. 2). Deposited within the Witch Ground Basin (Andrews et al., 1990), this complex is
205 underlain by the Hordland and Nordland Groups, of Palaeogene and Neogene age respectively, and
206 which are composed of claystone with limestone and sandstone interbeds (Judd et al.,1994).
207   The basal Quaternary unit, the Aberdeen Ground Formation (Fm.; unit S1 in Figure 2), is
208 composed of clay-rich sediments deposited in the Early Pleistocene (up to Marine Isotope Stage, MIS,
209 13), and displays a laterally continuous, layered seismic character (Stoker et al., 2011; Ottesen et al.,
210 2014). The overlying Ling Bank Fm. (S2) erodes into the top of the Aberdeen Ground Fm., representing
211 a regional glacial unconformity, with deposition of glacial tills in the Early to Middle Pleistocene (~1.2-
212 0.5 Ma, MIS 12 to 10; Stewart & Lonergan, 2011; Reinardy et al., 2017; Böttner et al. 2019). The glacial
213 tunnel valleys of the Ling Bank Fm. display both a layered and non-layered seismic character. The Coal
214 Pit Fm. (S3) overlies the Ling Bank and Aberdeen Ground Fms., and comprises glacial tills (which
215 include pebbly and muddy sands) deposited in the Upper mid to Late Pleistocene (MIS 6-3; Andrews
216 et al., 1990; Stoker et al., 2011). The Coal Pit Fm. is conformably overlain by Last Glacial Maximum
217 (LGM) deposits, which comprises silty-sandy clays with rare pebbles, deposited during MIS 3-2 (S4).
218 Unit S4 extends upwards to the base of Scanner pockmark. The Coal Pit Fm. and LGM deposits have
219 a dim and chaotic seismic character and are conformably overlain by the Witch Ground Fm. (S5),

composed of silty clay deposited during MIS 2 to 1 (Stoker et al., 2011). The Witch Ground Fm. has two main units: the lower (S5.1) and upper (S5.2) Witch Ground Member respectively. The lower Witch Ground Member has an apparent interbedded seismic character. The upper Witch Ground Member conformably overlies the lower Witch Ground Member, thinning or pinching out towards the northeast. The upper Witch Ground Member is composed of sediments of Holocene age (MIS 1) and has a uniform seismic character (Stoker et al., 2011). The Scanner pockmark depression erodes down to the base of the lower Witch Ground Member.

3 OVERVIEW OF CHIMNEY CHARACTERISATION METHODS

3.1 Overview & data acquisition

The methods used to investigate chimneys and their associated fluid flow can be divided into several types (Table 1). These include: seismic reflection imaging, ocean-bottom seismic methods, including seismic tomography and anisotropy analysis, controlled source electromagnetic surveying (CSEM), active and passive acoustics, sediment sampling of both the target site and onshore analogues, laboratory rock physics experiments, and process-based numerical modelling and fluid dynamic modelling approaches.

In support of the STEMM-CCS and CHIMNEY projects, four research expeditions were undertaken for data collection at the Scanner pockmark complex. 2D seismic reflection and refraction data, for use in travel time tomography, were acquired using a GI gun source and 18 ocean bottom seismographs (OBS) by RV Maria S Merian cruise MSM63 (Fig. 3a,d; Berndt et al., 2017), in addition to multi-beam bathymetry data, controlled source electromagnetic (CSEM) data (Fig. 5), and Parasound sub-bottom profiling data (Fig. 2a). RRS James Cook cruise JC152 conducted a wide-ranging seismic experiment over the Scanner and Challenger pockmarks (Figs. 3 & 4). Five different seismic sources were used (Bolt and GI airguns, Squid and Duraspark surface sparkers, and a deep towed sparker; Fig. 3), which were recorded by arrays of 25 and 7 OBSs, at the Scanner and Challenger pockmarks, respectively (Fig 3a; Bull, 2017). The seismic sources were also used to generate multichannel (GI guns, surface sparkers; Fig. 2b) and single channel (deep tow sparker) seismic reflection profiles. During cruise MSM78 (Karstens et al., 2019) and RV Poseidon POS518-2 (Linke & Haeckel, 2018), sediment cores for geological and geochemical analysis were taken from within the Scanner pockmark and a reference site (Fig. 1b,c) using a gravity corer and rock drill (RD2) which acquired core to depths of ~6 and ~33 metres below seafloor (mbsf), respectively. Additionally, data from a 3D seismic survey conducted by PGS (Fig. 2c; CNS Mega Survey Plus) were used to further support the study.

3.2 Seismic reflection methods

3.2.1 *Introduction*

Multichannel seismic reflection data record the wavefield reflected from physical discontinuities in the subsurface at a range of distances from an active source of acoustic energy. By doing so, they carry information about seismic wave propagation velocity and anomalies in visco-elastic properties. So long as the geological boundaries correspond to changes in physical properties controlling seismic wave propagation, reflection data imaging provides us with a representation of subsurface sedimentary and tectonic structures with a resolution equal to a fraction of the propagated wavelength (Kallweit & Wood, 1982). Sub-vertical fluid escape structures and sediment deformation (e.g., sediment mobilisation and polygonal faulting) can therefore be imaged, potentially also allowing for a relative dating of geological events by interpreting cross-cutting structures and stratal stacking patterns.

Changes in pore fluid type, especially partial gas saturation, have a strong influence on seismic velocities and the absorption of seismic wave energy (White, 1975; Domenico, 1977). The bulk effect of gas accumulation within sediment pores is a reduction in the sediment compressibility and, therefore,

267 acoustic impedance (Tóth et al., 2014). Typically this results in strong acoustic impedance contrasts,
268 visible in the seismic data as negative polarity reflections known as bright spots (Cevatoglu et al., 2015).
269 More generally, pore gas manifests itself as local increments in the subsurface reflectivity, as a function
270 of the properties of the encasing medium and the local partial gas saturation (Berndt, 2005; Cartwright,
271 2007; Løseth et al., 2009; Andresen, 2012; Karstens & Berndt, 2015). Frequency-dependent attenuation
272 and velocity dispersion can also be observed in ultra-high-frequency (in the order of kHz) data, as the
273 seismic frequency approaches the gas bubble characteristic frequency, allowing the detection of gas
274 migration irrespective of the presence of reflective anomalies (Tóth et al., 2015). Therefore, not only
275 do reflection data allow us to image potential gas migration pathways in the subsurface, but also to
276 detect gas accumulation pockets and potentially quantify their volume.

277 However, as a consequence of the strong energy partitioning at the interface with gas-charged
278 sediments, acoustic blanking may be observed within chimneys (Fig. 2b,c; Davis et al., 1997), which
279 hampers the effectiveness of seismic reflection imaging and inversion in such contexts. As a result,
280 wide-angle transmission data recorded at the seabed, for example on OBS, may also be required, in
281 order to characterise seismic velocities below the gas layer. Wide-angle transmission also helps resolve
282 the issue of ambiguity between the position of the reflector and the true interval velocity along the
283 wave-path, since the short offset range and the limited bandwidth of seismic reflection data result in a
284 limited sensitivity to interval velocities (Jannane et al., 1989). Therefore, integration with diving wave
285 travel time tomography, in addition to reflection waveform inversion techniques (e.g., Brossier et al.,
286 2015) and seismic-to-well calibration are necessary to compensate for the lack of sensitivity to the
287 kinematic properties of the medium, and provide an accurate depth representation.

288

289 *3.2.2   2D vs 3D seismic reflection*
290 Two-dimensional (2D) seismic imaging assumes that subsurface properties are invariant with respect
291 to the direction normal to the survey line. In the case of inherently three-dimensional structures, such
292 as pockmarks and chimneys, this assumption represents a potentially significant source of error. Whilst
293 a chimney can be assumed, in a simple case, to be radially symmetrical around the depth axis, there
294 potentially may be out-of-plane reflections that affect imaging. Three-dimensional (3D) seismic data
295 have substantially advanced the knowledge of subsurface fluid migration features, which were
296 previously often discarded as poorly imaged zones and seismic artifacts in 2D seismic data (Cartwright
297 & Huuse, 2005). The analysis of 3D seismic data is an effective method to map fluid accumulations in
298 the subsurface, identify permeability barriers and constrain subsurface geometries of entire fluid flow
299 systems (Cartwright et al., 2007; Løseth et al., 2009; Andresen, 2012; Karstens & Berndt, 2015). Where
300 only 2D seismic data are available, application of 3D processing of 2D acquisition geometries (e.g., Lin
301 et al., 2019) has proved extremely useful for improving the quality of the final results, provided that
302 variations of the streamer position during acquisition are monitored within the desired accuracy
303 (Whiteside et al., 2013) or estimated from the data (Clay & Vardy, 2018).

304 However, the resolution of conventional seismic data, laterally (often above 12.5 m) and
305 vertically (~10 m for a dominant frequency of 40 Hz), is often not sufficient to image the seismic
306 expression of fluid flow systems in detail. Recent developments in 3D high-resolution seismic
307 techniques allow imaging of the shallow subsurface in much greater detail than previously (e.g., Planke
308 et al., 2009; Petersen et al., 2010; Plaza-Faverola et al., 2015). An example technology is the P-Cable
309 (e.g., Planke et al., 2009), which has been used to map shallow gas accumulations, gas hydrate systems,
310 and fluid flow structures, such as chimneys (e.g., Plaza-Faverola et al., 2011; Bünz et al., 2012) down
311 to a resolution of 3 m. In contrast to conventional seismic frequencies of ~5–120 Hz (suitable for
312 monitoring deep reservoirs), high resolution P-Cable uses frequencies of up to 350 Hz, surpassing the
313 resolution of conventional 3D seismic.

Collectively, the seismic experiments conducted at the Scanner pockmark complex utilise different imaging resolutions and depths, by applying a multiple-frequency 2D surveying approach, using a number of seismic sources (Fig. 3b; Bull et al., 2018). Progressive extension of the seismic bandwidth to higher frequencies and shorter shot intervals results in higher vertical and lateral resolution. Surface sparker, deep towed sparker and sub-bottom profiler data (the latter is single-channel, and may be considered a hydro-acoustic technique, but we include it here with the other seismic approaches as it is used for the same purpose) with frequencies up to several kHz reveal near surface structural features previously not discernable using lower frequency sources, such as sediment slumping/flank collapse within the pockmark, and more detailed characterisation of gas accumulation at the top of the Aberdeen Ground Fm. and direct observation of fluid migration towards the base of the pockmark (Fig. 3a,b). Therefore, multi-frequency surveys with different sources (e.g., Bolt Gun, GI Gun, Chirp, Boomer, and Sparker) and high-resolution 2D or P-cable streamers can complement conventional 3D seismic data (e.g. Fig. 3c) and lead to a better understanding of the nature and internal architecture of chimneys, particularly in the shallow overburden stratigraphy.

3.2.3   *Advanced seismic wavefield analysis*

In addition to providing reflectivity images of the subsurface, multi-channel seismic data attributes, such as amplitude as a function of offset, can also be exploited to infer kinematic and dynamic properties of the subsurface (Ostrander, 1984). Pre-stack waveform inversion techniques (Virieux & Operto, 2009) can be applied to obtain quantitative characterisation of the effect of partial gas saturation on the elastic properties (P-wave velocities and Poisson's ratio). In particular, partial gas saturation has a strong effect on bulk modulus, associated with a relatively low influence on shear modulus, which corresponds to a lowering in P-wave impedance and a reduction of V_p/V_s ratio (Ostrander, 1984; Tóth et al., 2014; Provenzano et al., 2018). These contrasts can in turn be exploited to quantify gas accumulation using appropriately calibrated rock-physics models (Tóth et al., 2014; Provenzano et al., 2018).

3.2.4   *Time-lapse/4D seismic reflection*

Time-lapse seismic imaging refers to the acquisition of seismic data at the same location at different points in time, in order to assess temporal changes in the subsurface. Where both seismic datasets are 3D, this may be referred to as 4D seismic imaging. This technique has been applied extensively to subsurface reservoir monitoring, including conventional and unconventional hydrocarbon production (e.g., Watts et al., 1996; Landrø et al., 1999; Barkved et al., 2003). Changes in the subsurface due to fluid flow may change properties such as fluid saturation, temperature, porosity and pressure, and hence the elastic and stress-strain properties and behaviour of the rock, which cause a change in seismic response (Johnston, 2013). Such temporal changes can be used to better understand the formation and development of fluid flow features, as well as providing constraints for multiphase thermo-hydro-mechanical simulations. Recognising temporal changes in subsurface fluid flow systems is integral for monitoring CO_2 storage reservoirs and potential leakage in the overburden.

A principal challenge in time-lapse/4D seismic surveying is accounting for the repeatability, such that the produced images represent true temporal changes and not seismic artefacts associated with acquisition and/or processing. Attributes such as the normalised root-mean square noise are used to measure quantitatively the quality of the survey repeatability. Generally, repeatability is excellent where sediments are well stratified and undisturbed (e.g., Waage et al., 2019). However, since chimneys are often much more chaotic seismic structures, repeatability can be poor, and detection of changes in fluid flow between individual time-lapse surveys requires careful interpretation (Waage et al., 2019).

Time-lapse and/or 4D seismic data were not acquired at the Scanner pockmark complex. This technique has, however, been applied to the studies of actively-seeping chimneys, such as at Lomvi

pockmark on the Vestnesa Ridge, offshore W Svalbard (Bünz et al., 2012; Smith et al., 2014; Panieri et al., 2017), and for experimental fluid injections, including the Sleipner storage site (e.g., Arts et al., 2004; Chadwick et al., 2004, 2019; Boait et al., 2012; Eiken, 2019), the QICS experiment (Cevatoglu et al., 2015) and the STEMM-CCS Goldeneye release experiment (Flohr & Schapp et al., this volume; Roche et al., this volume). Time-lapse seismic data therefore play a key role in the understanding of both naturally occurring fluid flow, and CCS monitoring in pre-, active and post-CO_2 injection phases (Lumley, 2010).

3.3   Seismic tomography and full waveform inversion

The P- and S-wave velocity structure of a chimney and its surroundings can be determined by applying travel time tomography and full waveform seismic inversion. These techniques are applied with the principal aims of: locating gas-bearing zones; delineating the shape of the chimney; determining the presence and features of fractures (open or cemented, size and connectivity); and characterising the sediment properties within and outside the chimney.

Seismic travel time tomography is an inversion technique in which observed travel times (e.g., Fig. 4b) are compared to those computed through a discretised and parameterised model representation of the subsurface, with defined parameters that control the balance between minimising the data misfit and generating a model with the minimum required structure to fit the data. Travel time tomography approaches may be isotropic (e.g. Zelt & Barton, 1998) or anisotropic (e.g. Dunn et al., 2005), where in the latter the direction and magnitude of velocity anisotropy is fit and calculated directly, whereas in the former the anisotropy manifests as travel time residuals which can be analysed to determine the model anisotropic properties (Dunn & Toomey, 2001). Travel time tomography is a relatively low-resolution (normally hundreds of m to km laterally, hundreds of m vertically) imaging technique, with the resolution ultimately controlled by the shot and receiver spacings and further being dictated by the discretisation and parameterisation of the model.

The final OBS tomography model can be used as the initial model for full waveform inversion of OBS data (FWI; e.g., Virieux & Operto, 2009). FWI uses the entire recorded seismograms, and, therefore, includes amplitude and phase information instead of solely using the travel times. As a result, FWI represents a higher resolution technique, which is now widely used in crustal-tectonic (e.g., Morgan et al., 2013; Górszczyk et al., 2017; Davy et al., 2018), and engineering (e.g., Smithyman et al. 2009) contexts, in addition to being widely adopted across the hydrocarbon sector (e.g., Sirgue et al., 2010; Prieux et al., 2013). The effectiveness of FWI is highly sensitive to the starting model being capable of predicting the travel time within half a dominant period, in order to avoid cycle-skipping (Virieux and Operto, 2009). This approach is, therefore, commonly preceded by travel time tomography.

Two phases of data acquisition (Fig. 3a) were conducted at the Scanner pockmark complex to acquire data suitable for the application of first arrival seismic travel time tomography and full waveform inversion. The first survey, conducted during cruise MSM63, utilised an array of 18 OBSs, with shots generated using two GI airguns. The OBS and profile locations are shown in Figs. 3a & d respectively. A second, more extensive experiment was conducted during cruise JC152, coincident with the anisotropy experiment (described in section 2.4, below), and utilising an array of 18 OBSs located in and around Scanner pockmark and 7 at a nearby reference site, located ~1 km southeast of the pockmark, where industry 3D seismic data showed no evidence of the presence of gas (Fig. 3a). These instruments recorded shots from all of the seismic sources used in the experiment (Fig. 3c). Figure 4c-f shows the shots recorded on an OBS located within Scanner pockmark for an ~E-W oriented profile for each of the airgun and surface sparker sources.

While travel time tomography approaches are not necessarily reliant on a priori information, it is important to consider additional constraints, where available, since a poorly constrained inversion

409 may produce a biased result, based on its parameterisation and/or starting model (Zelt et al., 2003).
410 Interpreted multi-channel seismic profiles may be used to inform the initial P-wave velocity model. In
411 turn, the results of travel time tomographic modelling can be employed to improve the processing and
412 interpretation of multi-channel seismic profiles, by providing independent velocity information. The
413 wider-angle transmission regime involved in OBS methods also assists in resolving the issue of acoustic
414 blanking beneath gas accumulations, such as those observed beneath Scanner pockmark (Fig. 2c), and
415 provides a further tool for the verification of whether observed chimneys represent actual subsurface
416 geological features, or reflection imaging artefacts.

417 The two seismic approaches, multi-channel seismic reflection imaging and tomography, are
418 highly complementary to one another and may be utilised most effectively when applied synchronously.
419 The results of seismic tomography are also complementary to laboratory scale rock physics
420 experiments, since they place constraints on larger scale in situ physical properties, and thus fracture
421 orientations and fracture density (Amalokwu et al., 2017; Jin et al., 2018), which then can be used to
422 complement the geo-mechanical models.

423

424 **3.4   Seismic anisotropy**
425 Fractures in sedimentary settings play a crucial role in defining the physical properties of subsurface
426 reservoirs, as they enhance porosity and permeability, or conversely may contribute to reservoir
427 compartmentalisation. Thus, fracture orientation, size, volumetric density and connectivity are of
428 interest to the understanding of subsurface fluid flow. Attribute analysis of stacked seismic images,
429 which includes techniques such as coherence analysis (e.g., Bahorich & Farmer, 1995), can detect larger
430 fractures. However, these techniques are unable to image smaller fractures, below the spatial resolution
431 of the seismic image. Therefore, in order to determine fracture properties at sub-seismic scale, seismic
432 anisotropy analysis can be applied, which utilises the directional dependence of transmitted seismic
433 signals. A range of theories have been developed to describe the elastic response of fractured rocks
434 (e.g., Hudson 1981; Thomsen 1995). While these theories generally agree for dry rock, they differ
435 considerably where fluids and fluid flow between cracks and pores are present (Liu et al., 2000).

436 Estimating fracture sizes from narrow-band observations of seismic anisotropy may lead to
437 misinterpretations, as there is an ambiguity whereby a medium containing a small number of large
438 fractures will generate the same response as a medium containing a larger number of smaller fractures
439 (e.g., Maultzsch et al., 2003). Therefore, a frequency-dependent approach to studying anisotropy, which
440 is sensitive to the length-scale of the causative mechanism for the anisotropy, is required. Properties
441 such as fracture scale length and fluid saturation can then be inferred from the frequency-dependence
442 of anisotropic attributes, as predicted by theoretical work (Chapman, 2003; Jakobsen & Chapman,
443 2009). The impact of partial saturation on anisotropy and attenuation in materials of known fracture
444 density and orientation has been studied using models that can link laboratory and field datasets
445 (Amalokwu, 2016), which are required to make robust determinations of permeability.

446 The Scanner pockmark anisotropy experiment used several seismic sources with different
447 frequencies, in the range ~10 Hz to 2 kHz, as described above (Fig. 3b). This broadband dataset was
448 specifically designed for the measurement of frequency-dependent anisotropy, to permit enhanced
449 fracture characterisation. In order to achieve maximal azimuthal coverage, which is necessary for
450 determining the directionality of anisotropy, profiles were acquired at multiple orientations through the
451 OBS array (Fig. 3c). Several approaches are available for investigation of frequency-dependent
452 anisotropy associated with chimneys. Details of the two active source and one passive source methods
453 that were used at Scanner pockmark are provided below.

454

3.4.1 _Shear-wave splitting_

The measurement of seismic travel time anisotropy using shear-wave splitting (SWS) is an established technique for determining the orientation and density of fracture networks (e.g., Crampin, 1985). Shear-wave splitting occurs when a polarised shear wave enters an anisotropic medium. When this occurs, the shear wave is split into two orthogonal components, oriented perpendicular and parallel to the fracture normal direction. The two split shear waves travel at different speeds through the fractured medium, resulting in differences in their travel time. SWS analysis uses converted P-to-S waves to determine the orientation of a symmetry axis associated with the fracture normal direction. SWS distinguishes between different anisotropic symmetry systems, which produce characteristic patterns that can be observed in transformed radial and transverse components of the horizontal geophone records (Fig. 4b). This approach can be used to differentiate between dominant horizontal transverse isotropy, which may be associated with vertically aligned fractures, and vertical transverse isotropy, which may arise in the presence of concentric fractures.

The orientation of these symmetry planes, and the directions of the fast and slow S-wave arrivals can be used to determine the fracture orientations. The measured delay between the fast and slow S-wave arrivals is used to determine the intensity of anisotropy, which is related to the fracture size and/or density (e.g., Crampin, 1985; Mueller, 1992; Li, 1997). Raw estimates of SWS give only depth-averaged estimates of fracture properties. Therefore, to determine the depth variation of both fracture orientation and density, a layer-stripping approach is required (Haacke et al., 2009), which recursively compensates and removes the anisotropy measured in shallow layers. Shear-wave splitting analysis is applied to the study of the chimney beneath Scanner pockmark in order to map the geometry and extent of the fracture network. This approach allows us to distinguish between different hypotheses for the structure of chimneys.

3.4.2 _Seismic attenuation_

While S-wave velocity anisotropy, observed through SWS analysis, is sensitive to both open and closed fracture networks, attenuation anisotropy is primarily sensitive to open fracture networks and the fluids that may be present within these (e.g., Worthington & Hudson, 2000; Chapman, 2009). Attenuation may occur through mechanisms including scattering and wave-induced fluid flow (Baird et al., 2013). Scattering of seismic waves due to aligned heterogeneities has long been recognised to be frequency dependent (e.g., Shapiro & Hubral, 1995; Werner & Shapiro, 1999).

Field observations of attenuation anisotropy have been reported from walkaround vertical seismic profile data (Varela et al., 2006; Maultzsch et al., 2007; Bouchaala et al., 2019), with the observed effects often being consistent with the predictions of poroelastic models accounting for wave-induced fluid flow (Chapman, 2003). If wave-induced fluid flow is the dominant mechanism for the observed attenuation anisotropy, then the phenomenon may provide a link to fracture induced permeability. Chapman (2009) considered the case of multiple sets of fractures having different fluid connectivity.

Application of seismic attenuation and attenuation anisotropy analysis at Scanner pockmark was directed at investigating both the geometry (cf. SWS) and contents of subsurface fracture networks, where these are present. As with travel time anisotropy, the broad-band frequency nature of the various seismic sources used is required to discriminate between the properties of fractures of different sizes, which may otherwise not be distinguished.

3.4.3 _Ambient noise anisotropy_

Methods for analysing surface waves from ambient noise utilise lower frequencies, typically <1-2 Hz, than the active seismic sources. This approach further extends the frequency range of frequency-

502 dependent analyses to determine fracture properties. Rayleigh wave velocities can be measured on the
503 vertical and hydrophone components of the OBS. By taking spectrograms of cross-correlations between
504 OBS pairs (processed according to Bensen et al., 2007) located on opposite sides of the chimney,
505 Rayleigh wave phase-velocity dispersion can be measured (Yao et al., 2006) and used to invert for
506 vertical shear-wave velocity structure. Applying Radon transforms to a set of cross-correlations
507 between all possible OBS pairs within an array and summing these over time, a technique known as 2D
508 beamforming (Lacoss et al., 1969), shows the slowness at which Rayleigh waves cross the array at all
509 azimuths. This method facilitates full-azimuth observations of anisotropy (Alvizuri & Tanimoto, 2011).
510   However, there are limitations on the frequencies that can be observed using passive methods
511 which arise due to the OBS array geometry. The largest spacings within the array, termed the aperture,
512 used at Scanner pockmark result in a lowest usable frequency of ~0.5 Hz (Rost & Thomas, 2009). For
513 beamforming there are also challenges arising from the array geometry. While the OBS array located
514 at the Scanner pockmark is relatively symmetrical, the array at the reference site is not, and so has a
515 highly asymmetric response in the slowness domain, which causes aliasing effects that can cause
516 artificial anisotropy to be observed. For analysis of azimuthal dependence to be effective, any artificial
517 anisotropy must be removed (Picozzi et al., 2010).
518   Cross-correlation analysis and 2D beamforming can be used to observe the dispersion and
519 azimuthal dependence of Rayleigh waves and can be inverted for 1D shear wave velocity structure at
520 Scanner pockmark in the 0.5-1.5 Hz range. This technique contributes both to constraining the structure
521 of the chimney and extending the range of frequencies which can be used for considering frequency-
522 dependent anisotropy characteristics.
523
524 **3.5   Controlled source electromagnetic surveying**
525 The marine controlled source electromagnetic (CSEM) method is used for mapping variations in
526 electrical resistivity of the subsurface (e.g., Cheeseman et al., 1987; Edwards, 2005). The CSEM
527 method used in this study involves towing a horizontal electric dipole close to the seabed that transmits
528 an alternating electromagnetic field. The electromagnetic energy diffuses through the sea water and
529 seafloor and is recorded by electric field receivers that are towed in-line behind the transmitter and
530 others that are stationary on the sea floor (Constable, 2013). The measured field amplitude and phase
531 lag between source and receivers relate to the electrical resistivity of the seafloor. When more resistive
532 Earth materials are encountered (e.g., low porosity sediments), elevated electric fields are observed at
533 the receivers and the phase lag is reduced.
534   The CSEM method is sensitive to changes in the bulk electric resistivity structure of the Earth,
535 a property that depends on lithology and mineral composition but is particularly sensitive to connected
536 porosity and pore fluid content (Palacky, 1988). Due to this sensitivity to sediment pore fluids, the
537 marine CSEM method has been widely used for hydrocarbon exploration (e.g., Ellingsrud et al., 2002;
538 Constable, 2010). Electrical resistivity is also an indicator for whether pathways for fluids to the seabed
539 exist, as the presence of aligned permeable and conductive fractures may lead to electrical anisotropy
540 (e.g., Naif et al., 2016).
541   The CSEM survey at Scanner pockmark was conducted during cruise MSM63, using the
542 University of Southampton deep-towed active source instrument (DASI; Sinha, et al., 1990), towed at
543 20-40 m above the sea floor. The source signal comprised a ~100 Ampere, 1 Hz square wave. Twelve
544 profiles were acquired, oriented in four different azimuths to assess the electrical anisotropy. Two
545 different types of receiver were utilised to record the induced field: an array of 14 ocean bottom
546 electromagnetic (OBEM) field receivers (6 three-component receivers and 8 horizontal-component
547 receivers; Fig. 5a), here measuring the electric field only, and two three-axis Vulcan electric field
548 receivers towed behind the source (Fig. 5b; Constable et al., 2016). The CSEM data from both receiver
549 types are processed with a Fourier transform over 1 s-long windows to obtain amplitude and phase data

550 in the frequency domain, and stacked over 60 s-long windows to improve the signal-to-noise ratio (Myer
551 et al., 2011). Estimating the electrical resistivity distribution from the data requires the use of modelling
552 procedures. For the towed receivers (Fig. 5c), 2D forward modelling for a homogeneous subsurface
553 with one resistivity value (half-space) is performed to compare the modelled data to the observed
554 vertical electric field amplitude (E_z) data and estimate the subsurface resistivity. For the seafloor
555 receivers (Fig. 5d,e), the magnitude of the major axis of the polarisation ellipse traced by the electric
556 field, P_{max}, is compared to 1D forward modelling results for half-space resistivities. P_{max} is independent
557 of the receiver orientation. Resistivities appear to increase with depth. Inversion algorithms (e.g.,
558 Constable et al., 1987) which optimise the fit between the observed and predicted data are required to
559 estimate a heterogeneous resistivity structure (analysis for the towed receivers is presented in Gerhmann
560 et al., this volume).

561 There are trade-offs between the thickness and resistivity of anomalous features (e.g., Edwards,
562 1997) that can be overcome using prior geological knowledge or constraints from complementary data.
563 For example, seismic reflection data can provide high resolution imaging of geological stratigraphy and
564 structures, while CSEM is able to detect the presence and type of fluids in the pore space, such as
565 hydrocarbons, CO_2, and variations in salinity. The difference between changes in pore fluid or
566 lithological variations may be distinguished by interpreting CSEM and seismic data in conjunction (e.g.,
567 Hoversten et al., 2006). Geological interpretations benefit from combined analysis with, for example,
568 wide-angle seismic data (e.g., Goswami et al., 2015), seismic reflection data (e.g., Weitemeyer et al.,
569 2011; Attias et al., 2016; Berndt et al., 2019), magnetic data (Gehrmann et al., 2019) and well logs (e.g.,
570 Harris et al., 2009).

571 The CSEM method is, overall, a relatively low-resolution method (10-1000 m), due to the
572 diffusive nature of EM fields. The specific resolution and penetration depth depend on the source-
573 receiver geometry, the number of receivers at different offsets to the source and the frequency spectrum
574 of the source signal (Edwards, 1988). The dual-receiver approach used here includes towed instruments
575 sensitive to the shallow subsurface and OBEM receivers sensitive to the deeper subsurface. For the
576 purposes of understanding potential subsurface fluid escape structures, the CSEM method provides a
577 tool to map variations in resistivity related to connected porosity and fluid/gas content of seafloor
578 sediments.

579

580 **3.6 Passive seismic methods**
581 Passive seismic monitoring involves the use of seismometers and sound recording devices, such as
582 OBSs, located at the seafloor. These instruments provide continuous recordings, and, therefore, capture
583 events during seismic acquisition interludes. In the Scanner pockmark seismic experiment, passive
584 seismicity was recorded using the same OBS array as for the anisotropy experiment (Fig. 3a).

585 Various types of events were detected using this approach, including: short (<1 s) duration
586 events, similar to those previously detected in gas seepage areas (Tary et al., 2012; Bayrakci et al., 2014;
587 Batsi et al., 2019), and which may represent collapses and/or the formation of small pockmarks; medium
588 (few seconds) duration events, comparable to a volcano-tectonic tremor (e.g., Latter, 1981; Harrington
589 & Brodsky, 2007), rarely observed in this tectonic context, and which may represent the movements of
590 fluids in conduits in the shallow subsurface; and events related to bubbles escaping at the seafloor. The
591 low frequency content displayed by these types of events (<30 Hz) mean it may also be possible to
592 identify these events during periods of, for example, sparker seismic acquisition, due to the much higher
593 frequency content of the source signal (≥200 Hz).

594 For recorded seismicity associated with gas bubble escape at the seafloor, the Minnaert (1933)
595 equation can used to estimate the bubbles' radii from the frequencies of the events. However, this
596 approach may not be able to distinguish between the acoustic signature of many small bubbles and one

597 big bubble, which highlights the necessity to calibrate this approach using additional methods (e.g.,
598 active acoustics).
599   Passive acoustic monitoring of seismicity associated with methane venting and/or fluid
600 movement in the subsurface at Scanner pockmark aims to quantify the gas flux through the chimney to
601 the seabed and into the water column. Unlike active acoustic methods, this approach represents a
602 continuous monitoring tool. The microseismic events detected through passive monitoring may be
603 associated with the local tidal cycle and, hence, may indicate a possible correlation between tides and
604 the movement of fluids from a subsurface reservoir to the seabed. Furthermore, if the seismicity is a
605 result of fluid movement at depth it may be applicable to studies of fluid flow beneath the cap rock or
606 overburden, where the fluids do not directly reach the seabed.
607
608 **3.7   Active acoustic methods**
609 Hydro-acoustic surveying involves the use of either single- or multi-beam echosounders, which transmit
610 one or more beams, respectively, of monochromatic frequency beneath the ship. The delay associated
611 with the returning pulse is typically used to map the underlying bathymetry, while the strength or
612 amplitude of the returning pulse can provide information on the physical properties of the reflecting
613 medium. Given the strong impedance contrast between water and gas, hydro-acoustic methods are
614 sensitive to the presence of gas bubbles in the water column (Fig. 6). The gas bubbles rise due to
615 buoyancy, drawing surrounding fluid into and upwards with the plume with lateral dispersion as a
616 function of bubble rising velocity and water current velocity. The gas plume comprises bubbles of
617 various sizes, with larger bubbles possessing relatively higher rising velocity and smaller bubbles
618 possessing relatively lower rising velocity. The plume can be observed to rise to the thermocline at ~40
619 m below sea surface (Fig. 6; Böttner et al., 2019; Li et al., 2020).
620   Multi-beam data can be used to map the three-dimensional extent of gas plumes escaping from
621 pockmarks and, across multiple surveys, observe variations over time. Seabed currents may cause the
622 plume to separate based on differing bubble size distributions, which can be mapped using multi-beam
623 data (Li et al., 2020). Similarly, observing the target strength of gas plumes in single-beam data can be
624 used to estimate the bubble size distribution and gas flux being released from the pockmark, provided
625 a range of frequencies covering the bubble resonance frequency are used (Li et al., 2020).
626   Active hydro-acoustic surveying was applied in the study of the active venting at the Scanner
627 pockmark in order to quantify the gas flux from the seabed and to study the gas plume evolution in the
628 water column. Repeat surveys can also be used to determine if there is any temporal variation, for
629 example due to tidal cycles (e.g., Boles et al., 2001; Schneider von Deimling et al., 2010). Temporal
630 patterns may also be compared with observations from passive acoustics, which provide a continuous
631 record of gas venting at the seabed, or of the migration of fluids at depth.
632
633 **3.8   Direct sampling of sediments and pore fluids**
634 *3.8.1   Drilling and coring*
635 Direct sampling of seabed sediments via coring allows for a local characterisation of lithology, porosity
636 and other geophysical and geochemical attributes at centimetre-scale or less resolution, providing a
637 verification of geophysical properties and parameterisation for numerical models. Detailed description
638 of sediments in terms of their lithology, physical, and chemical properties allows determination of the
639 geological origin of the sediments, the extent and characteristics of specific stratigraphic units, the
640 possible origin of the pore fluids, and a very high-resolution, visual observation of changes in sediment
641 texture and fabric. Changes in sediment colour, e.g. the presence of black layers that form when methane
642 is consumed by anaerobic methane oxidation with sulphate, and the structure of the sediment, e.g. the
643 presence of outgassing and fluidisation structures, provide evidence for the presence of gas in the

644 sediment, as well as evidence for palaeo-fluid migration. Further, non-invasive 3D analysis of sediment
645 structure is possible using XCT imaging techniques (Fig. 7b-e), which can highlight the spatial
646 distribution of dense materials such as iron sulphides that can form during anaerobic methane oxidation
647 (Fig. 7c,e). Geochemical analyses of pore fluids can be used to determine their origin and, hence, the
648 presence of migration pathways and the connectivity of different layers. Geochemical analyses of the
649 solid phase allow understanding of the chemical reactions that are occurring or have occurred in the
650 sediments and can explain physical properties, such as changes in permeability caused by carbonate or
651 iron sulphide precipitation. Methane derived authigenic carbonates in the sediments and on the seafloor
652 are indicators for prolonged presence of fluid flow, and can be dated to derive information about fluid
653 flow history.
654   Sediment cores from the Scanner pockmark complex and a reference site located ~7 km to the
655 east (Fig. 1b,c) were recovered using the BGS Rockdrill (RD2) and a gravity corer during cruises
656 MSM78 and POS518-2 (Fig. 7b). RD2 is a remotely operated multi-barrel wireline subsea robotic
657 sampling system that continuously cores 1.72 m-long sections, with a diameter of 6.1 cm. The
658 maximum drilling depth was 33 mbsf at the reference site. Gravity cores were collected from the
659 uppermost 5.75 m of the sediment column using a 12.5 cm-diameter tube driven into the seabed under
660 weight-assisted free-fall (Linke & Haeckel, 2018).
661   Immediately following collection of the sediment cores, pore waters and sediment samples
662 were extracted from both RD2 and gravity cores. Pore waters were collected with 0.2 μm-pore diameter
663 Rhizons (Seeberg-Elverfeldt et al., 2005; Dickens et al., 2007) at approximately 30 cm depth intervals,
664 and preserved for analyses of cations (e.g. dissolved Ca, Fe, Mn, Si, B), anions (e.g. Cl, SO_4, total
665 alkalinity), nutrients (NH_4, PO_4, Si, NO_x) and dissolved sulphides. Samples of the sediments were
666 collected with cut-off 5 cm syringes and analysed for their methane concentrations and methane carbon
667 isotopic composition, porosity, grain size and organic and inorganic carbon content. The cores were
668 then scanned using a GEOTEK multi-sensor core logger (MSCL; Fig. 7a), to measure acoustic wave
669 velocity, density, resistivity and magnetic susceptibility, before being sectioned horizontally,
670 photographed, and logged. The chemostratigraphy of the sediment was then measured in high resolution
671 (1 mm) with the ITRAX XRF core scanner.
672   Some caution is required during core logging and interpretation, as artefacts such as small-scale
673 fractures and other disturbances can be introduced during the drilling procedure. This is particularly
674 important for soft, non-lithified sediments such as those found in our study area, as the coring process
675 may reduce porosity, due to dewatering compaction and shear straining (Bouma & Boerma, 1968;
676 Blomqvist, 1985). Concentrations of some reactive geochemical parameters (e.g., dissolved Fe,
677 dissolved inorganic carbon, H_2S and CH_4) may further be affected by outgassing or chemical oxidation
678 during the retrieval and subsampling of the cores. These effects can be minimised by subsampling
679 immediately after core recovery, or by the use of in-situ measurement techniques such as lab-on-chip
680 sensors (e.g. Whitesides, 2006).
681   While coring and drilling approaches allow very high (cm-scale) vertical resolution, the
682 horizontal resolution is limited by the number of sediment cores that can be taken within the time frame
683 of an expedition. Therefore, appropriate sampling strategies are required to effectively integrate the
684 information from sediment cores with information gathered using other approaches. For the purpose of
685 our study, previously acquired seismic, real-time fast-track processed seismic lines, and prior
686 information about the shallow geology was used to inform our drilling strategy. However, at the Scanner
687 pockmark drilling locations, RD2 settings were configured for recovery of authigenic carbonates, rather
688 than unconsolidated sediments, and as a result, sediment recovery was rather low (~50%), due to
689 washout of loosely consolidated sand intervals.
690   The integration of sediment core and geophysical data maximises their inherent value, by
691 providing localised sub-seismic resolution site-specific constraints (Vardy, 2015; Vardy et al., 2017;

692 Provenzano et al., 2018). Multi-sensor core logging of sediment cores permits the measurement of
693 geophysical and geotechnical parameters, providing a way to: calibrate the two-way-time seismic
694 reflection data to depth; constrain seismic inversion and interpretation within a range of plausible values
695 (e.g., Provenzano et al., 2018); interpret and cross-validate the results of seismic tomography and CSEM
696 methods; and interpret physical properties in terms of changes in sediment properties, such as porosity
697 (e.g., Vardy, 2015; Baasch et al., 2017). Appropriate calibration of the instruments is necessary for a
698 meaningful comparison between samples acquired using different coring techniques and core liner
699 materials, and the need to account for laboratory temperature and humidity conditions.
700

701 *3.8.2 Geomechanical testing and sediment core analysis*
702 Rock physics experiments permit the direct examination of the changes in geophysical, geomechanical
703 and geochemical sample properties under controlled conditions in the laboratory. Two rock physics
704 experimental setups were used in combination for the study of coupled thermo-hydro-mechano-
705 chemical phenomena occurring in a rock-brine-CO_2 system: (1) multi-flow CCS and (2) acoustic pulse
706 tube rigs.
707 Firstly, the multi-flow CCS rig permits the analysis of geophysical signatures (ultrasonic P-
708 and S-wave attributes, and electrical resistivity) of reservoir rocks subjected to brine and CO_2 flow-
709 through tests at controlled reservoir pressure and temperature conditions, resulting from the
710 hydromechanical changes occurring in the rock sample due to CO_2–brine fluid substitution effects and
711 rock-fluid reactivity. Secondly, the acoustic pulse tube rig allows the measurement of seismic velocity
712 and attenuation of P-waves in sediment and rock samples over a frequency range of 1-10 kHz and S-
713 waves at 500 Hz. This frequency band complements the ultrasonic frequencies obtained by the multi-
714 flow CCS rig and helps to constrain improved rock physics models accounting for fluid mobility and
715 frequency-dependent seismic effects (Batzle et al., 2006; Mavtko et al., 2009). In addition, the P- and
716 S-wave frequency ranges of the acoustic pulse tube measurements partially overlap with the sparker
717 sources used for the seismic anisotropy assessment of the Scanner pockmark (Fig. 3b), permitting the
718 calibration of the seismic data under controlled conditions in the laboratory.
719 The experimental approach used provides a geophysical and hydromechanical assessment of
720 fluid flow in (i) CO_2 reservoir rocks and (ii) the shallowest section of the marine sediment overburden.
721 In the former case, the reservoir rock experiments simulate variable spatial-temporal states during
722 (drainage) and post- (imbibition) CO_2 injection, considering homogeneous (background) and fractured
723 (slip-related features) reservoir samples. In the latter case, the tests focus on the hydrodynamic response
724 of near-seabed sediments subjected to variable CO_2 flow rates.
725 A study of reservoir rocks was conducted using natural reservoir samples (Utsira sand
726 formation, Sleipner; Falcon-Suarez et al., 2018), and quartzose synthetic sandstones manufactured in
727 the lab following the procedure described in Falcon-Suarez et al. (2019), including homogeneous
728 (Falcon-Suarez et al., 2016, 2017) and fractured samples (Muñoz-Ibáñez et al., 2019). In all tests, an
729 increasing CO_2-to-brine partial flow condition was imposed through the originally brine-saturated
730 samples, in order to progressively saturate the sample in CO_2. The confining stress, pore pressure, and
731 temperature conditions slightly varied between tests, within the ranges 16-40 MPa, 7-12 MPa, and 20-
732 35 °C, respectively. The fluid substitution process and related hydromechanical response of the rock
733 were assessed though the continuous monitoring of ultrasonic P- and S-wave velocity and attenuation,
734 electrical resistivity, axial and radial strains, and hydraulic conductivity.
735 Figure 9 shows a comparison between the results obtained using a synthetic (Falcon-Suarez et
736 al., 2016) and a natural (Falcon-Suarez et al., 2018) sandstone, with similar composition and porosity.
737 The arrival of CO_2 in the rock samples lead to increased resistivity, together with a sudden drop (> 5%)
738 in P-wave velocity and increase in the attenuation (more significant in the synthetic sample), while

16

739 subsequently increasing the CO_2 content had only limited further effects. Forced imbibition is used to
740 study the trapping efficiency of the rock through evaluation of the residual CO_2 content and the
741 geophysical signatures associated with this value. In this regard, Muñoz-Ibáñez et al. (2019) studied the
742 hydrodynamic behaviour of a fractured reservoir analogue sample, and found that non-connected,
743 fractures may act as larger cavities than background porosity, and these cavities are energetically
744 favourable for CO_2 storage. Therefore, non-connected fractures have the potential to enhance CO_2
745 trapping and the overall sealing efficiency of CO_2 storage reservoirs (Muñoz-Ibáñez et al., 2019), in
746 contrast to the role played by a connected fracture network (i.e., the hypothesised structure of a
747 chimney).

748 In addition, gravity core samples from cruise POS527 (Achterberg & Esposito, 2018) were
749 used to conduct flow-through experiments, to analyse the coupled hydro-mechanical-chemical response
750 of seafloor sediments subjected to sudden gas release episodes (e.g., pockmarks). These experiments
751 included (i) a set of permeability tests to monitor the sediment reactivity to CO_2 (i.e.
752 dissolution/precipitation), and (ii) a simulation of the STEMM-CCS CO_2 release experiment (Flohr &
753 Schapp et al., this volume) to collect linked geophysical-hydromechanical information about the target
754 site under controlled conditions in the laboratory. The data collected during these experiments indicate
755 permeabilities of ~10^{-16} m^2 in the upper part of the sediment column. Preliminary analyses of reactive
756 transport models (Marin-Moreno et al., 2019) indicate that the sediment is largely unreactive to the
757 exposure of CO_2 saturated brine, while the grain size may be conditioning the CO_2 distribution within
758 the sediment; from clay- to sand-rich layers the distribution becomes more homogeneous (Roche et al.,
759 this volume).

760 For further understanding of hydraulic fracturing and gas migration mechanisms, flow-through
761 experiments were carried out on gravity core samples recovered from locations adjacent to the STEMM-
762 CCS CO_2 release site during the RV Poseidon cruise POS534 (Schmidt, 2019). Combining
763 geomechanical testing with XCT imaging (Fig. 10d; Deusner et al., 2016) allows the visualisation of
764 fracture formation in response to pressure accumulation and fluid injection. Fracture formation in the
765 poorly consolidated clay sediments started at a low critical pressure of ~5-15 kPa above the confining
766 stress (Fig. 10a). Fracture propagation was essentially perpendicular to the major principal stress
767 direction, likely resulting from the formation of disk-shaped gas bubbles with high aspect ratios, as
768 expected in clay sediments (Boudreau et al., 2005). Fracture formation was first observed from rapid
769 gas pressure dissipation (Fig. 10b, event 4) and the appearance of a small gas accumulation in the XCT
770 image projections (Fig. 10c). Mass balancing of the injected gas and changes in confining volumes after
771 fracture opening until the end of the first injection interval indicate a high apparent fracture permeability
772 (Fig. 10b). Flow-through experiments and coupled thermo-hydro-chemo-mechanical studies can
773 provide important insight into fracture formation and propagation in natural sediments, and are an
774 important tool to develop and validate numerical models of chimney evolution. However, mechanical
775 and hydraulic constraints in small-scale laboratory experiments will not provide an exact replication of
776 the in-situ field environment, which must be carefully considered during experimental planning and
777 data interpretation.

778

779 ### 3.9 Onshore outcrop analogues
780 In addition to direct sampling of an actively venting system, further characterisation and the long-term
781 development of fluid escape structures can be determined from analysis of onshore outcrop analogue
782 systems. Field outcrops permit characterisation of physical structure, geometry, physical properties and
783 understanding of past physical, chemical and hydro-mechanical processes, through direct observation
784 and sampling. However, fluid escape outcrop analogues are challenging features for comparative
785 analysis with active subsurface systems (e.g. Roberts et al., 2017). Following the cessation of active
786 fluid flow, a number of diagenetic and surface processes may alter the physical properties of the rocks,

787 which can include post-dewatering compaction, cementation, groundwater-induced geochemical
788 alteration, weathering and erosion. XCT techniques can be utilised to acquire 3D digital rock images of
789 the outcrop samples, whereby the cement can be selectively removed using image processing
790 techniques, allowing the study of the physical and hydraulic properties of the rock formation prior to
791 cementation (Fig. 8d; e.g. Böttner et al., in review).

792   There is often a discrepancy between the scales of fluid flow features observed in onshore
793 outcrops and their seismic manifestations, whereby chimneys observed in seismic data can extend
794 several hundreds of metres in diameter and up to 1000 m in height (Berndt, 2005; Cartwright et al.,
795 2007; Løseth et al., 2009; Andresen, 2012; Karstens & Berndt, 2015). Outcrops of sand-filled fractures
796 in California (Fig. 8c), which are sand intrusions that form due to exceedance of lithostatic pressure and
797 subsequent remobilisation and fluidisation of sediments (Huuse et al., 2010; Hurst et al., 2011), have
798 been observed to reach similar dimensions to their corresponding seismic discernible features (Huuse
799 et al., 2005; Ross et al., 2014). However, the largest known field outcrops of hydrocarbon-derived
800 carbonate conduits, located in Varna, Bulgaria, are only up to 10 m high and ~1 m in diameter, and are
801 spread over a comparatively small area (2.4×10^5 m^2; De Boever et al., 2006a, 2006b). The lack of
802 outcrop evidence for fracture systems that extend up to 1000 m in vertical height, and with large spatial
803 extent is likely a consequence of the preferential preservation of hard parts, as suggested by the observed
804 sand-filled fractures and carbonate pipes in California and Varna, respectively (De Boever et al., 2006a;
805 Hurst et al., 2011). However, a benefit of field outcrop analogues is that sub-vertical structures can be
806 mapped at mm-scale resolutions, which is not possible using seismic reflection imaging. Consequently,
807 more accurate quantification of fault/fracture properties, such as measurement of aperture or cement
808 infill type, is achievable using outcrop based studies. The study of outcrops can be complemented with
809 the mapping of a target area, using unmanned aerial vehicles (UAVs) that allow mapping over large
810 distances (km-scale) at very high accuracy (cm-scale). These data can then be used to calculate digital
811 elevation models, image mosaics and high-resolution point clouds which, once geo-referenced using
812 ground control points, can help close the observational gap between seismic data and geological field
813 sampling.

814

815 **3.10 Process-based numerical modelling**
816 Process-based numerical modelling, for simplicity called hereafter numerical modelling, can be used to
817 provide quantitative insights into: how chimneys form and propagate through time and space; the
818 distribution and transport of mass (water, CO_2, CH_4, higher hydrocarbons, salts, grains etc.) and energy
819 (heat) components among different phases (solid, liquid, gas) through pores and fractures; the complex
820 coupled physical and chemical processes between the above components and properties; and the
821 changes in petrophysical (e.g., porosity and permeability) and chemical properties (e.g., dissolved gas
822 distribution in the formation fluid brine). Therefore, numerical modelling approaches are useful in
823 helping to quantitatively understand the governing processes that can explain observations, but they
824 are, in turn, reliant on appropriate calibration relating to the target of interest.

825   As part of the STEMM-CCS and CHIMNEY projects, reactive transport modelling has been
826 conducted (by Marin-Moreno et al., 2019) to examine the migration of injected CO_2 through a generic
827 chimney, using Scanner pockmark as a proxy for pressure, temperature, geological, mineral and
828 chemical conditions. In the model, the chimney extends upwards in the subsurface reservoir through
829 the caprock to a shallowest depth of 400 mbsf, where it meets the overburden (Fig. 11a). Modelling
830 was conducted in radially symmetric geometry approximation, with injection of CO_2 taking place at
831 500 mbsf and 0 m radial distance. The time scale of this analysis is 100 years, longer than potential
832 geological CO_2 injection activities.

833   Modelling indicates that, over these timescales, the porosity (Fig. 11b) and permeability (Fig.
834 11c) changes due to dissolution and precipitation of minerals are negligible for the representative

835   chimney being modelled (Marin-Moreno et al., 2019). Hence, for this particular location and over the
836   time scale of this analysis, the modelling of chemical reactions (Fig. 11d,e) can be dismissed. For
837   injected CO_2 saturations of $\geq 30\%$, and with overburden isotropic matrix permeabilities and chimney
838   effective vertical permeabilities (average permeability of the matrix and the fractures in the chimney)
839   of $\geq 10^{-14}$ m^2, the models indicate that CO_2 reaches the seabed, at 500 m above the injection point, in
840   less than 100 years (Fig. 11a,f).

841   The modelling conducted assumes that the injection of CO_2 occurs far away from the chimney,
842   in isothermal conditions, and that there are no mechanical changes (Marin-Moreno et al., 2019).
843   However, the non-isothermal upwards migration of CO_2 may create stress- and thermal-induced
844   deformations that could affect the aperture of existing fractures, or create new fractures, and so, in turn,
845   affect the migration processes. Thus, assessment of the impact of thermal, hydraulic and mechanical
846   changes of fractures within chimneys may require further consideration.

847   The dynamics of fluids migrating within the shallow overburden sediments can also be assessed
848   using a Navier-Stokes-Darcy multi-fluid flow model (AnsdMF), which simulates the mass and
849   momentum exchanges of multi-fluid phases (Behzadi et al., 2004; Bannari, et al., 2008) and couples
850   the turbulent flows in the ocean with the flows in sediments (Fig. 12a). The AnsdMF modelling was
851   conducted in 2D, and comprises a sediment layer with a defined thickness, porosity, and fracture
852   properties (length and aperture; Fig. 12b). These subsurface characteristics may be further constrained
853   using other methods discussed in this study. Above the seabed is a turbulent bottom boundary layer.
854   The location and rate of gas release beneath the seabed are then specified and the gas is tracked as it
855   migrates and disperses through the sediment, and is expelled from the seabed (Fig. 12c).

856   The AnsdMF model is robust and efficient for simulations of multi-fluid flow in sediments with
857   a complex structure and variable fracture properties, and fluid pathways to a turbulent ocean. In
858   addition, AnsdMF can be applied over a wide range of scales, ranging from micro/pore- to field-scale
859   ($\leq 10^{-2}$ to $\geq 10^3$ m). The observations from computational fluid dynamic models can be calibrated against
860   observations derived from active acoustics, which provide a measure of fluids expelled from the seabed,
861   and passive acoustics, which can additionally detect flow within the subsurface, to compare flux rates
862   of subsurface fluid migration with observed discharge from the seabed. Further, bio-ecosystem models
863   could be coupled with AnsdMF and advanced oceanic hydrodynamic models to assess the impacts of
864   fluid migration on benthic ecosystems and in the water column (Blackford et al., 2020).

865

866   **4   DISCUSSION - A MULTI-SCALE, MULTI-DISCIPLINARY APPROACH**
867   **4.1   Parameters**
868   In this paper, a number of methods have been identified which can be utilised and integrated to generate
869   a comprehensive characterisation of subsurface fluid pathways associated with chimneys. The
870   parameters influencing fluid flow within chimneys can be broadly divided into three categories: 1)
871   structural properties including the subsurface stratigraphic structure, the presence, geometry,
872   distribution and connectivity of fractures, and principal stress magnitude and orientation; 2) physical
873   properties of the sediments, including thermal, hydraulic, mechanical, elastic, and electrical properties;
874   and 3) fluids, which includes their presence, phase, and distribution in the subsurface, chemical
875   composition and volume/mass flux calculations (Table 1; Fig. 13). In general, at least one approach
876   from each of the method groupings (Table 1 left-hand column) is required to reach a sufficiently detailed
877   and holistic understanding of the structure and processes involved in the venting of gas via a chimney.

878   We have also identified five method traits: resolution, length scale, temporal applicability, co-
879   dependency and resource use. The method parameters and traits are summarised in Table 1 and are
880   further discussed below.

881

4.2 Resolution and scale

Table 2 shows (a) the order of magnitude resolutions and (b) length scales (area and/or depth) achievable for each method applied to the study of a chimney. Table 2a demonstrates that there is a resolution gap between the geophysical (seismic, acoustic, CSEM) and geological/geochemical (rock sampling, laboratory) methods around the m-scale. Numerical modelling approaches allow bridging of the resolution gap, by the integration of data from the geophysical, geological and geochemical methods.

There is an inherent trade-off between resolution and length scale, whereby methods capable of achieving higher spatial resolution can typically only be applied at reduced length scales. This is particularly an issue in the vertical dimension. This trade-off arises in seismic and CSEM studies due to an intrinsic relationship between the imaging resolution and depth scale, whereby lower frequency sources have greater depth penetration, due to the stronger attenuation of higher frequency signals over lower frequencies (Resnick, 1990). However, vertical imaging resolution is also related to bandwidth, with lower bandwidth signals resulting in a lower vertical resolution than higher bandwidth signals. Taking the seismic approaches utilised in this study as an example, the lower frequency airgun sources generate the best depth penetration (≥100s of m), but are limited to high m to 10s of m or greater vertical resolution, while sparker sources may only penetrate a few 100s of m, but can generate m-scale resolution, and sub-bottom profiler recording (which we include here with seismic approaches as they are applied for the same purpose) can achieve resolutions on the dm-scale, but with only very limited (10s of m) depth penetration. Therefore, where frequency-dependent attenuation is a factor in measurements made using a particular method, Table 2 must be considered in this context.

An optimal subsurface imaging approach would assess parameters at the highest resolution possible over the areal and depth extent of the chimney. However, where these features are located at depth, beneath overburden and sealing layers, attenuation of higher frequencies results in a depth-resolution trade-off, with increasingly only larger features visible. This represents a key motivation both for the application of a multi-frequency surveying approach in the Scanner pockmark seismic experiment, utilising a range of seismic sources (e.g. airguns, sparkers), and the study location chosen. Together, these allow the development of a cross-scale, sufficiently resolved image of a chimney at shallow depth, where it can be studied in detail, with other techniques (laboratory experiments, numerical modelling) then able to extend the observations to the deeper subsurface, where they may be detected by geophysical techniques at lower resolution. The use of a broad seismic source frequency range for the anisotropy experiment is also critical, due to the frequency dependence of anisotropy detection and interpretation (Chapman, 2003).

In addition, some of the methods display differing sensitivities to the magnitudes of the properties being measured (e.g., Constable, 2010). For example, while the elastic properties of sediments are sensitive to both lithological and pore fluid variations, their electrical resistivity is dominated by the pore fluid component. The differing response of these two techniques as gas saturation varies has been shown by Constable (2010) for a 50% porosity sand. The largest effect on P-wave velocity occurs for the first few percent of gas fraction, and changes very little above this (White, 1977; Lee, 2004). In contrast, the resistivity response increases exponentially with increases in gas saturation (Archie, 1952). As a result, gas saturations determined using seismic and CSEM methods may differ (e.g., Goswami et al., 2015; Attias, 2020; Bialas et al., 2020), with CSEM being more sensitive to the wider saturation-range response measurable.

4.3 Temporal applicability

The integrated methods described in this paper also influence the temporal scales over which fluid flow through chimneys can be understood (Table 1). Only a few of the methods can be used to determine temporal information related to pore fluid changes in the subsurface (measured at discrete time intervals

930 using time-lapse/4D seismic), fluxes through the subsurface (measured discretely by active acoustics,
931 and measured/modelled continuously using passive seismics and computational fluid dynamics) and
932 fluid-induced chemical and physical changes (geochemical methods and numerical modelling).

933   Repeat geochemical data collection and seismic surveying can be conducted, commonly on the
934 time scale of every year or few years. However, measurement of true temporal changes using seismic
935 data, rather than seismic artefacts, is limited by the repeatability of the surveying technique. This makes
936 time-lapse seismic studies most suitable for application to areas of well stratified and undisturbed
937 sediments, rather than chaotic features such as chimneys (e.g., Waage et al., 2019). Developments in
938 time-lapse seismic repeatability, such as continued use of true-4D imaging, or the installation of
939 permanent seabed sensing infrastructure such as OBS or fibre optic cables, have the potential to improve
940 this.

941   Passive seismic and active acoustics can resolve temporal flow variations on the order of
942 seconds to weeks, providing information on the ascent of individual bubbles, but also how flow is
943 modulated by diurnal tides. Of these, however, only passive seismic provides continuous temporal
944 information over extended periods of time. These two methods have, therefore, different applicabilities
945 to short- and longer-term monitoring activities of fluid escape associated with chimneys. Both acoustic
946 methods also play an important role in the calibration of computational fluid dynamic models of fluid
947 migration through the chimney and out of the seabed. These models can then be adapted to provide
948 further information about the temporal evolution of fluid flow processes through chimneys in different
949 geological settings.

950   Of the methods that can be used to assess changes in the properties of chimneys over time, only
951 numerical modelling approaches can be extended to much longer timescales (centuries to millennia),
952 compared to experimental, field or laboratory techniques. Field-based outcrop analysis may also be
953 considered to provide additional temporal information, allowing understanding of flow over geological
954 timescales, long after active flow has ceased. However, the integration of these techniques enables the
955 development of new multiscale coupled seismic-hydro-mechano-chemical modelling approaches, with
956 the potential of enhancing predictions of chimney behaviour over time.

957

958 **4.4 Co-dependencies**

959 Table 1 shows that a range of geophysical methods can be used to determine the site parameters of
960 interest to the study of fluid flow structures. However, the successful application of individual methods
961 relies on a network of co-dependencies between different methods for calibration and constraint (Table
962 1). In particular, inverse methods, such as travel time tomography and CSEM are subject to inherent
963 trade-offs between model parameters, such as velocity or resistivity respectively, and layer thickness
964 (Edwards, 1997). Travel time tomography is also problematic when trying to resolve low velocity
965 zones, as the energy is diverted away from them. As a result, use of prior geological knowledge, or
966 constraints from other data, is important in the modelling process (e.g. Harris et al., 2009; Goswami et
967 al., 2015; Attias et al., 2016).

968   Some co-dependencies are more significant than others. Seismic reflection imaging provides
969 constraints on several of the methods utilised in this study, which explains its widespread use in
970 subsurface exploration and monitoring programmes. Seismic reflection imaging and seismic inversion
971 are co-dependent, although it is possible for these methods to be deployed fully independently. It is
972 advantageous for travel time tomography to have input from reflection imaging of the subsurface in
973 order to constrain the solution of the non-unique tomographic problem towards realistic subsurface
974 structures. However, it is also important that modelling is conducted in an objective manner that does
975 not overly bias the result, and suitable modelling approaches can be applied which do not
976 require/depend on this additional starting constraint. The velocity information which is obtained from
977 travel time tomography or FWI can be used to improve the quality of seismic reflection imaging,

including assisting with migration and depth conversion, in which accurate interval velocity information plays a central role. Furthermore, it can provide velocity information in areas of seismic blanking or potential artefacts, such as those associated with the presence of gas in the chimney. Converted-wave seismic anisotropy may also be partially reliant on seismic reflection data, to identify seismic horizons where mode conversion may occur, and an independent shear-wave velocity constraint is also required to interpret from which layers these signals may be originating, and for layer-stripping (Haacke & Westbrook, 2006).

Laboratory experimental approaches can provide insights into the dominant processes governing the response of the system. The experimental strategy and the ability to approximate the real behaviour of subsurface chimneys, or other subsurface fluid migration pathways, depends on suitable calibration and constraints from field geophysical and geochemical experiments. Laboratory experiments are directly dependent on the quality of direct sampling. One way to minimise this dependency is to use synthetic samples to replicate subsurface material. In the study of Scanner pockmark, the main limitation of direct sampling was dewatering of the water saturated, poorly consolidated samples that likely occurred during the core extraction process, leading to alterations in the physical properties of the core material. Future optimisation of the core extraction process is required, to ensure improved preservation of poorly consolidated cored material. Autoclave pressure coring tools could be used, such as the IODP Pressure Core Sampler (Graber et al., 2002) or MeBo-MDP (Pape et al., 2017), that are able to retrieve sections of a drill core under in-situ pressure, thereby avoiding disturbances of the cored sediment due to degassing that occur during conventional coring. Hence, pressure coring permits the investigation of cored materials whilst retaining the in-situ physical, structural and chemical properties (e.g., permeability, gas content, resistivity, salinity). Furthermore, the acquisition of borehole geophysical measurements (e.g., cross borehole surveys using wireline logging tools) is another common method for obtaining in-situ measurements, provided that the drilled borehole is stabilised by a liner (e.g., Crain, 2010). The results from rock physics experiments can be used to derive and validate the results of travel time tomography, FWI and seismic anisotropy studies.

Multiphase and multicomponent numerical modelling of the thermal, hydrological, mechanical and chemical response of marine geological systems with chimneys is currently limited by the robustness of available in-situ geophysical and chemical characterisation methods, especially for fracture geometrical, physical and chemical properties, and the difficulty in accurately recreating these in the models. How well individual processes are represented in the numerical modelling results depends strongly on the in-situ geophysical and geochemical data available to constrain the model input parameters. This further highlights that an appropriate direct rock sampling strategy is an essential part of the multi-disciplinary approach for chimney characterisation .

Active acoustic and passive seismic methods for detecting fluid flow can be applied independently of other approaches (Fig. 13a). A water-column sound velocity profile is required for accurate calibration of the shipboard echo-sounders, and, depending on the subsurface geological structure, a detailed velocity model may be necessary for accurate relocation of micro-seismic events. Cross-calibration of these two approaches is important, in order to extend the temporal observations of more punctual active acoustic surveys, and to resolve ambiguities in the apparent response of different bubble size distributions. These approaches also provide an important calibration for computational fluid dynamic modelling, either by indicating the potential flux entering the modelled system or measuring the expulsion from the seabed.

4.5   Resource use, challenges and development

It is also important to consider resource demand in the study of focused fluid flow conduits, such as the chimneys at Scanner pockmark, and how this may impact future studies relevant to CCS operations. Resources may include both direct monetary costs associated with data acquisition, in addition to less-

well defined time-based costs, which cover the data processing and interpretation. Ultimately, there is a trade-off between the field experimental methods which can be performed using a given set of resources (including time), and the total amount of information which can be determined about the subsurface structure.

Offshore site characterisations are generally spatially discrete snapshots in time. Undertaking studies of this nature requires field expeditions, including ship time, which results in relatively high monetary costs. Furthermore, the spatially discrete nature of offshore site investigations means that subsurface information must be gathered from all potential future sites of interest to CCS, to understand the geometry of the structures that may be present.

Depending on the availability of prior information about the specific imaging target, such as its spatial and depth scale, and the practicalities of implementing different imaging techniques, it may be possible to conduct experiments where multiple data sets are acquired concurrently, reducing the time-cost of the operation. For example, during the cruise JC152 seismic experiments at Scanner pockmark both the travel time tomography and seismic anisotropy datasets were collected using the same sets of shots, while the GI, Duraspark and Squid sparker sources were also recorded using a towed seismic streamer. Passive seismicity, for the study of fluid migration through the subsurface and ambient noise, was recorded using the same OBS array as for the JC152 tomography and anisotropy experiments (Fig. 3a). However, the parameters of a single seismic experiment may not be able to ideally meet the needs of all the different types of analysis that may be required for full and detailed characterisation of the subsurface feature(s) of interest. For example, for ambient noise studies, larger OBS station spacings would allow lower frequencies to be utilised in the analysis (e.g., Rost & Thomas, 2009). However, this conflicts with the smaller spacing required to achieve the maximum shallow subsurface resolution in tomographic models.

In a number of cases, the time-based cost of the techniques described in this study is relatively low, due to the relative simplicity of data processing using well-established methods (e.g., seismic reflection data, active acoustics, core/field sample analysis). However, while many of the methods discussed in this study are well-established and extensively used in both research and industrial settings, there is potential for future reductions in resource costs. Methods such as travel time tomography, CSEM, passive acoustics, and seismic anisotropy involve significant time in manual data picking and/or modelling, resulting in high relative time costs. Future developments in data processing may permit the replacement of manual processing stages with automated workflows, which may be facilitated by machine learning and artificial intelligence (e.g., Kim et al., 2018; Kong et al., 2019), resulting in reduced time costs. Further, from the geophysical experiments at Scanner pockmark, it can be determined that significant seismic processing time could be saved if OBS and OBEM spatial coordinates, degree of tilt and orientation, are more accurately constrained during data acquisition (e.g., Haacke & Westbrook, 2006). Installing permanent OBSs or fibre optic cables would allow easier and more cost-effective implementation of repeat seismic surveying, where multiple cruise legs are required. Compared to offshore exploration costs, laboratory experiments can be run at much lower expense, especially the measurement of basic parameters, while the investigation of the effect of parameter changes (e.g. temperature, pressure) on the system may also be tackled using carefully designed experiments.

Ultimately, the STEMM-CCS and CHIMNEY studies of the chimneys at Scanner pockmark provided significant information on the structure of these features, which may be applied in future studies. The multi-scale and multi-parameter design of these investigations demonstrates that the integration of subsurface geophysical characterisation of a chimney with laboratory experiments, process-based numerical modelling approaches, and onshore analogues is possible. We also anticipate that our findings will be applicable for future targets, in particular those located at depth, beneath the overburden and sealing cap rocks, where higher resolution subsurface imaging is much more

1074 challenging. Therefore, the findings of the STEMM-CCS and CHIMNEY projects have the potential to
1075 reduce future resource intensiveness, whereby the pre-existing knowledge of fluid flow systems gained
1076 from studying the Scanner pockmark complex can be applied to new sites, reducing the need for
1077 additional site specific data acquisition.
1078
1079 *5   Relevance to geological CO₂ storage*
1080 The study of chimneys as potential fluid flow systems is highly relevant to the risk assessment of future
1081 CCS operations. For the assessment of a prospective CO_2 storage site, a site characterisation is first
1082 conducted to understand the potential containment risks, based on pre-existing seismic, well and
1083 environmental baseline data (e.g., Furre et al., 2019b). As the project progresses in maturity, additional
1084 data may be acquired based on identified risks or uncertainties. Containment risks are commonly
1085 identified using a bowtie risk assessment, where monitoring and modelling activities are implemented
1086 as barriers to reduce the likelihood of a top event (Dean and Tucker, 2017). A top event may be
1087 described as the unintended migration of CO_2 from a primary or a secondary sealing layer. In this
1088 context, chimneys could be considered as one such risk element. Fluid escape through
1089 abandoned/legacy wells and faults are other common risk elements that require consideration (IPCC,
1090 2005).
1091   If chimneys are identified as a potential threat from the initial site characterisation (based on
1092 existing data), stakeholders would be required to follow a process to determine unknown parameters
1093 which may contribute to the containment risk. Figure 14 demonstrates a potential approach to this,
1094 where the findings of our multi-scale approach to determining chimney parameters (Section 4; Tables
1095 1 and 2) are integrated into an existing Measurement, Monitoring and Verification (MMV) risk-based
1096 decision framework (Dean & Tucker, 2017). The outstanding risk question is defined as specifically as
1097 possible, and the unknown factors which contribute to this are separated from the parameters which are
1098 sufficiently well resolved from pre-existing resources. The remaining unknown factors, which may
1099 include fracture connectivity, permeability, and/or fluid volume flux and composition, are then targeted
1100 using appropriate methods drawn from Section 3, in order to mitigate the outstanding risks. The
1101 selection of which method(s) to use is based on each methods' suitability for determining the parameters
1102 of interest (Table 1; Fig. 13), at the appropriate resolution and scale for the problem (Table 2), and any
1103 potential dependencies it may have (Table 1). Tailored deployment of new resources is then conducted,
1104 in a monitoring step. This may, for example, involve further data acquisition and/or modelling studies.
1105 Alternatively, this could also include the re-processing or re-appraisal of existing data or models. In
1106 order to optimise the risk assessment process, this step should factor both the additional cost and time
1107 of further acquisition against the benefits of obtaining the new information using these approaches. The
1108 staging of resource deployment is also important at this stage, such that the maximum amount of new
1109 information is resolved using the minimum necessary additional resource cost/time. It would not,
1110 therefore, necessarily be either feasible or desirable to use all of the methods discussed in this study,
1111 highlighting that stakeholders need to efficiently determine the parameter-specific traits they require
1112 for appropriate de-risking of the chimney. The outcomes of the monitoring step are then used to re-
1113 appraise and verify the containment risk-level attributed to the chimney, before a decision is made. If
1114 this verification stage indicates that all of the outstanding risks have not yet been constrained
1115 sufficiently, the process should be repeated until they have. In this respect, the risk assessment and
1116 mitigation process can be considered to be a cycle (Figure 14).
1117   Each prospective CO_2 storage site will have unique characteristics and, therefore, will be
1118 different. However, potential risks need to be assessed holistically, which will result in different
1119 resource deployment choices for different sites. Based on the outline workflow we have described, and
1120 using Tables 1 and 2 as a guide, we can consider a number of simple examples which could be resolved
1121 using this approach. If a fracture network at a spatial scale of 10s of m was deemed to be the greatest

1122 threat/uncertainty for prospective CCS operations, then seismic reflection or seismic tomography would
1123 be the most suitable method to use, while CSEM data may also assist in determining fracture
1124 connectivity and fluid content. If the sediment matrix porosity-permeability or the effects of
1125 microfractures were the principal cause of concern, laboratory experiments and/or modelling, using
1126 appropriate field analogues to define the input parameters, would be the optimal approach. As a final
1127 example, if CO_2 emission and flux rate from the seabed over a spatial scale of >1 km were the greatest
1128 threat/uncertainty, active acoustics would be the most appropriate method to use.

1129 Alternatively, further data acquisition may not be required. In the case of the Goldeneye
1130 prospective storage site, located in the Outer Moray Firth Basin, Central North Sea, a chimney-like
1131 feature was observed during the risk assessment phase. However, rather than further data acquisition,
1132 the first monitoring step applied was to conduct high resolution re-processing of existing data, alongside
1133 pre-stack interpretation. Together, these approaches resolved the issue sufficiently, finding that the
1134 observed feature instead represented a seismic imaging artefact caused by a glacial tunnel valley,
1135 without the need to acquire additional data (Dean et al., 2015).

1136 Active natural methane escape is observed directly within the shallow subsurface of the
1137 exemplar chimney at the Scanner pockmark complex in the North Sea. However, prospective CO_2
1138 storage reservoirs are more commonly located at greater depth and are capped by several sealing layers,
1139 for example the storage units at Sleipner are located at a depth of ~800-1000 mbsf. Therefore,
1140 understanding the role of chimneys in applied CCS environments may also represent a deeper
1141 subsurface problem. Compared to shallow chimneys, deeper chimneys may exhibit a number of
1142 differences, such as 1) increased stress - fluid pressure - temperature conditions; 2) the fluid of interest
1143 may be in a different phase (liquid compared to gas); and 3) changes in the sediment and pore fluid
1144 composition. At greater depths (higher effective stresses) there is likely to be more consolidated
1145 material, which may result in reduced porosity-permeability of the sediment matrix. Moreover, fracture
1146 apertures tend to decrease with increasing effective stress (increasing depth). Therefore, if a chimney
1147 existed at greater depths, it is more likely to have lower effective permeability, although this is
1148 dependent on the rock material properties and microscopic fracture roughness (e.g., McDermott &
1149 Kolditz, 2006; Rutqvist, 2015). At greater depths the chimney would need to contain considerable
1150 stress-persistent fracture apertures to be deemed a risk. Further research is required to more accurately
1151 constrain the differences expected between deeper and shallower chimneys. The study of deeper
1152 chimneys may also alter the experimental approach. For example, a number of the applied geophysical
1153 methods lose resolution with depth, due to the increasing attenuation of higher frequency signals that
1154 are required to image structures at shorter length scales (Resnick, 1990). However, by applying the
1155 principles discussed here and in Figure 14, a multi-component, appropriate target-scale risk appraisal
1156 approach can be developed for a chimney structure located at greater depth.

1157 Overall, our integrated multi-scale experimental approach can be incorporated into pre-existing
1158 measurement, monitoring and verification approaches (e.g., Dean and Tucker, 2017). Future monitoring
1159 approaches must also be supported by robust baseline surveys and detailed understanding of the risks
1160 of CO_2 emissions that extend into the marine environment (Blackford et al., 2014, 2015; Flohr & Schapp
1161 et al., this volume). Our understanding of fluid flow through chimneys must be improved to decrease
1162 containment risks at prospective storage sites and thereby realise the potential of CCS for mitigating
1163 global warming.

1164

1165 **6 SUMMARY**
1166 Chimneys (also referred to as seismic chimneys and/or pipes) may represent an important class of
1167 subsurface fluid escape pathway. The study and understanding of chimneys are highly important to risk
1168 assessments for potential CCS applications. To this end, the CHIMNEY and STEMM-CCS research
1169 programmes have investigated chimneys in the North Sea. The results of these investigations will

1170 contribute to the further development of models for the understanding of fluid flow through such
1171 structures.
1172   In this paper we have described an approach for the multi-scale, multi-method geophysical
1173 characterisation of chimneys within sedimentary basins, using the Scanner pockmark as a case study.
1174 In the development of this multi-method approach, we note the following:

- While individual experimental approaches, conducted in the field or in the lab, are able to determine one or more of the physical properties of chimneys and their role in fluid flow, integration between different methods is required to fully characterise the system.
- Many of the described approaches rely on having suitable constraints and calibration from other methods. It is necessary, therefore, to ground-truth the methods, both in the field and in the laboratory, wherever possible, in order to ensure that conclusions determined are robust.
- The method approaches available are applicable at different physical length scales and resolution, with a common trade-off between these two factors. Hence, it is also important that the techniques used to study fluid flow structures are applied across scale and resolution ranges, as well as different temporal scales, in order to build a holistic and sufficiently detailed understanding.
- We propose that the integrated methodology presented to study the chimney beneath Scanner pockmark is applicable beyond this specific study area, and thus our work contributes to a wider understanding of this class of feature and its potential importance in fluid migration.

TABLES

Table 1. Summary of the methods used for the characterisation of a chimney, displaying the assessed parameters and the method specific traits. The parameters used for complete characterisation of a chimney include: 1) fracture geometry, orientation, connectivity and subsurface structure; 2) physical properties – e.g. porosity, permeability and resistivity; and 3) fluid presence, distribution, composition and flux/ flow rate. A method can (green) or cannot (red) be used to assess a given parameter. The traits of each method include: a) temporal applicability - whether the method can be applied at different times to observe temporal variability at the site; b) co-dependencies - whether a method can be used for calibration and constraint of another method; c) time and resource intensiveness - whether data can be produced with a given amount of resources on the timescale of weeks (low), months (medium) or greater than six months (high); and d) cost - a relative economic cost scale for completion (that can be qualitatively described as a method requiring desk time (low), laboratory time (medium) and/or ship time (high)).

Methods		Section	Method (Site) Parameters			Method traits		
			Fractures & structure	Physical properties	Fluids	Temporal applicability	Co-dependencies	Resource use
Acoustic (A)	Active acoustic	3.7	Red	Red	Green	Green	None	Low
Passive seismic (PS)	Passive seismic	3.6	Red	Red	Green	Green	None	Medium
Seismic reflection (SR)	2D seismic reflection	3.2.1-3.2.3	Green	Red	Green	Red	ST	Low-medium
	3D seismic reflection	3.2.1-3.2.3	Green	Red	Green	Red	ST	Medium
	4D/time-lapse seismic reflection	3.2.4	Green	Red	Green	Green	ST	Medium
Seismic tomography (ST)	Travel time tomography & FWI	3.3	Green	Green	Red	Red	SR	Medium-high
Seismic anisotropy (SA)	Shear wave splitting	3.4.1	Green	Green	Red	Red	SR, ST	High
	Seismic attenuation	3.4.2	Green	Green	Green	Red	SR, ST	High
	Ambient noise anisotropy	3.4.3	Green	Red	Red	Red	SR, ST	High
Controlled source electromagnetics (CSEM)	CSEM	3.5	Red	Green	Green	Red	SR	High
Direct sampling (DS)	Drilling & core analysis	3.8.1	Red	Green	Green	Red	SR	Medium
	Outcrop analogues	3.9	Green	Green	Red	Red	None	Low-medium
Laboratory experiments (LE)	Laboratory experiments	3.8.2	Green	Green	Green	Red	DS	Low
Modelling (M)	Numerical modelling	3.10	Green	Green	Green	Green	DS, SR	High

1218 **Table 2.** Summary of the resolution (a) and the length scale (b) over which each geophysical method can be used to assess parameters, for complete
1219 characterisation of chimneys. Note that for methods subject to frequency-dependent attenuation with increasing depth penetration (e.g. seismic, CSEM), we
1220 show here the full range of resolutions and length scales. Thus, as depth penetration increases, the smallest achievable resolution and length scale will also
1221 increase.
1222
1223 a)

Methods		Resolution					
		≤cm	dm	m	10s m	100s m	km
Acoustic (A)	Active acoustic			▓▓			
Passive seismic (PS)	Passive seismic			n/a			
Seismic reflection (SR)	2D / 3D / time-lapse reflection		▓▓▓▓	▓▓▓			
Seismic tomography (ST)	Travel time tomography & FWI			▓▓	▓▓▓	▓	
Seismic anisotropy (SA)	Shear wave splitting				▓▓		
	Seismic attenuation				▓▓		
	Ambient noise anisotropy					▓▓	▓
Controlled source electromagnetics (CSEM)	CSEM				▓▓	▓▓	▓
Direct sampling (DS)	Drilling & core analysis	▓▓▓	▓▓				
	Outcrop analogues	▓▓▓	▓▓				
Laboratory experiments (LE)	Laboratory experiments	▓▓▓	▓▓				
Modelling (M)	Numerical modelling	▓▓▓	▓▓▓	▓▓▓	▓▓▓	▓▓▓	▓

1224

1225   b)

Methods		Length Scale					
		≤cm	dm	m	10s m	100s m	km
Acoustic (A)	Active acoustic			■	■	■	■
Passive seismic (PS)	Passive seismic					■	■
Seismic reflection (SR)	2D / 3D / time-lapse reflection			■	■	■	■
Seismic tomography (ST)	Travel time tomography & FWI				■	■	■
Seismic anisotropy (SA)	Shear wave splitting				■	■	■
	Seismic attenuation				■	■	■
	Ambient noise anisotropy					■	■
Controlled source electromagnetics (CSEM)	CSEM			■	■	■	■
Direct sampling (DS)	Drilling & core analysis			■	■	■	
	Outcrop analogues	■	■	■	■	■	
Laboratory experiments (LE)	Laboratory experiments	■	■				
Modelling (M)	Numerical modelling	■	■	■	■	■	■

1226

FIGURES

a)

b)

Figure 1. STEMM-CCS and CHIMNEY study area. a) Regional map of northern North Sea plotted over GEBCO (2019) bathymetry. Location of the Scanner and Goldeneye experiment sites, and active Sleipner CCS storage site are labelled. Yellow box indicates location of UK North Sea licence box 15/25. Dashed black line demarcates boundary between UK (to W) and Norway (to E) exclusive economic zones (200 nm). b) Ship-acquired swath bathymetry of the study area, around Scanner and Challenger pockmark complexes. Dashed black box indicates location of inset. Inset: Detailed bathymetry of Scanner pockmark complex. Diamonds and triangles indicate locations of RD2 drilling locations and gravity coring sites respectively. Orange outline indicates acquisition during cruise leg MSM78. Black outline indicates acquisition during cruise leg POS518.
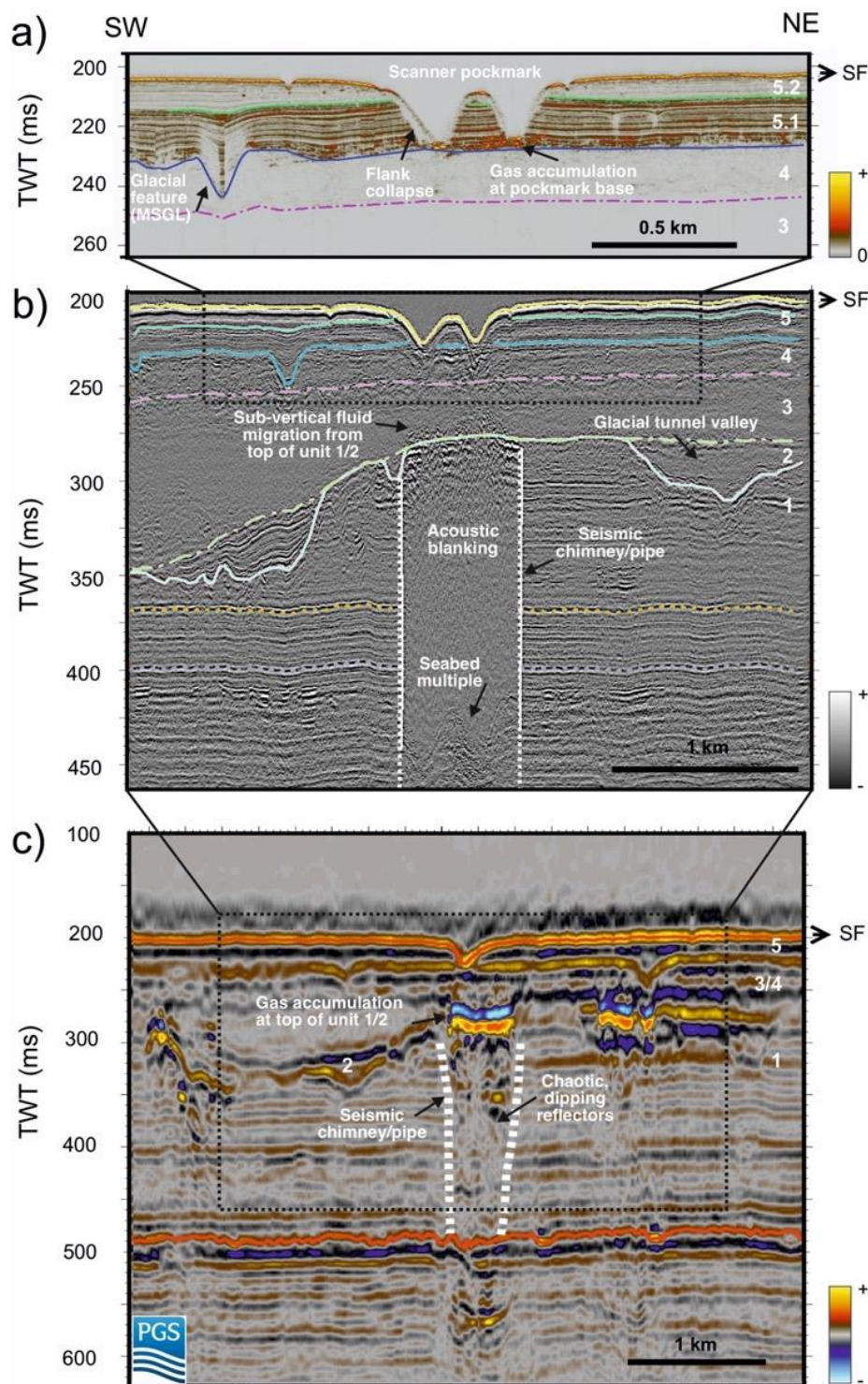
Figure 2. Seismic stratigraphy of the Scanner pockmark region, after Böttner et al. (2019). Profiles shown extend from southwest to northeast across the Scanner pockmark complex. a) Sub-bottom profiler seismic reflection data. b) 2D seismic reflection data acquired using Sparker source. c) 3D seismic reflection data. Interpreted seismic units S1 to S5 are shown. S1 – Aberdeen Ground Fm., S2 – Ling Bank Fm., S3-4 – Coal Pit Fm. (S3 – Coal Pit & S4 – Last Glacial Maximum deposits (LGM)), S5 – Witch Ground Fm. (S5.1 – lower Witch Ground Member, S5.2 – upper Witch Ground Member). Light blue line = top S1; green dashed line = top S2; pink dashed line = top S3; blue line = top S4; green solid line = top S5.1 and yellow line = top S5.2 / SF = Seafloor. Outline of a chimney is displayed with white dashed line.
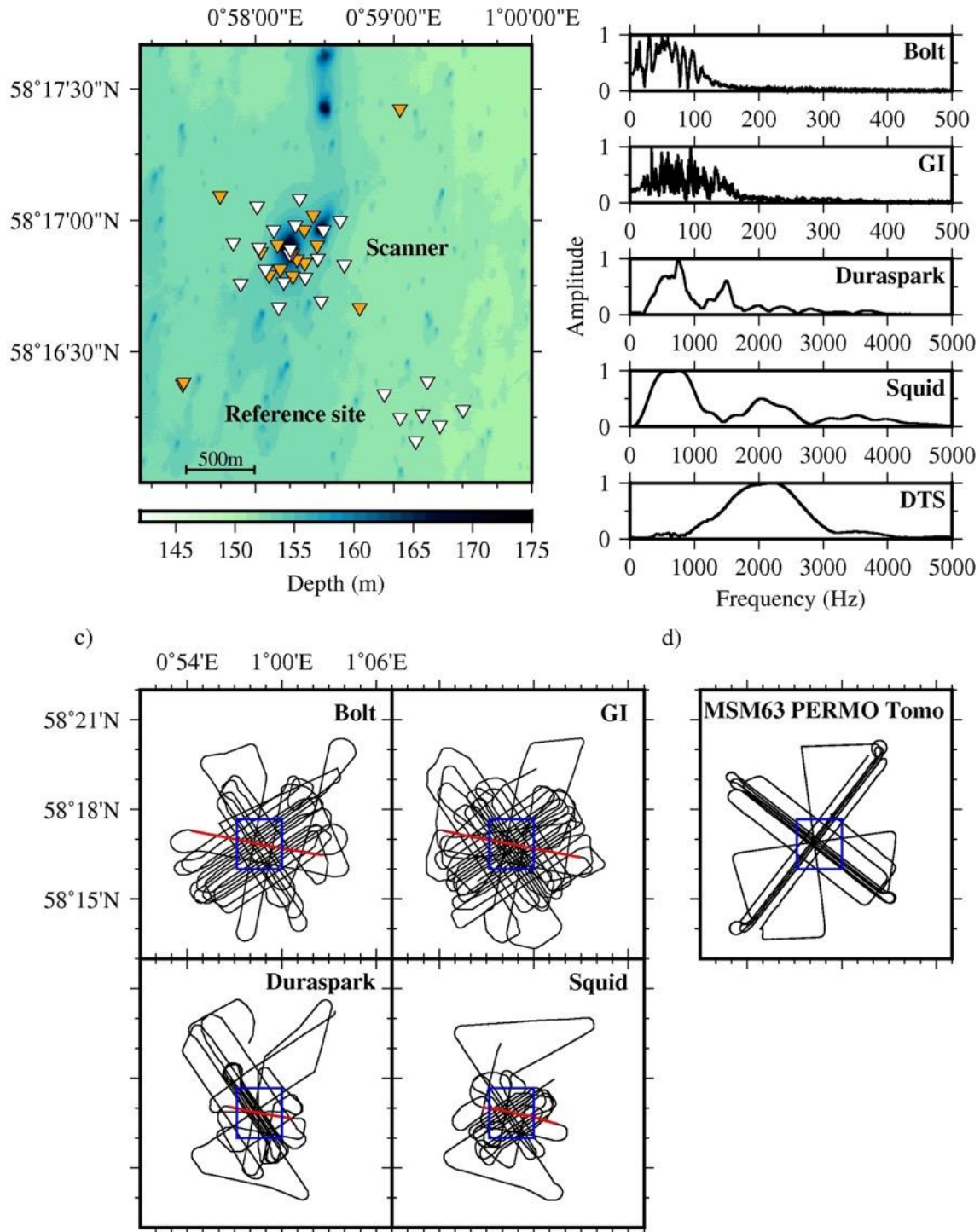
1248
Figure 3. Layout of the Scanner pockmark seismic experiments. a) OBS locations for JC152 seismic
1250 tomography, anisotropy and passive seismic experiments (white triangles), and MSM63 seismic
1251 tomography experiment (orange triangles). b) Far-field source frequency spectra of the seismic sources
1252 used in the JC152 tomography and anisotropy experiments. c) Seismic acquisition tracks for JC152,
1253 with sources labelled, showing the multi-azimuthal geometry of source coverage. Only the air-gun (Bolt
1254 and GI) and surface sparker (Duraspark and Squid) sources are shown. Blue box shows extent of area
1255 shown in a). Red line indicates location of the profiles shown in Fig. 4. d) Acquisition track for the
1256 MSM63 acquisition.
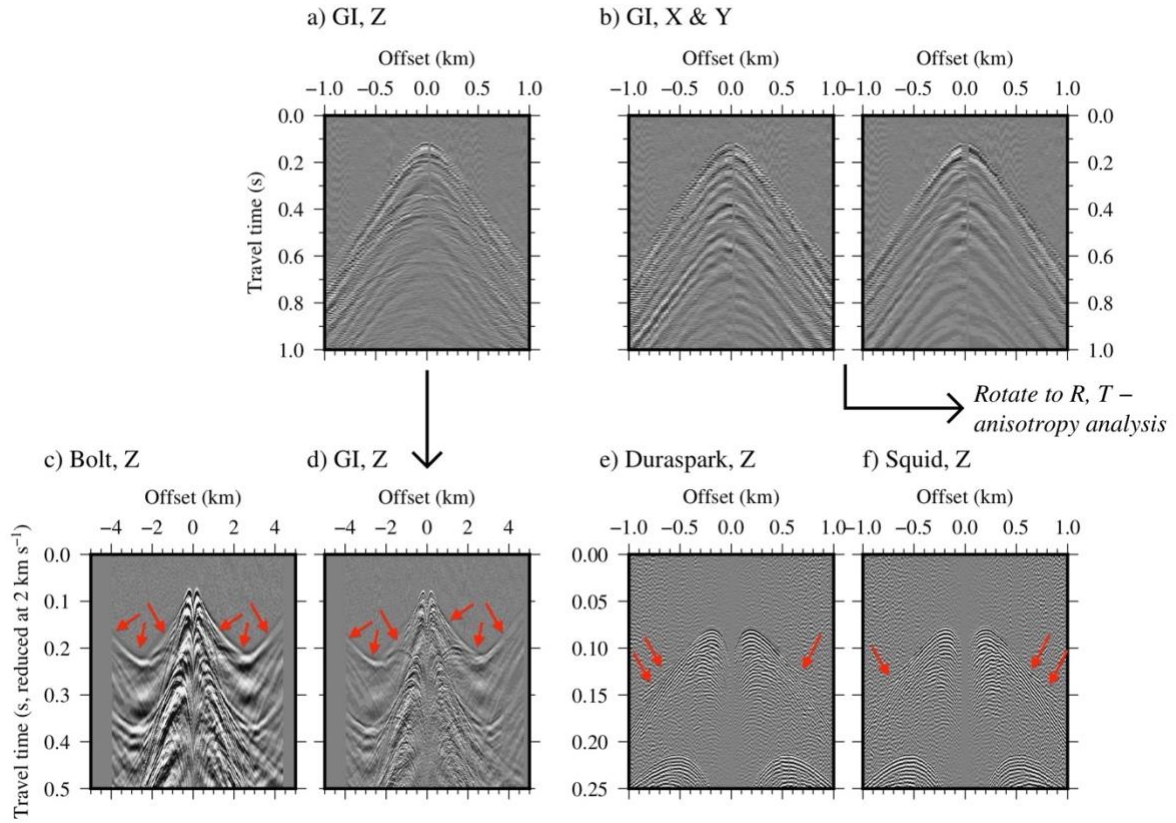
Figure 4. Example OBS data from the JC152 seismic tomography and anisotropy experiments. All records shown are from OBS 1, located within Scanner pockmark, and are approximately E-W oriented (red lines, Fig. 3c). a) Z geophone components, GI source. b) X & Y geophone components, GI source, used for seismic anisotropy analysis. c)-f) Z component (c) Bolt, (d) GI, (e) Duraspark sparker, and (f) Squid sparker, plotted with reduction velocity of 2 km s⁻¹. Note the different horizontal and vertical scales for the airgun vs. sparker sources. Bolt and GI airgun records plotted with a 5-15 Hz low-pass filter. Sparker records plotted with a 100-200 Hz low-pass filter. Arrows show location of emergent (refracted) arrivals.
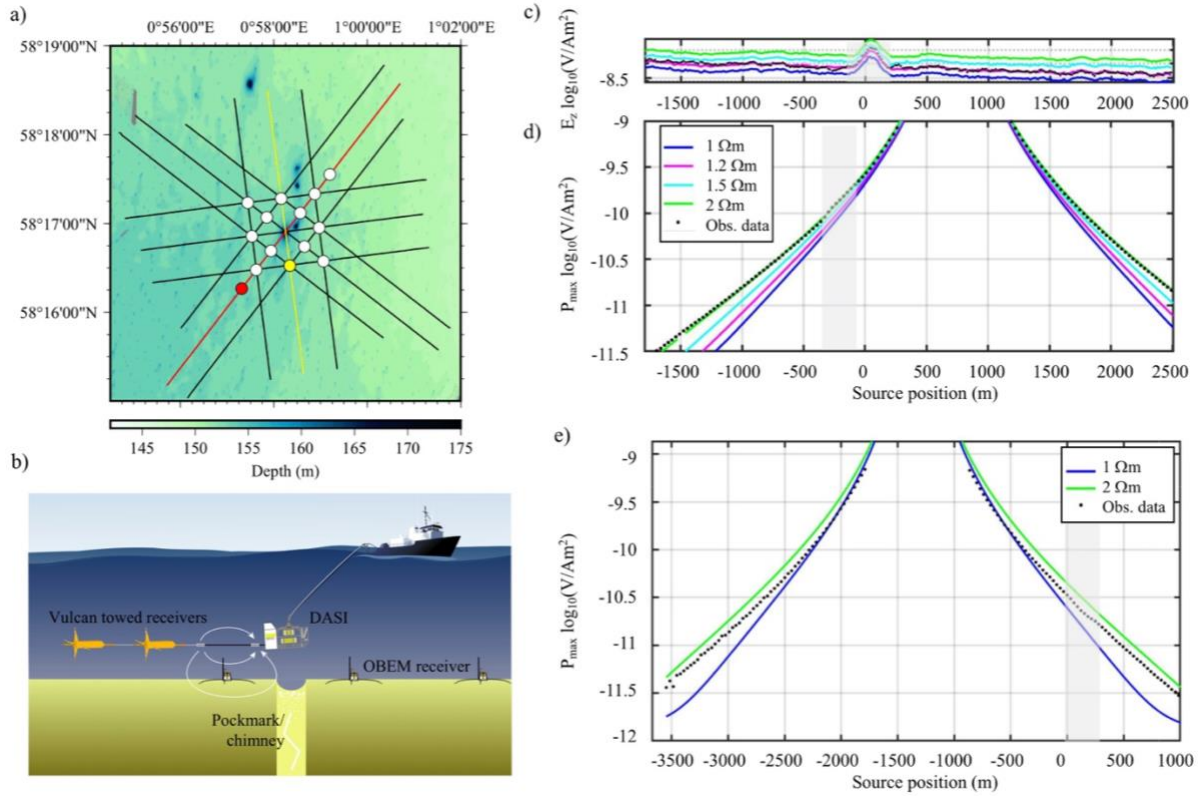
Figure 5. Scanner pockmark CSEM experiment. a) Bathymetry map with data acquisition profiles (black) and OBEM receiver locations (circles). Data in c-e) are shown for profiles and OBEM instruments coloured in yellow (c-d) and red (e), respectively. b) Sketch of survey setup, with towed DASI source, towed Vulcan receivers and three component OBEM seafloor receivers. c-d) Example data at 1 Hz from N to S trending profile (yellow line) for the closest towed receiver c) and the OBEM d) (yellow circle on a). The x axis shows the source position (black antenna with white field lines in b)) along profile, with the location of Scanner pockmark set at 0 m. The OBEM in d) is located at ~700 m along profile. The observed data (black dots), the vertical electric field amplitude (E_z) and the total horizontal electric field amplitude (P_{max}) respectively, are compared to 2D (c), towed receiver) and 1D (d), OBEM) forward modelled data (coloured lines) for a subsurface with half-space resistivities of 1 to 2 Ωm. The towed receiver data, sensitive to the top ~50-100 m, agree well with predicted data for a 1.2 Ωm subsurface resistivity, while the OBEM data at larger offset to the source agree better with higher resistivities, indicating an increase in resistivity with depth. In c), the location of the grey box corresponds to observed E_z values when the transmitter is above the pockmark. In d), a slight increase of P_{max} at ~-200-400 m (highlighted with grey box), however, may indicate a localised increase of resistivities in the subsurface. e) OBEM instrument P_{max} data example from SW to NE trending profile (yellow line). At about 100-400 m from the Scanner pockmark position, a localised increase of P_{max} is observed, potentially related to an increase in resistivity in the subsurface in the vicinity of the seismic chimney.
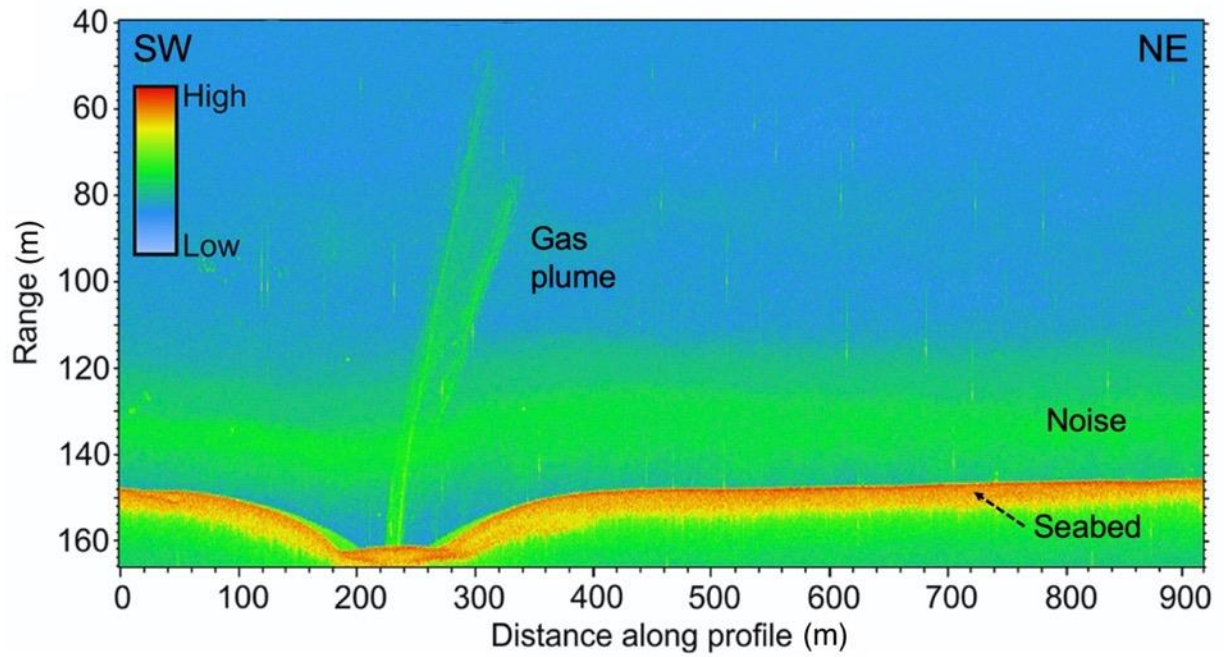
Figure 6. Hydro-acoustic imaging of the Scanner pockmark gas plume, using EM712 echosounder data at a frequency range of 40-100 kHz. Highest backscatter is displayed in red (seabed). The gas plume is clearly visible as a strong (green) zone of backscatter emanating from the pockmark, rising to the thermocline at ~40 m below the sea surface. Figure adapted from Böttner et al. (2019).

1291
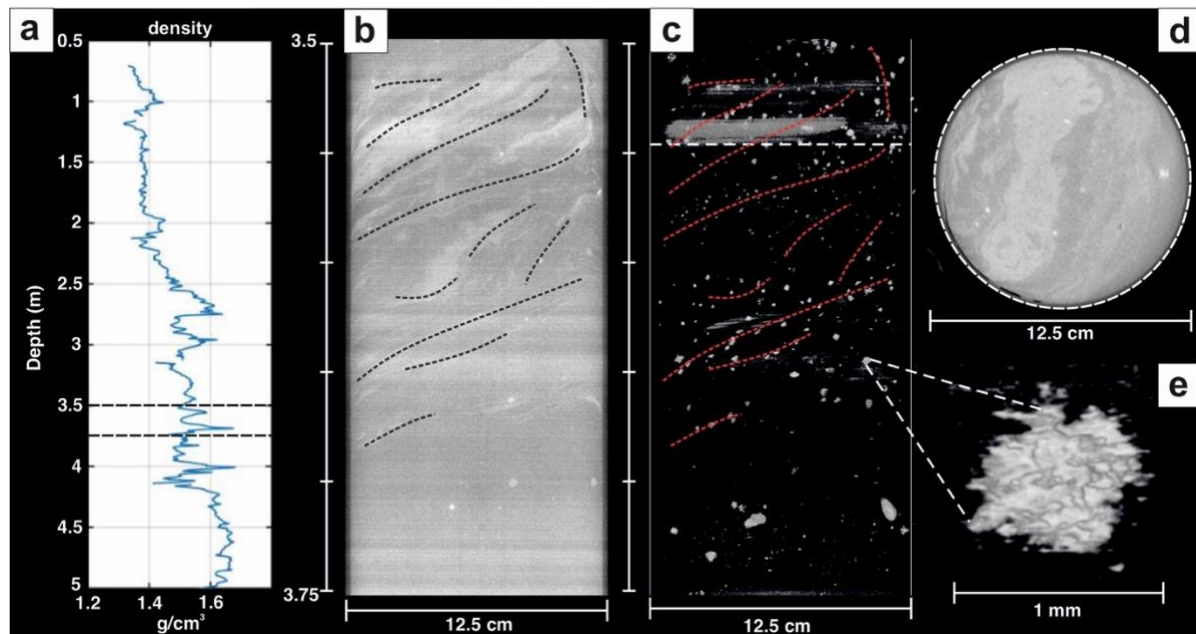
1292
1293 **Figure 7**. Gravity cores of sediments recovered from directly beneath East Scanner Pockmark (GC17;
1294 Fig. 1c) during the MSM78 expedition. The cores were analysed using a) Multi-Sensor Core Logging
1295 (MSCL), which includes density data and b-e) X-ray micro-CT analysis. b) and d) Analysis of a 25 cm
1296 length x 12.5 cm diameter core section composed of fine silt. Coarser grained horizons (lighter grey)
1297 show evidence of fluidisation structures and layering, picked out by the dotted lines. c) Same image as
1298 b) but with lower density material removed, showing the presence of disseminated iron sulphide (bright
1299 spots, close-up shown in e) that has precipitated within the coarser grained horizons. The presence of
1300 iron sulphide is indicative of transport of methane-rich fluids through the coarser grained sediment
1301 horizons.
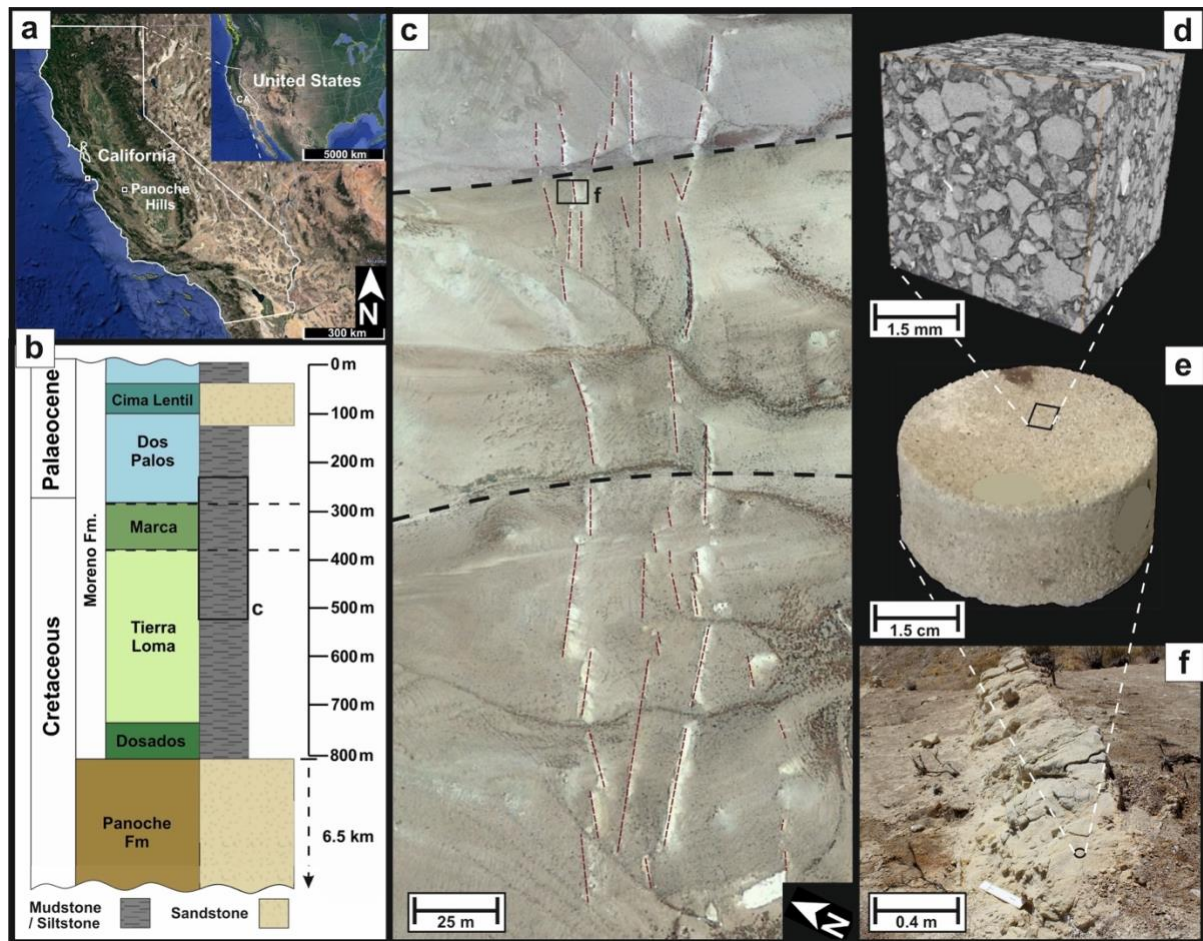
Figure 8. Field outcrop analogue of a fluid escape system in the Panoche Hills, Central California. a) Map of the Panoche Hills field location. b) Lithostratigraphy of the Panoche Hills which includes the Panoche Fm., comprised of up to 6.5 km of turbiditic sandstone, overlain by greater than 600 m of mudstone and siltstone cap rock / overburden sealing units. c) Map view of sand filled fractures intruding sub-vertically through the sealing units of the Moreno Fm. The map view is analogous to the spatial extent mappable with UAVs. d-f) Direct sampling and observation of a sand-filled fracture at different length scales, which includes d) pore-scale XCT analysis and e) core-scale laboratory analysis.
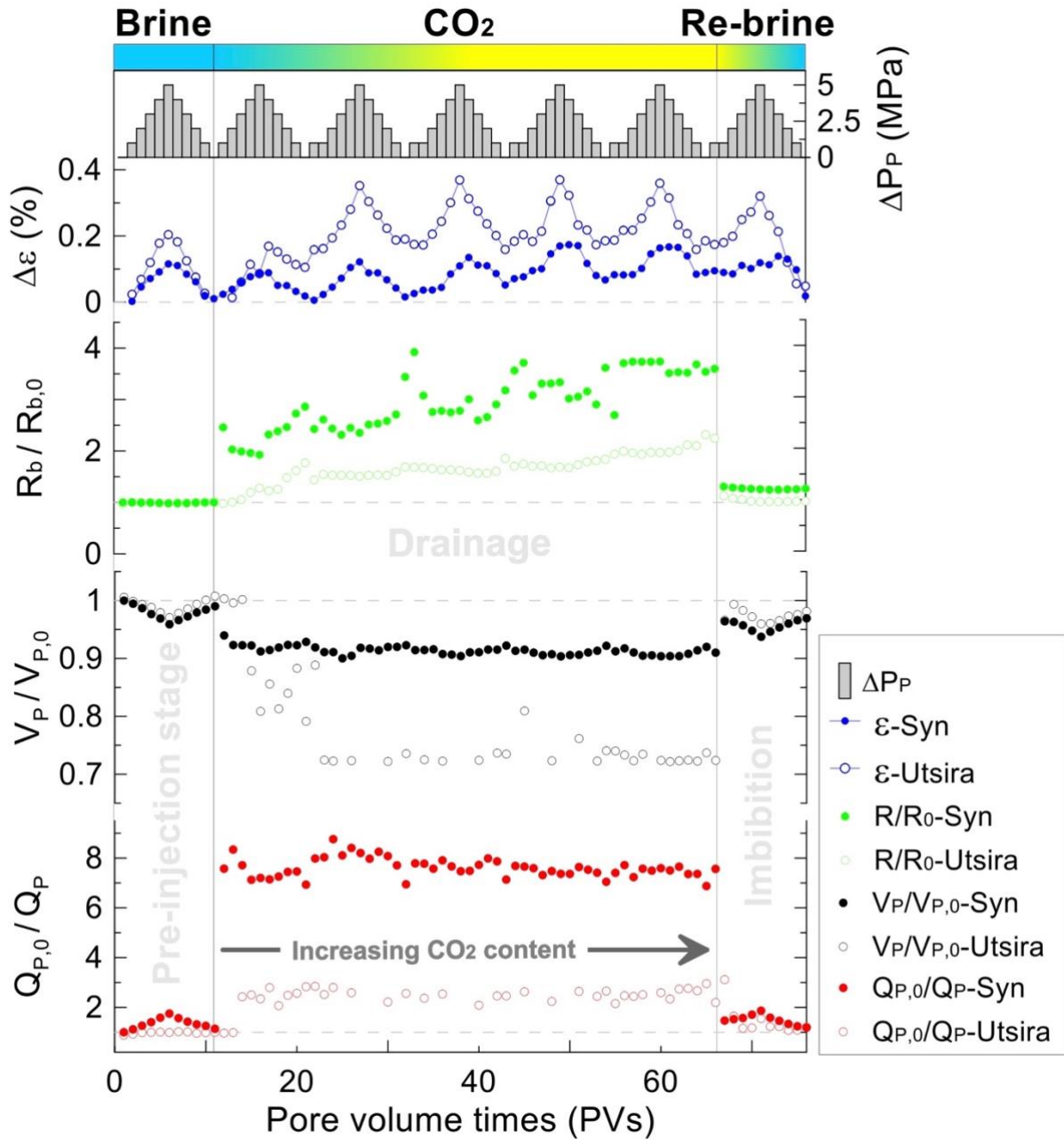
Figure 9. Laboratory flow-through experimental results. Brine-CO_2 flow-through tests were conducted for two samples, a 38% porosity synthetic sandstone (Syn) and an intact core sample from Utsira Sand formation (Sleipner field). The tests simulate cyclic overpressure scenarios (ΔP_P) in a Sleipner-like CO_2 storage reservoir during pre-injection, CO_2 injection (drainage) and post-injection (imbibition) stages. Electrical resistivity, P-wave velocity, V_P, and P-wave attenuation, Q_P^{-1} are normalised with respect to the values at the original reservoir conditions (16.4 and 7 MPa of confining and pore pressure, respectively), and plotted together with volumetric strain, ε_v, versus pore volume (PV, i.e. injected fluid volume normalised to the sample pore volume). The results show the effect of rock consolidation on the elastic and transport properties of reservoir formations with similar petrophysical features but different degrees of cementation (i.e., weakly-cemented Utsira sand formation versus silica-cemented synthetic sandstone), and the evolution with the increasing CO_2 content. Figure adapted from Falcon-Suarez et al. (2018).
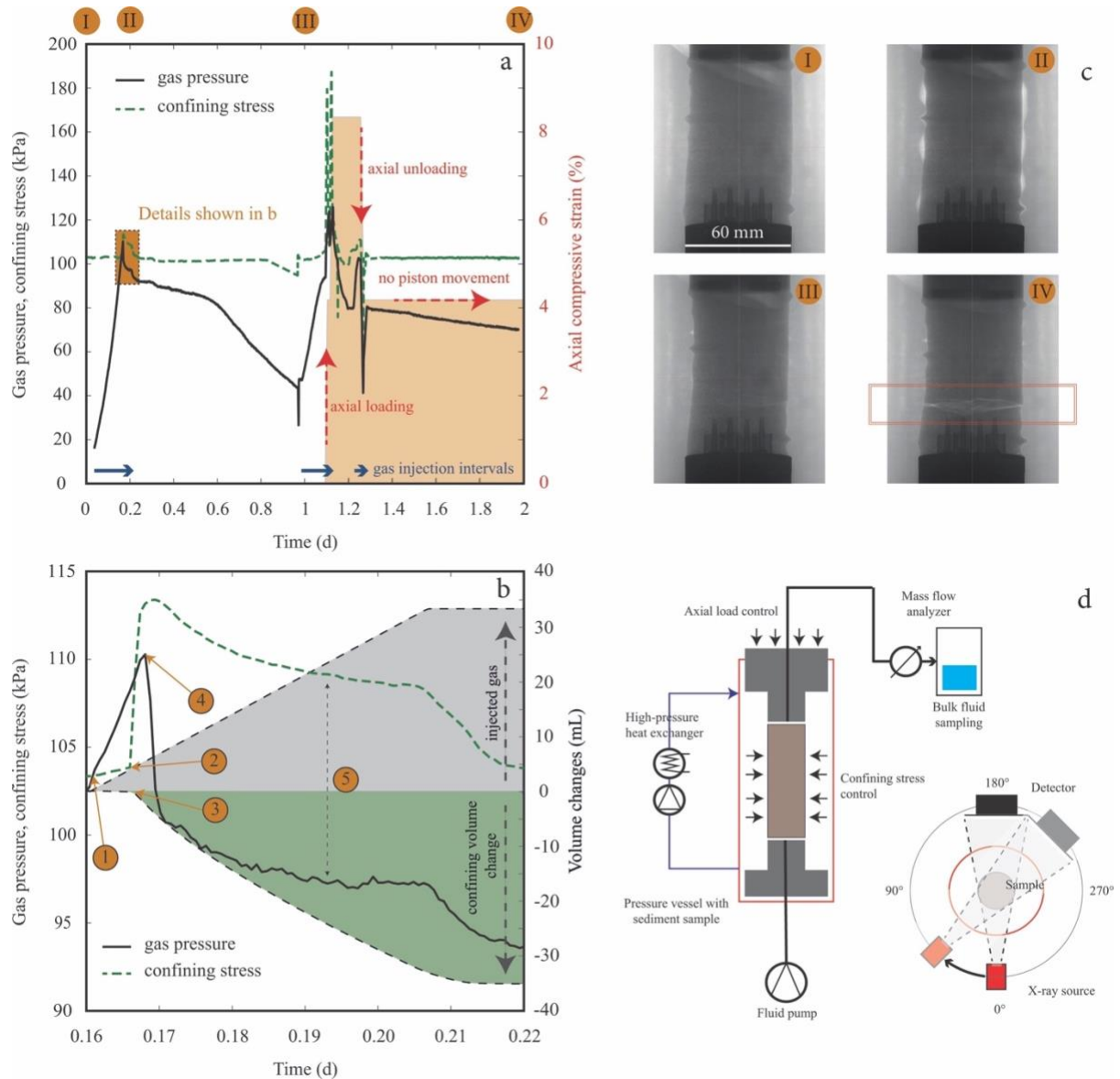
Figure 10. Fracture formation due to gas migration in poorly consolidated clay sediments. Flow through experiments were carried out on gravity core samples recovered during RV Poseidon cruise POS534 (Schmidt, 2019). Injection experiments were carried out with N_2 because of its low solubility compared to CO_2. a) Gas pressure and confining stress. b) Pressure-volume relations during and after fracture formation. c) X-ray projection images at different time points. d) Setup of the X-ray micro-CT imaging system. Gas was injected in intervals (dark blue arrows) followed by pressure dissipation periods. Fracture formation was rapid after gas pressure increased above the confining stress (1). After reaching a critical pressure for fracture formation, an increase in confining stress (2) triggered confining fluid removal (3). The gas pressure dissipated rapidly after fracture opening (4), which subsequently resulted in the accumulation of gas at the sample surface. The offset between confining stress and gas pressure during ongoing gas injection (5) likely resulted from measurement inaccuracies because all system components were rated for high-pressure operation.
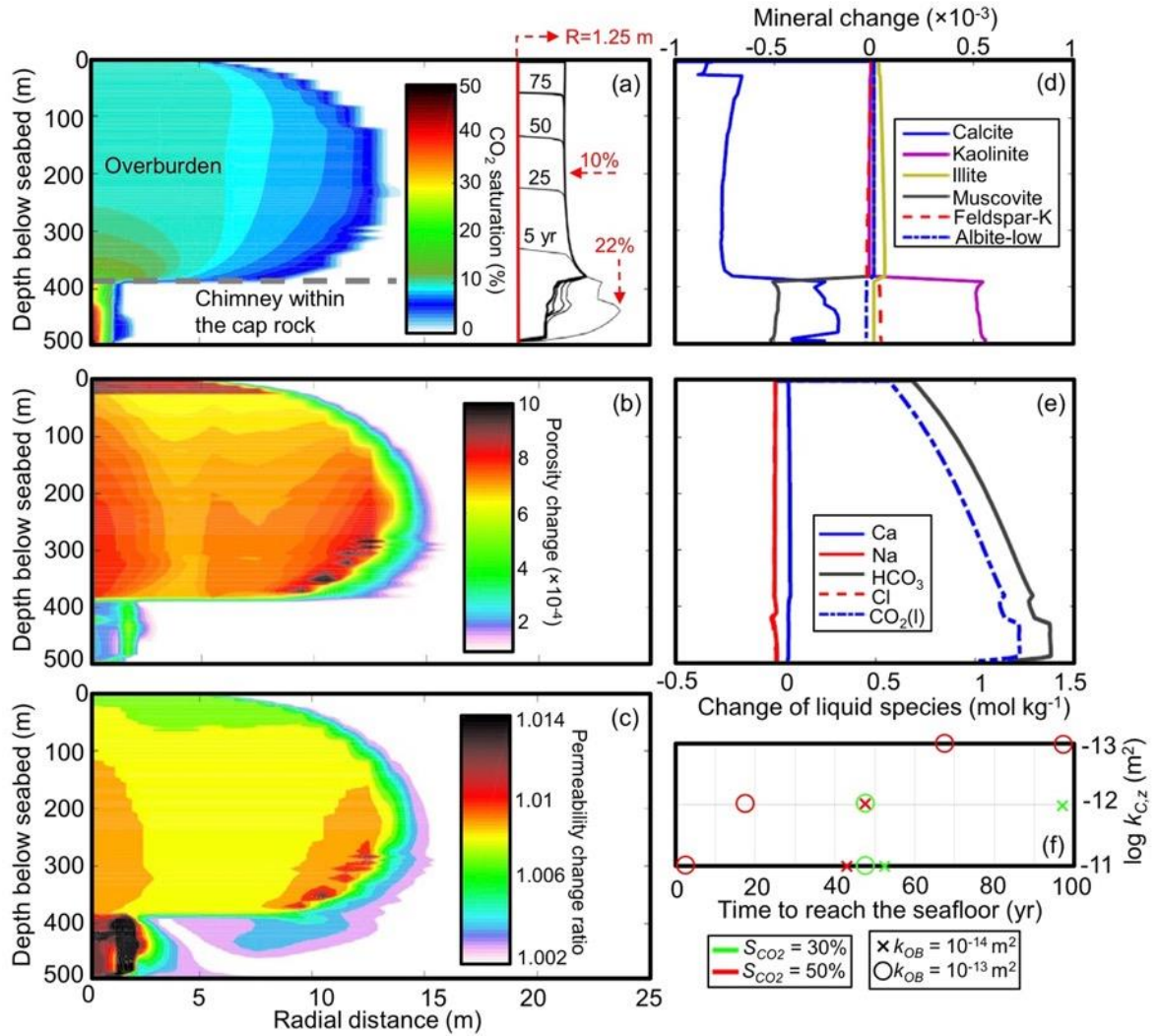
Figure 11. Reactive transport modelling of CO_2 migration through a generic chimney using the North Sea, Scanner pockmark complex as a proxy for pressure, temperature, geological, mineral and chemical conditions (adapted from Marin-Moreno et al., 2019). The model geometry comprises CO_2 injection at a radial distance of 0 m and depth below seabed of 500 m. The chimney extends vertically to the top of the cap rock (400 mbsf). Results are shown after 100 yr, with a constant injected CO_2 saturation of 50%, an overburden isotropic permeability of 10^{-13} m^2 and chimney vertical and horizontal permeabilities of 10^{-13} m^2, and 10^{-15} m^2. Variation of a) CO_2 saturation, b) porosity and c) permeability with depth and radial distance. Inset in a) shows the temporal evolution over 100 yr of CO_2 saturation with depth at a distance of 1.25 m from the injection point. Red numbers are CO_2 saturations. Changes in d) mineralogy and e) concentration of liquid species at a distance of 1.25 m from the injection point. f) Models of CO_2 gas reaching the seabed in less than 100 yrs for tested injected CO_2 saturations of 10%, 30% and 50%; overburden isotropic permeabilities of 10^{-13} m^2, and 10^{-14} m^2; and chimney vertical permeabilities ranging from 10^{-11} m^2 to 10^{-16} m^2 (ratios of chimney vertical to horizontal permeability from 1 to 1000 were tested). Figure adapted from Marin-Moreno et al. (2019).

40
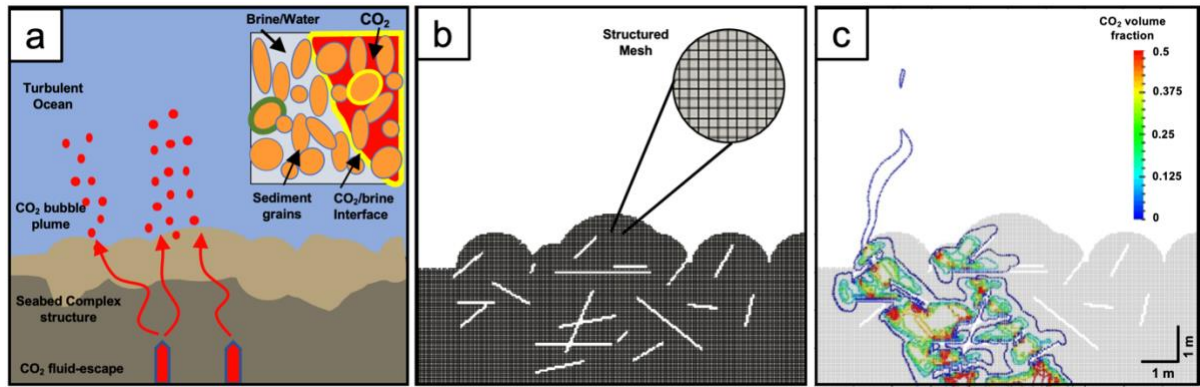
Figure 12. Computational fluid dynamic modelling of gas leakage through sub-seabed fracture network. Modelling has been conducted for CO_2 fluid escape. (a) Schematic of complex subsurface sediments, gas plume at a potential fluid escape site. (b) Simulation geometry. Lower (black) part of model is sediment (~4 m average thickness) with 1 cm thick, non-connected fractures (white). Upper part is the water column. c) Contoured gas volume fraction at time (snapshot) of gas dispersion through sediments into the ocean. Figure adapted from Saleem (2020).

1358

1359
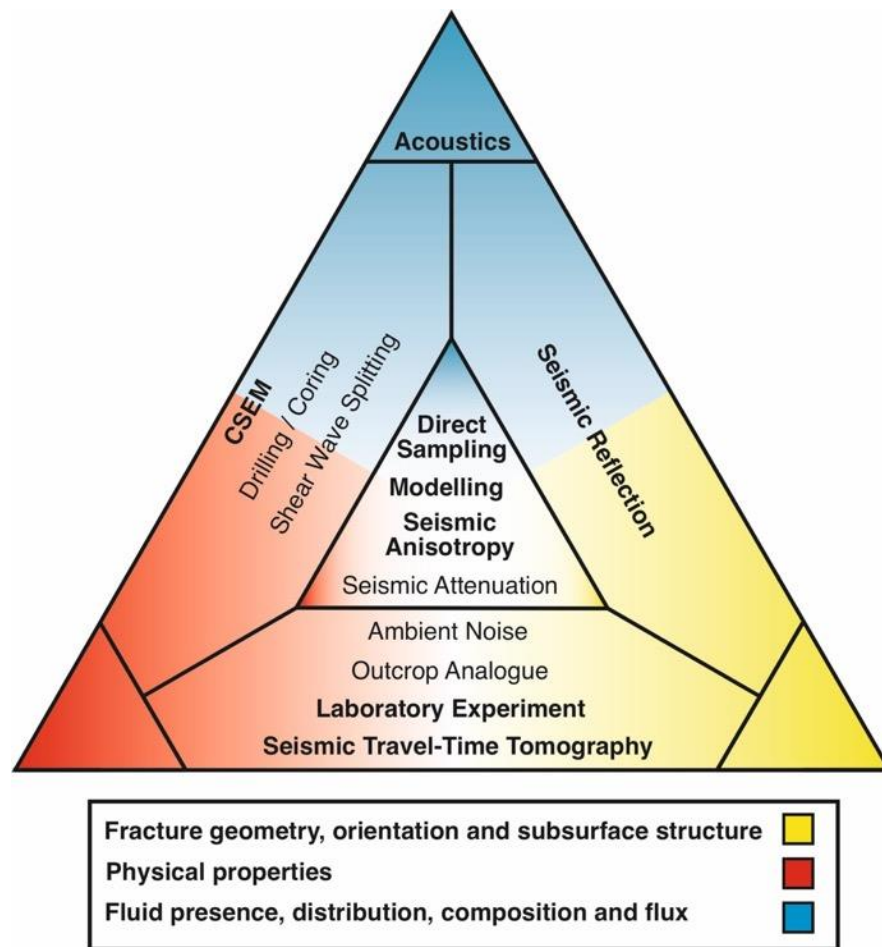
Figure 13. Summary of relationships between methods used and parameters investigated in the study of the chimneys beneath Scanner pockmark. Triangle plot highlighting the three main parameters (Table 1) used for characterisation of a chimney/fluid escape system, where each method is located within the regions of the triangle corresponding to the parameters it can be used to resolve.
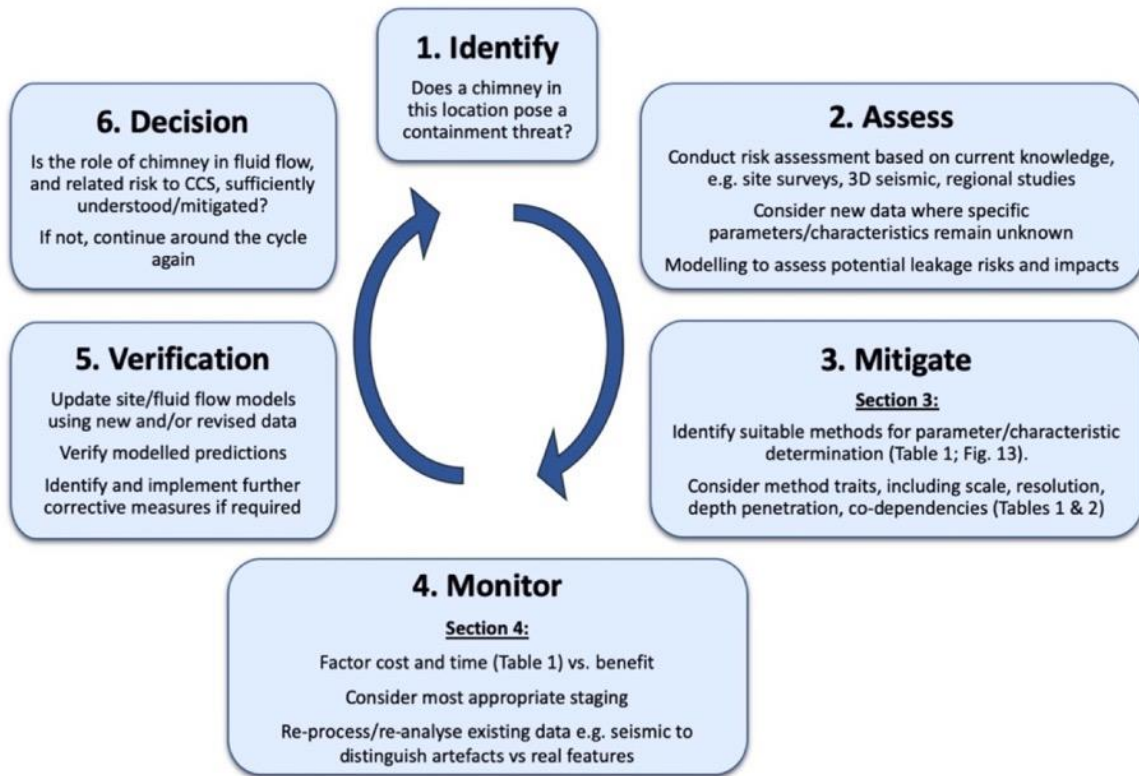
Figure 14: Outline of a decision-making cycle illustrating the steps in the risk-based assessment of a site where chimneys may pose a risk to potential CCS operations. The multi-parameter, multi-scale approach discussed in sections 3 and 4 of this paper should be used in steps 3 and 4, the mitigating and monitoring steps, in order to optimise the decision making process.

REFERENCES

Achterberg, E. & Esposito, M. (2018). RV POSEIDON Fahrtbericht / Cruise Report POS527: Baseline Study for the Environmental Monitoring of Subseafloor CO2 Storage Operations, Kiel-Kiel (Germany), 15.8.-3.9.2018. https://doi.org/10.3289/geomar_rep_ns_45_2018.

ACT Acorn Consortium. (2018). D08 East Mey CO2 Storage Site Development Plan 10196ACTC-Rep-26-01. https://actacorn.eu/sites/default/files/ACT%20Acorn%20East%20Mey%20CO2%20Storage%20Site%20Storage%20Development%20Plan%201.0.pdf.

Alvizuri, C., & Tanimoto, T. (2011). Azimuthal anisotropy from array analysis of Rayleigh waves in Southern California, Geophysical Journal International, 186, 3, Pages 1135–1151, https://doi.org/10.1111/j.1365-246X.2011.05093.x.

Amalokwu, K. (2016). Saturation effects on frequency-dependent seismic anisotropy in fractured porous rocks, Doctoral thesis, 168 pp, University of Southampton. http://eprints.soton.ac.uk/id/eprint/391107.

Amalokwu, K., Papageorgiou G., Chapman, M., & Best, A. I. (2017). Modelling ultrasonic laboratory measurements of the saturation dependence of elastic modulus: New insights and implications for wave propagation mechanisms, International Journal of Greenhouse Gas Control, 59, 148-159. https://doi.org/10.1016/j.ijggc.2017.02.009.

Andresen, K. J. (2012). Fluid flow features in hydrocarbon plumbing systems: What do they tell us about the basin evolution?. Marine Geology, 332, 89-108. https://doi.org/10.1016/j.margeo.2012.07.006.

Andrews, I. J., Long, D., Richards, P. C., Thomson, A. R., Brown, S., Chesher, J. A., & McCormac, M. (1990). The geology of the Moray Firth (Vol. 3). HMSO, London. http://pubs.bgs.ac.uk/publications.html?pubID=B01844.

Archie, G.E. (1952). Classification of carbonate reservoir rocks and petrophysical considerations, American Association of Petroleum Geologists Bulletin, 36(2), 278–298. https://doi.org/10.1306/3D9343F7-16B1-11D7-8645000102C1865D.

Arntsen, B., Wensaas, L., Løseth, H., & Hermanrud, C. (2007). Seismic modeling of gas chimneys. Geophysics, 72(5), SM251-SM259. https://doi.org/10.1190/1.2749570.

Arts, R., Eiken, O., Chadwick, A., Zweigel, P., Van der Meer, L., & Zinszner, B. (2004). Monitoring of CO2 injected at Sleipner using time lapse seismic data. In Greenhouse Gas Control Technologies-6th International Conference (pp. 347-352). https://doi.org/10.1016/j.energy.2004.03.072.

Attias, E., Weitemeyer, K., Minshull, T. A., Best, A. I., Sinha, M., Jegen-Kulcsar, M., Hölz, S. & Berndt, C. (2016). Controlled-source electromagnetic and seismic delineation of subseafloor fluid flow structures in a gas hydrate province, offshore Norway. Geophysical Journal International, 206(2), 1093-1110. https://doi.org/10.1093/gji/ggw188.

Attias, E., Amalokwu, K., Watts, M, Falcon-Suarez, I. H., North, L., Hu, G. W., Best, A. I., Weitemeyer, K. M., & Minshull, T. A. (2020). Gas hydrate quantification at a pockmark offshore Norway from joint effective medium modelling of resistivity and seismic velocity. Marine and Petroleum Geology, 113, 104151. https://doi.org/10.1016/j.marpetgeo.2019.104151.

Baasch, B., Müller, H., von Dobeneck, T., & Oberle, F. K. (2017). Determination of grain-size characteristics from electromagnetic seabed mapping data: A NW Iberian shelf study. Continental Shelf Research, 140, 75-83. https://doi.org/10.1016/j.csr.2017.04.005.

Bachu, S. (2000). Sequestration of CO_2 in geological media: criteria and approach for site selection in response to climate change. Energy conversion and management, 41(9), 953-970. https://doi.org/10.1016/S0196-8904(99)00149-1.

Bahorich, M., & Farmer, S. (1995). 3-D seismic discontinuity for faults and stratigraphic features: The coherence cube. The leading edge, 14(10), 1053-1058. https://doi.org/10.1190/1.1437077.

Baird, A.F., Kendall, J.M., & Angus, D.A. (2013). Frequency-dependent seismic anisotropy due to fractures: Fluid flow versus scattering. Geophysics, 78, WA111-WA122. https://doi.org/10.1190/geo2012-0288.1.

Bannari, R., et al. (2008). Three-dimensional mathematical modeling of dispersed two-phase flow using class method of population balance in bubble columns. Computers & Chemical Engineering. 32(12): p. 3224-3237. https://doi.org/10.1016/j.compchemeng.2008.05.016.

Barkved, O., Buer, K., Halleland, K. B., Kjelstadli, R., Kleppan, T., & Kristiansen, T. (2003). 4D seismic response of primary production and waste injection at the Valhall field. In 65th EAGE Conference & Exhibition (pp. cp-6). European Association of Geoscientists & Engineers. https://doi.org/10.3997/2214-4609-pdb.6.A22.

1423 Batsi, E., Tsang-Hin-Sun, E., Klingelhoefer, F., Bayrakci, G., Chang, E. T. Y., Lin, J.-Y., et al. (2019). Nonseismic
1424   signals in the ocean: Indicators of deep sea and seafloor processes on ocean-bottom seismometer
1425   data. Geochemistry, Geophysics, Geosystems, 20, 3882– 3900. https://doi.org/10.1029/2019GC008349.

1426 Bayrakci, G., Scalabrin, C., Dupré, S. et al. (2014). Acoustic monitoring of gas emissions from the seafloor. Part II:
1427   a case study from the Sea of Marmara. Mar Geophys Res 35, 211–229. https://doi.org/10.1007/s11001-014-
1428   9227-7.

1429 Behzadi, A., Issa, R.I., & Rusche, H. (2004). Modelling of dispersed bubble and droplet flow at high phase fractions.
1430   Chemical Engineering Science, 59(4): p. 759-770. https://doi.org/10.1016/j.ces.2003.11.018.

1431 Bensen, G.D., Ritzwoller, M.H., Barmin, M.P., Levshin, A.L., Lin, F., Moschetti M.P., Shapiro, N.M. & Yang, Y.
1432   (2007). Processing seismic ambient noise data to obtain reliable broad-band surface wave dispersion
1433   measurements, Geophysical Journal International, Volume 169, Issue 3, Pages 1239–
1434   1260. https://doi.org/10.1111/j.1365-246X.2007.03374.x.

1435 Benson, S.M. & Cole, D.R. (2008). CO2 Sequestration in Deep Sedimentary Formations, Elements, 4, 325-331.
1436   https://doi.org/10.2113/gselements.4.5.325.

1437 Berndt, C. (2005). Focused fluid flow in passive continental margins. Philosophical Transactions of the Royal Society
1438   A: Mathematical, Physical and Engineering Sciences, 363(1837), 2855-2871. https://doi.org/
1439   10.1098/rsta.2005.1666.

1440 Berndt, C., Chi, W. C., Jegen, M., Lebas, E., Crutchley, G., Muff, S., et al. (2019). Tectonic Controls on Gas Hydrate
1441   Distribution Off SW Taiwan. Journal of Geophysical Research: Solid Earth, 146(1), 54–21.
1442   http://doi.org/10.1029/2018JB016213.

1443 Berndt, C., Elger, J., Böttner, C., Gehrmann, R., Karstens, J., Muff, S. et al. (2017). RV MARIA S. MERIAN
1444   Fahrtbericht/Cruise Report MSM63-PERMO, Southampton–Southampton (UK) 29.04.-25.05.2017.
1445   https://doi.org/10.3289/GEOMAR_REP_NS_37_2017.

1446 Bialas, J., Bohlen, T., Dannowski, A., Eisenberg-Klein, G., Gassner, L, Gehrmann, R., Heeschen, K., Hölz, S., Jegen,
1447   M., Klaucke, Krieger, M., Mann, J., Müller, Ch., Prüßmann, J., Schicks, J., Schünemann, E., Schwalenberg, K.,
1448   Sommer, M., Smilde, P. L., Spangenberg, E., Trappe, H., & Zander T. (2020), Joint interpretation of geophysical
1449   field experiments in the danube deep-sea fan, Black Sea, Marine and Petroleum Geology, Volume 121.
1450   https://doi.org/10.1016/j.marpetgeo.2020.104551.

1451 Blackford, J., Stahl, H., Bull, J.M., Bergès, B.J.P., Cevatoglu, M., Lichtschlag, A., Connelly, D., James, R.H., Kita,
1452   J., Long, D., Naylor, M., Shitashima, K., Smith, D., Taylor, P., Wright, I., Akhurst, M., Chen, B., Gernon, T.M.,
1453   Hauton, C., Hayashi, M., Kaieda, H., Leighton, T.G., Sato, T., Sayer, M.D.J., Suzumura, M., Tait, K., Vardy,
1454   M.E., White, P.R. & Widdicombe, S. (2014). Detection and impacts of leakage from sub-seafloor deep
1455   geological carbon dioxide storage, Nature Climate Change, 4, 1011-1016. https://doi.org/10.1038/nclimate2381.

1456 Blackford, J., Bull, J.M., Cevatoglu, M., Connelly, D., Hauton, C., James, R.H., Lichtschlag, A., Stahl, H.,
1457   Widdicombe, S. & Wright, I.C. (2015). Marine baseline and monitoring strategies for carbon dioxide capture
1458   and storage (CCS). International Journal of Greenhouse Gas Control, 38, pp.221-229.
1459   https://doi.org/10.1016/j.ijggc.2014.10.004.

1460 Blackford, J., Alendal, G., Avlesen, H., Brereton, A., Cazenave, P. W., Chen, B., Dewar, M., Holt, J., & Phelps, J.
1461   (2020). Impact and detectability of hypothetical CCS offshore seep scenarios as an aid to storage assurance and
1462   risk assessment, International Journal of Greenhouse Gas Control, Volume 95,
1463   https://doi.org/10.1016/j.ijggc.2019.102949.

1464 Blomqvist, S. (1985). Reliability of core sampling of soft bottom sediment—an in-situ study. Sedimentology, 32(4),
1465   605-612. https://doi.org/10.1111/j.1365-3091.1985.tb00474.x.

1466 Boait, F. C., White, N. J., Bickle, M. J., Chadwick, R. A., Neufeld, J. A., & Huppert, H. E. (2012). Spatial and
1467   temporal evolution of injected CO2 at the Sleipner Field, North Sea. Journal of Geophysical Research: Solid
1468   Earth, 117(B3). https://doi.org/10.1029/2011JB008603.

1469 Boles, J. R., Clark, J.F., Leifer, I., & Washburn, L. (2001). Temporal variation in natural methane seep rate due to
1470   tides, Coal Oil Point area, California, Journal of Geophysical Research, 106(C11), 27,077–27,086.
1471   https://doi.org/10.1029/2000JC000774.

1472 Böttner, C., Berndt, C., Reinardy, B.T.I., Geersen, J., Karstens, J., Bull, J.M., Callow, B.J., Lichtschlag, A., Schmidt,
1473   M., Elger, J., Schramm, B. & Haeckel, M. (2019). Pockmarks in the Witch Ground Basin, Central North Sea,
1474   Geochemistry, Geophysics, Geosystems, 20, 1698-1719. https://doi.org/10.1029/2018gc008068.

Böttner, C., Callow, B.J., Schramm, B., Gross, F., Geersen, J., Schmidt, M., Vasilev, A., Petsinski, P., & Berndt, C., (2020, IN REVIEW). Focused methane migration formed pipe structures in permeable sandstones: Insights from UAV-based digital outcrop analysis in Varna, Bulgaria.

Bouchaala, F., Ali, M.Y., Matsushima, J., Bouzide, Y., Takam Takougang, E.M, Mohamed, A., & Sultan, A. (2019). Azimuthal investigation of compressional seismic-wave attenuation in a fractured reservoir. Geophysics, 84, B437-B446. https://doi.org/10.1190/geo2019-0079.1.

Boudreau, B.P., Algar, C., Johnson, B.D., Croudace, I., Reed, A., Furukawa, Y., Dorgan, K.M., Jumars, P.A., Grader, A.S., & Gardiner, B.S. (2005). Bubble growth and rise in soft sediments. Geology 33, 517-520. https://doi.org/10.1130/G21259.1.

Bouma, A. H., & Boerma, J. A. K. (1968). Vertical disturbances in piston cores. Marine Geology, 6(3), 231-241. https://doi.org/10.1016/0025-3227(68)90032-7.

Brossier, R., Operto, S., & Virieux, J. (2015). Velocity model building from seismic reflection data by full-waveform inversion. Geophysical Prospecting, 63(2), 354-367. https://doi.org/10.1111/1365-2478.12190.

Bull, J. M. (2017). Cruise report – RRS James Cook JC152: CHIMNEY - Characterisation of major overburden pathways above sub-seafloor CO_2 storage reservoirs in the North Sea. Scanner and Challenger pockmark complexes. https://eprints.soton.ac.uk/420257/.

Bull, J.M, Berndt, C.B., Minshull, T.M., Henstock, T., Bayrakci, G., Gehrmann, R., Provenzano, G. Bottner, C., Schramm, B, Callow, B., Chapman, M., Birinci, H., Yilo, N., Dewar, M., Chen, B., Saleem, U., Marin-Moreno, H., Lichtschlag, A., Falcon-Suarez, I., Roche, B., James, R. H., Connelly, D. P., Matter, J., Elger, J., Karstens, J. and Best, A. I. (2018). Constraining Leakage Pathways Through the Overburden Above Sub-Seafloor CO_2 Storage Reservoirs. 14th Greenhouse Gas Control Technologies Conference Melbourne 21-26 October 2018 (GHGT-14).

Bünz, S., Mienert, J., & Berndt, C. (2003). Geological controls on the Storegga gas-hydrate system of the mid-Norwegian continental margin. Earth and Planetary Science Letters, 209(3-4), 291-307. https://doi.org/10.1016/S0012-821X(03)00097-9.

Bünz, S., Polyanov, S., Vadakkepuliyambatta, S., Consolaro, C., & Mienert, J. (2012). Active gas venting through hydrate-bearing sediments on the Vestnesa Ridge, offshore W-Svalbard. Marine Geology, 332, 189-197. https://doi.org/10.1016/j.margeo.2012.09.012.

Cartwright, J. (2007). The impact of 3D seismic data on the understanding of compaction, fluid flow and diagenesis in sedimentary basins. Journal of the Geological Society, 164(5), 881-893. https://doi.org/10.1144/0016-76492006-143.

Cartwright, J., & Huuse, M. (2005). 3D seismic technology: the geological 'Hubble'. Basin Research, 17(1), 1-20. https://doi.org/10.1111/j.1365-2117.2005.00252.x

Cartwright, J., Huuse, M. & Aplin, A. (2007). Seal bypass systems, AAPG bulletin, 91, 1141-1166. https://doi.org/10.1306/04090705181.

Cartwright, J., & C. Santamarina (2015). Seismic characteristics of fluid escape pipes in sedimentary basins: Implications for pipe genesis, Marine and Petroleum Geology, 65, 126-140. https://doi.org/10.1016/j.marpetgeo.2015.03.023.

Cathles, L. M., Z. Su, & D. Chen (2010). The physics of gas chimney and pockmark formation, with implications for assessment of seafloor hazards and gas sequestration, Marine and Petroleum Geology, 27(1), 82-91. https://doi.org/10.1016/j.marpetgeo.2009.09.010.

Cevatoglu, M., Bull, J.M., Vardy, M.E., Gernon, T.M., Wright, I.C. & Long, D. (2015). Gas migration pathways, controlling mechanisms and changes in sediment acoustic properties observed in a controlled sub-seabed CO_2 release experiment, International Journal of Greenhouse Gas Control. 38, 26-43, https://doi.org/10.1016/j.ijggc.2015.03.005.

Chadwick, R. A., Arts, R., Eiken, O., Kirby, G. A., Lindeberg, E., & Zweigel, P. (2004). 4D Seismic Imaging of an Injected C02 Plume at the Sleipner Field, Central North Sea. Geological Society, London, Memoirs, 29(1), 311-320. https://doi.org/10.1144/GSL.MEM.2004.029.01.29.

Chadwick, R. A., Williams, G. A., & Falcon-Suarez, I. (2019). Forensic mapping of seismic velocity heterogeneity in a CO2 layer at the Sleipner CO2 storage operation, North Sea, using time-lapse seismics, International Journal of Greenhouse Gas Control, 90, 102793. https://doi.org/10.1016/j.ijggc.2019.102793.

Chapman, M. (2003). Frequency-dependent anisotropy due to meso-scale fractures in the presence of equant porosity. Geophysical prospecting, 51(5), 369-379. https://doi.org/10.1046/j.1365-2478.2003.00384.x.

Chapman, M. (2009). Modeling the effect of multiple sets of mesoscale fractures in porous rock on frequency-dependent anisotropy. Geophysics, 74(6), D97-D103. https://doi.org/10.1190/1.3204779.

Cheeseman, S.J., Edwards, R.N., & Chave, A.D. (1987). On the Theory of Sea Floor Conductivity Mapping using Transient Electromagnetic Systems. Geophysics, 52:204-217. https://doi.org/10.1190/1.1442296.

Clay, S., & Vardy, M. (2018). Optimisation of Source and Receiver Geometry for Ultra High Frequency Seismic Data. In 3rd Applied Shallow Marine Geophysics Conference (Vol. 2018, No. 1, pp. 1-5). European Association of Geoscientists & Engineers. https://doi.org/10.3997/2214-4609.201802673.

Clayton, C.J. & Dando, P.R. (1996). Comparison of seepage and seal leakage rates. In D. Schumacher & M. A. Abrams (Eds.), Hydrocarbon Migration and Its Near-surface Expression. in Outgrowth of the AAPG Hedberg Research Conference. American Association of Petroleum Geologists Memoir, Vancouver, British Columbia, April 24-28, 1994 (No. 66). AAPG.

Cole, D., Stewart, S.A. & Cartwright, J.A. (2000). Giant irregular pockmark craters in the Palaeogene of the Outer Moray Firth Basin, UK North Sea, Marine and Petroleum Geology, 17, 563-577. https://doi.org/10.1016/S0264-8172(00)00013-1.

Constable, S. (2010). Ten years of marine CSEM for hydrocarbon exploration. Geophysics, 75(5), 75A67-75A81. https://doi.org/10.1190/1.3483451.

Constable, S. (2013). Review paper: Instrumentation for marine magnetotelluric and controlled source electromagnetic sounding. Geophysical Prospecting, 61(s1), 505-532. https://doi.org/10.1111/j.1365-2478.2012.01117.x.

Constable, S. C., Parker, R. L., & Constable, C. G. (1987). Occam's inversion: A practical algorithm for generating smooth models from electromagnetic sounding data. Geophysics, 52(3), 289-300. https://doi.org/10.1190/1.1442303.

Constable, S., Kannberg, P. K., & Weitemeyer, K. (2016). Vulcan: A deep-towed CSEM receiver. Geochemistry, Geophysics, Geosystems, 17(3), 1042-1064. https://doi.org/10.1002/2015GC006174.

Crain, E. R. (2010), Crain's petrophysical handbook, Spectrum 2000 Mindware, Rocky Mountain House, AB. https://www.spec2000.net, 2019.

Crampin, S. (1985). Evaluation of anisotropy by shear-wave splitting. Geophysics, 50(1), 142-152. https://doi.org/10.1190/1.1441824.

Davy, R.G., Morgan, J.V., Minshull, T.A., Bayrakci, G., Bull, J.M., Klaeschen, D., Reston, T.J., Sawyer, D.S., Lymer, G. & Cresswell, D. (2018). Resolving the fine-scale velocity structure of continental hyperextension at the Deep Galicia Margin using full-waveform inversion. Geophysical Journal International, 212(1), pp.244-263. https://doi.org/10.1093/gji/ggx415.

De Boever, E., Swennen, R., & Dimitrov, L. (2006a). Lower Eocene carbonate cemented chimneys (Varna, NE Bulgaria): Formation mechanisms and the (a) biological mediation of chimney growth?. Sedimentary Geology, 185(3-4), 159-173. http://dx.doi.org/10.1016/j.sedgeo.2005.12.010.

De Boever, E., Swennen, R., & Dimitrov, L. (2006b). Lower Eocene carbonate-cemented "chimney" structures (Varna, Bulgaria)—control of seepage rates on their formation and stable isotopic signature. Journal of Geochemical Exploration, 89(1-3), 78-82. https://doi.org/10.1016/j.gexplo.2005.11.028

Dean, M., & Tucker, O. (2017). A risk-based framework for Measurement, Monitoring and Verification (MMV) of the Goldeneye storage complex for the Peterhead CCS project, UK, International Journal of Greenhouse Gas Control, 61, 1-15. https://doi.org/10.1016/j.ijggc.2017.03.014.

Dean, M., Tucker, O.D., Strijbos, F.P.L., de Jong, R.A.M., Marshall, J. & Goswami, R., (2015). Characterisation and Monitoring of the Goldeneye CO_2 Storage Site. in 77th EAGE Conference and Exhibition 2015. https://doi.org/10.3997/2214-4609.201412719.

Deusner, C., Gupta, S., Kossel, E., Freise, M., Anbergen, H., Wille, T., Bigalke, N., Haeckel, M. (2016). The role of high-pressure flow-through experiments for evaluating the mechanical behaviour of gas hydrate-bearing soils. Energy Geotechnics, 437-443. https://doi.org/10.1201/b21938-70.

Dickens, G., M. Koelling, D. Smith, L. Schnieders, & IODP Exp. 302 Scientists (2007). Rhizon sampling of pore waters on scientific drilling expeditions: an example from the IODP Expedition 302, Arctic Coring Expedition (ACEX). IODP Scientific Drilling, 4, 22-25. https://doi.org/10.2204/iodp.sd.4.08.2007.

Domenico, S. N. (1977). Elastic properties of unconsolidated porous sand reservoirs. Geophysics, 42(7), 1339-1368. https://doi.org/10.1190/1.1440797.

Dunn, R. A., & Toomey, D. R. (2001). Crack-induced seismic anisotropy in the oceanic crust across the East Pacific Rise (9 30′ N). Earth and Planetary Science Letters, 189(1-2), 9-17. https://doi.org/10.1016/S0012-821X(01)00353-3.

Dunn, R. A., Lekić, V., Detrick, R. S., & Toomey, D. R. (2005). Three-dimensional seismic structure of the Mid-Atlantic Ridge (35 N): Evidence for focused melt supply and lower crustal dike injection. Journal of Geophysical Research: Solid Earth, 110(B9). https://doi.org/10.1029/2004JB003473.

Edwards, R. N. (1988). Two-dimensional modeling of a towed in-line electric dipole-dipole seafloor electromagnetic system: The optimum time delay or frequency for target resolution. Geophysics, 53(6):846-853. https://doi.org/10.1190/1.1442519.

Edwards, R. N. (1997). On the resource evaluation of marine gas hydrate deposits using sea-floor transient electric dipole-dipole methods. Geophysics, 62(1), 63-74. https://doi.org/10.1190/1.1444146.

Edwards, R. N. (2005). Marine Controlled Source Electromagnetics: Principles, methodologies, future commercial applications. In Surveys in Geophysics, 26, 675-700. Springer, Berlin, Heidelberg, New York. https://doi.org/10.1007/s10712-005-1830-3.

Eiken, O. (2019). Twenty years of Monitoring CO_2 injection at Sleipner. In: Davis, T.L., Landrø, M., Wilson, M. (Eds.), Geophysics and Geosequestration. Cambridge University Press, 209-234. https://doi.org/10.1017/9781316480724.014.

Ellingsrud, S., Eidesmo, T., Johansen, S., Sinha, M. C., MacGregor, L. M., & Constable, S. (2002). Remote sensing of hydrocarbon layers by seabed logging (SBL): Results from a cruise offshore Angola. The Leading Edge, 21(10), 972-982. https://doi.org/10.1190/1.1518433.

EU CCS Directive on Geological Storage of Carbon Dioxide (2009). DIRECTIVE 2009/31/EC OF THE EUROPEAN PARLIAMENT AND OF THE COUNCIL, Official Journal of the European Union, L 140/114 EN. https://eur-lex.europa.eu/LexUriServ/LexUriServ.do?uri=OJ:L:2009:140:0114:0135:EN:PDF.

Falcon-Suarez, I., North, L., Amalokwu, K. & Best, A. (2016). Integrated geophysical and hydromechanical assessment for CO_2 storage: shallow low permeable reservoir sandstones, Geophysical Prospecting, 64, 828-847. https://doi.org/10.1111/1365-2478.12396.

Falcon-Suarez, I., Marín-Moreno, H., Browning, F., Lichtschlag, A., Robert, K., North, L.J. & Best, A.I. (2017). Experimental assessment of pore fluid distribution and geomechanical changes in saline sandstone reservoirs during and after CO_2 injection, International Journal of Greenhouse Gas Control, 63, 356-369. https://doi.org/10.1016/j.ijggc.2017.06.019.

Falcon-Suarez, I., Papageorgiou, G., Chadwick, A., North, L., Best, A. & Chapman, M. (2018). CO2-brine flow-through on an Utsira Sand core sample: Experimental and modelling. Implications for the Sleipner storage field, International Journal of Greenhouse Gas Control, 68, 236-246. https://doi.org/10.1016/j.ijggc.2017.11.019.

Fauria, K. E., & A. W. Rempel (2011), Gas invasion into water-saturated, unconsolidated porous media: Implications for gas hydrate reservoirs, Earth and Planetary Science Letters, 312(1-2), 188-193, https://doi.org/10.1016/j.epsl.2011.09.042.

Flohr & Schapp et al. (in review, this volume). Towards improved monitoring of offshore carbon storage: A real-world field experiment detecting a controlled sub-seafloor CO_2 release

Frey, S. E., Gingras, M. K., & Dashtgard, S. E. (2009). Experimental studies of gas-escape and water-escape structures: mechanisms and morphologies. Journal of Sedimentary Research, 79(11), 808-816. http://dx.doi.org/10.2110/jsr.2009.087.

Furre, A.-K., Menegulo, R., Ringrose, P. and Kassold, S. (2019a) Building confidence in CCS: From Sleipner to the Northern Lights Project, First Break 37 (7), 81-87. https://doi.org/10.3997/1365-2397.n0038.

Furre, A., Ringrose, P., & Santi, A.C. (2019b). Observing the Invisible – CO_2 Feeder Chimneys on Seismic Time-Lapse Data. 81st EAGE Conference and Exhibition 2019, Volume 2019, p.1 – 5. https://doi.org/10.3997/2214-4609.201901646.

Gafeira, J. & Long, D. 2015. Geological investigation of pockmarks in the Scanner Pockmark SCI area. JNCC Report No 570. JNCC Peterborough. http://data.jncc.gov.uk/data/290b95b7-fcfc-4c76-8780-8714329dcf0c/JNCC-Report-570-FINAL-WEB.pdf.

Gay, A., Lopez, M., Berndt, C. & Séranne, M. (2007). Geological controls on focused fluid flow associated with seafloor seeps in the Lower Congo Basin, Marine Geology, 244, 68-92. https://doi.org/10.1016/j.margeo.2007.06.003.

1632 GEBCO (2019). The GEBCO_2019 Grid - a continuous terrain model of the global oceans and land. British
1633   Oceanographic Data Centre, National Oceanography Centre, NERC, UK. https://doi.org/10/c33m.

1634 Gehrmann, R.A.S., North, L.J., Graber, S., Szitkar, F., Petersen, S., Minshull, T.A. & Murton, B.J. (2019). Marine
1635   mineral exploration with controlled-source electromagnetics at the TAG hydrothermal field, 26N Mid-Atlantic
1636   Ridge, Geophysical Research Letters, 46, 11, 5808–5816. https://doi.org/10.1029/2019GL082928.

1637 Gehrmann, R. A. S., Provenzano, G., Böttner, C., Marin-Moreno, H., Bayrakci, G., Tan, Y. Y., Yilo, N. K., Djanni,
1638   A. T., Weitemeyer, K. A., Minshull, T. A., Bull, J. M., Karstens, J., & Berndt, C. (In review), Porosity and free
1639   gas estimates from controlled source electromagnetic data at the Scanner Pockmark in the North Sea,
1640   International Journal of Greenhouse Gas Control

1641 Global CCS Institute (2019), The Global Status of CCS: 2019, Melbourne, Australia.
1642   https://www.globalccsinstitute.com/wp
1643   content/uploads/2019/12/GCC_GLOBAL_STATUS_REPORT_2019.pdf.

1644 Górszczyk, A., Operto, S., & Malinowski, M. (2017). Toward a robust workflow for deep crustal imaging by FWI
1645   of OBS data: The eastern Nankai Trough revisited. Journal of Geophysical Research: Solid Earth, 122(6), 4601-
1646   4630. https://doi.org/10.1002/2016JB013891.

1647 Goswami, B. K., Weitemeyer, K. A., Minshull, T. A., Sinha, M. C., Westbrook, G. K., Chabert, A., Henstock, T. &
1648   Ker, S. (2015). A joint electromagnetic and seismic study of an active pockmark within the hydrate stability
1649   field at the Vestnesa Ridge, West Svalbard margin. Journal of Geophysical Research: Solid Earth, 120(10),
1650   6797-6822. https://doi.org/10.1002/2015JB012344.

1651 Graber, K. K., Pollard, E., Jonasson, B., & Schulte, E. (2002), Overview of Ocean Drilling Program Engineering
1652   Tools and Hardware. https://doi.org/10.2973/odp.tn.31.2002.

1653 Haacke, R. R., & Westbrook, G. K. (2006). A fast, robust method for detecting and characterizing azimuthal
1654   anisotropy with marine PS converted waves, and its application to the west Svalbard continental slope.
1655   Geophysical Journal International, 167(3), 1402–1412. https://doi.org/10.1111/j.1365-246X.2006.03186.x.

1656 Haacke, R. R., Westbrook, G. K., & Peacock, S. (2009). Layer stripping of shear-wave splitting in marine PS
1657   waves. Geophysical Journal International, 176(3), 782-804. https://doi.org/10.1111/j.1365-246X.2008.04060.x.

1658 Harrington, R. M., & Brodsky, E. E. (2007). Volcanic hybrid earthquakes that are brittle-failure events. Geophysical
1659   Research Letters, 34(6). https://doi.org/10.1029/2006GL028714.

1660 Harris, P. E., Du, Z., MacGregor, L., Olsen, W., Shu, R., & Cooper, R. (2009). Joint interpretation of seismic and
1661   CSEM data using well log constraints: An example from the Luva Field. First Break, 27(5).
1662   https://doi.org/0.3997/1365-2397.27.1299.28932.

1663 Hindle, A. D. (1997). Petroleum Migration Pathways and Charge Concentration: A Three-Dimensional
1664   Model. AAPG Bulletin; 81 (9): 1451–1481. https://doi.org/10.1306/3B05BB1E-172A-11D7-
1665   8645000102C1865D.

1666 Hoversten, G.M., Cassassuce, G. , Gasperikova, E., Newman, G.A., Chen, J., Rubein, Y., Hou, Z., & Vasco, D.
1667   (2006). Direct reservoir parameter estimation using joint inversion of marine seismic AVA and CSEM data.
1668   Geophysics, 71(3):C1-C13. https://doi.org/10.1190/1.2194510.

1669 Hovland, M., & Sommerville, J. H. (1985). Characteristics of two natural gas seepages in the North Sea. Marine and
1670   Petroleum Geology, 2(4), 319-326. https://doi.org/10.1016/0264-8172(85)90027-3

1671 Hovland, M., Heggland, R., De Vries, M.H. & Tjelta, T.I. (2010). Unit-pockmarks and their potential significance
1672   for predicting fluid flow, Marine and Petroleum Geology, 27, 1190-1199.
1673   https://doi.org/10.1016/j.marpetgeo.2010.02.005.

1674 Hudson, J. A. (1981). Wave speeds and attenuation of elastic waves in material containing cracks. Geophysical
1675   Journal International, 64(1), 133-150. https://doi.org/10.1111/j.1365-246X.1981.tb02662.x.

1676 Hurst, A., Scott, A., & Vigorito, M. (2011). Physical characteristics of sand injectites. Earth-Science Reviews, 106(3-
1677   4), 215-246. https://doi.org/10.1016/j.earscirev.2011.02.004.

1678 Hustoft, S., Bünz, S., & Mienert, J. (2010). Three-dimensional seismic analysis of the morphology and spatial
1679   distribution of chimneys beneath the Nyegga pockmark field, offshore mid-Norway. Basin Research, 22(4),
1680   465-480. https://doi.org/10.1111/j.1365-2117.2010.00486.x.

1681 Huuse, M., Shoulders, S. J., Netoff, D. I., & Cartwright, J. (2005). Giant sandstone pipes record basin-scale
1682   liquefaction of buried dune sands in the Middle Jurassic of SE Utah. Terra Nova, 17(1), 80-85.
1683   https://doi.org/10.1111/j.1365-3121.2004.00587.x.

1684 Huuse, M., Jackson, C. A. L., Van Rensbergen, P., Davies, R. J., Flemings, P. B., & Dixon, R. J. (2010). Subsurface
1685   sediment remobilization and fluid flow in sedimentary basins: an overview. Basin Research, 22(4), 342-360.
1686   https://doi.org/10.1111/j.1365-2117.2010.00488.x.

1687 IPCC (2005). Carbon Dioxide Capture and Storage. Cambridge University Press, Cambridge, England.
1688   https://www.ipcc.ch/report/carbon-dioxide-capture-and-storage/.

1689 IPCC (2014). Climate Change 2014: Synthesis Report. Contribution of Working Groups I, II and III to the Fifth
1690   Assessment Report of the Intergovernmental Panel on Climate Change [Core Writing Team, R.K. Pachauri and
1691   L.A.   Meyer   (eds.)].   IPCC,   Geneva,   Switzerland,   151   pp.
1692   https://epic.awi.de/id/eprint/37530/1/IPCC_AR5_SYR_Final.pdf.

1693 Jakobsen, M., & Chapman, M. (2009). Unified theory of global flow and squirt flow in cracked porous media.
1694   Geophysics, 74(2), WA65-WA76. https://doi.org/10.1190/1.3078404.

1695 Jannane, M., Beydoun, W., Crase, E., Cao, D., Koren, Z., Landa, E., Mendes, M., Pica, A., Noble, M., Rotes, G.,
1696   Singh, S., Snieder, R., Tarantola, A., Trezeguet, D., and Xie, M. (1989). Wavelengths of earth structures that
1697   can be resolved from seismic reflection data. Geophysics, 54(7), 906-910. https://doi.org/10.1190/1.1442719.

1698 Jin, Z., Chapman, M. & Papageorgiou, G (2018). Frequency-dependent anisotropy in a partially saturated fractured
1699   rock, Geophysical Journal International, 215(3), 1985-1998. https://doi.org/10.1093/gji/ggy399.

1700 Judd, A. & Hovland, M. (2009). Seabed fluid flow: the impact on geology, biology and the marine environment.
1701   Cambridge University Press. https://doi.org/10.1017/CBO9780511535918.

1702 Judd, A., Long, D. & Sankey, M. (1994). Pockmark formation and activity, UK block 15/25, North Sea, Bulletin of
1703   the Geological Society of Denmark, 41, 34-49.

1704 Karstens, J., Böttner, C., Edwards, M., Falcon-Suarez, I., Flohr, A., James, R., Lichtschlag, A., Maicher, D., Pheasant,
1705   I., Roche, B., Schramm, B., & Wilson, M. (2019). RV MARIA S. MERIAN Cruise Report MSM78-PERMO2,
1706   Edinburgh–Edinburgh (UK), 16.10.-25.10.2018. https://doi.org/10.3289/geomar_rep_ns_48_2019.

1707 Karstens, J. & Berndt, C. (2015). Seismic chimneys in the Southern Viking Graben – Implications for palaeo fluid
1708   migration   and   overpressure   evolution,   Earth   and   Planetary   Science   Letters,   412,   88-100.
1709   http://dx.doi.org/10.1016/j.epsl.2014.12.017.

1710 Lacoss, R, Kelly, E. & Toksöz, M. (1969). Estimation of Seismic Noise Structure using Arrays. Geophysics. 34. 21-
1711   38. https://doi.org/10.1190/1.1439995.

1712 Landrø, M., Solheim, O. A., Hilde, E., Ekren, B. O., & Stronen, L. K. (1999). The Gullfaks 4D seismic study.
1713   Petroleum Geoscience, 5(3), 213-226. https://doi.org/10.1144/petgeo.5.3.213.

1714 Latter, J. H. (1981). Volcanic earthquakes, and their relationship to eruptions at Ruapehu and Ngauruhoe volcanoes.
1715   Journal of volcanology and geothermal research, 9(4), 293-309. https://doi.org/10.1016/0377-0273(81)90041-
1716   X.

1717 Lee, M. W. (2004). Elastic velocities of partially gas-saturated unconsolidated sediments: Marine and Petroleum
1718   Geology, 21, no. 6, 641–650. https://doi.org/10.1016/j.marpetgeo.2003.12.004.

1719 Li, X. Y. (1997). Fractured reservoir delineation using multicomponent seismic data. Geophysical Prospecting, 45(1),
1720   39-64. https://doi.org/10.1046/j.1365-2478.1997.3200262.x.

1721   Li, J., Roche, B., Bull, J.M., White, P.R., Leighton, T.G., Provenzano, G. Dewar, M., & Henstock, T. (2020).
1722   Broadband acoustic inversion for gas flux quantication - application to a methane plume at Scanner Pockmark,
1723   central North Sea. Journal of Geophysical Research, Oceans, 125(9), https://doi.org/10.1029/2020JC016360
1724 Lin, L., Hsu, H., Liu, C. et al. Marine 3D seismic volumes from 2D seismic survey with large streamer feathering.
1725   (2019). Mar Geophys Res 40, 619–633. https://doi.org/10.1007/s11001-019-09391-9.

1726 Linke, P. & Haeckel, M. (2018). RV POSEIDON Cruise Report POS518: Baseline Study for the Environmental
1727   Monitoring of Subseafloor CO2 Storage Operations, Leg 2: Bremerhaven – Kiel (Germany) 12.10.-28.10.2017.
1728   https://doi.org/10.3289/GEOMAR_REP_NS_40_2018.

1729 Liu, E., Hudson, J. A., & Pointer, T. (2000). Equivalent medium representation of fractured rock. Journal of
1730   Geophysical Research: Solid Earth, 105(B2), 2981-3000. https://doi.org/10.1029/1999JB900306.

1731 Liu J., Haeckel M., Rutqvist J., Wang S., Yan W. (2019) The mechanism of methane gas migration through the gas
1732   hydrate stability zone: insights from numerical simulations. Journal of Geophysical Research 124, 4399-4427.
1733   https://doi.org/10.1029/2019JB017417.

1734 Løseth, H., Gading, M., & Wensaas, L. (2009). Hydrocarbon leakage interpreted on seismic data. Marine and
1735   Petroleum Geology, 26(7), 1304-1319. http://dx.doi.org/10.1016/j.marpetgeo.2008.09.008.

1736 Løseth, H., Wensaas, L., Arntsen, B., Hanken, N.-M., Basire, C. & Graue, K. (2011). 1000 m long gas blow-out
1737   pipes, Marine and Petroleum Geology, 28, 1047-1060. https://doi.org/10.1016/j.marpetgeo.2010.10.001.

1738 Lowe, D. R. (1975). Water escape structures in coarse-grained sediments, Sedimentology, 22(2), 157-204.
1739   https://doi.org/10.1111/j.1365-3091.1975.tb00290.x.

1740 Lumley, D. (2010). 4D seismic monitoring of CO2 sequestration. The Leading Edge, 29(2), 150-155.
1741   https://doi.org/10.1190/1.3304817.

1742 Marin-Moreno, H., Bull J. M., Matter J., Sanderson, D. J., Roche, B. (2019). Reactive transport modeling insights
1743   into CO2 migration through sub-vertical fluid flow structures, International Journal of Greenhouse Gas Control,
1744   86, 82-92. https://doi.org/10.1016/j.ijggc.2019.04.018.

1745 Maultzsch, S., Chapman, M., Liu, E., & Li, X. Y. (2003). Modelling frequency-dependent seismic anisotropy in
1746   fluid-saturated rock with aligned fractures: implication of fracture size estimation from anisotropic
1747   measurements. Geophysical Prospecting, 51(5), 381-392. https://doi.org/10.1046/j.1365-2478.2003.00386.x.

1748 Maultzsch, S., Chapman, M., Liu, E., & Li, X. Y. (2007). Modelling and analysis of attenuation anisotropy in multi-
1749   azimuth VSP data from the Clair field. Geophysical prospecting, 55(5), 627-642. https://doi.org/10.1111/j.1365-
1750   2478.2007.00645.x.

1751 McDermott, C., & Kolditz, O., (2006), Geomechanical model for fracture deformation under hydraulic, mechanical
1752   and thermal loads, Hydrogeology Journal, 14(4), 485-498, https://doi.org/10.1007/s10040-005-0455-4.

1753 Minnaert, M. (1933). XVI. On musical air-bubbles and the sounds of running water. The London, Edinburgh, and
1754   Dublin Philosophical Magazine and Journal of Science, 16(104), 235-248.
1755   https://doi.org/10.1080/14786443309462277.

1756 Minshull, T.A., Sinha, M.C. & Peirce, C. (2005). Multi-disciplinary, sub-seabed geophysical imaging – a new pool
1757   of 28 seafloor instruments in use by the United Kingdom Ocean Bottom Instrument Consortium. Sea
1758   Technology, 46(10), 27-31. http://eprints.soton.ac.uk/id/eprint/18172.

1759 Morgan, J., Warner, M., Bell, R., Ashley, J., Barnes, D., Little, R., Roele, K. & Jones, C. (2013). Next-generation
1760   seismic experiments: wide-angle, multi-azimuth, three-dimensional, full-waveform inversion. Geophysical
1761   Journal International, 195(3), 1657-1678. https://doi.org/10.1093/gji/ggt345.

1762 Moss, J. L., & Cartwright, J. (2010a). 3D seismic expression of km-scale fluid escape pipes from offshore Namibia.
1763   Basin Research, 22(4), 481-501. https://doi.org/10.1111/j.1365-2117.2010.00461.x.

1764 Moss, J. L., & Cartwright, J. (2010b). The spatial and temporal distribution of pipe formation, offshore Namibia.
1765   Marine and Petroleum Geology, 27(6), 1216-1234. https://doi.org/10.1016/j.marpetgeo.2009.12.013.

1766 Mueller, M. C. (1992). Using shear waves to predict lateral variability in vertical fracture intensity. The Leading
1767   Edge, 11(2), 29-35. https://doi.org/10.1190/1.1436870.

1768 Muñoz-Ibáñez, A., Falcon-Suarez, I.H., Marín-Moreno, H., Martín, J.D. & Mackin, P. (2019). Transport properties
1769   of saline CO2 storage reservoirs with unconnected fractures from brine-CO2 flow-through tests, Journal of
1770   Petroleum Science and Engineering, 106551, https://doi.org/10.1016/j.petrol.2019.106551.

1771 Myer, D., Constable, S., & Key, K. (2011). Broad-band waveforms and robust processing for marine CSEM surveys.
1772   Geophysical Journal International, 184(2), 689-698. https://doi.org/10.1111/j.1365-246X.2010.04887.x.

1773 Naif, S., Key, K., Constable, S. & Evans, R.L. (2015). Water-rich bending faults at the middle america trench.
1774   Geochemistry, Geophysics, Geosystems, 16(8), 2582-2597. https://doi.org/10.1002/2015GC005927.

1775 Nichols, R. J., Sparks, R. S. J. & Wilson, C. J. N. (1994). Experimental studies of the fluidization of layered sediments
1776   and the formation of fluid escape structures. Sedimentology, 41(2), 233-253. https://doi.org/10.1111/j.1365-
1777   3091.1994.tb01403.x.

1778 Ostrander, W. (1984). Plane-wave reflection coefficients for gas sands at nonnormal angles of incidence. Geophysics,
1779   49(10), 1637-1648. https://doi.org/10.1190/1.1441571.

1780 Ottesen, D., Dowdeswell, J. A., & Bugge, T. (2014). Morphology, sedimentary infill and depositional environments
1781   of the Early Quaterny North Sea Basin (56–62 N). Marine and Petroleum Geology, 56, 123-146.
1782   https://doi.org/10.1016/j.marpetgeo.2014.04.007.

1783 Palacky, G.V. (1988). Resistivity characteristics of geologic targets. In Misac N. Nabighian, editor, Electromagnetic
1784   Methods in Applied Geophysics, volume 1, chapter 3, 52-129. Society of Exploration Geophysicists.
1785   https://doi.org/10.1190/1.9781560802631.ch3.

1786 Panieri, G., Bünz, S., Fornari, D. J., Escartin, J., Serov, P., Jansson, P., Torres, M.E., Johnson, J.E., Hong, W., Sauer,
1787   S. and Garcia, R (2017). An integrated view of the methane system in the pockmarks at Vestnesa Ridge, 79 N.
1788   Marine Geology, 390, 282-300. https://doi.org/10.1016/j.margeo.2017.06.006.

1789 Pape, T., Hohnberg, H.-J., Wunsch, D., Anders, E., Freudenthal, T., Huhn, K. & G. Bohrmann (2017), Design and
1790   deployment of autoclave pressure vessels for the portable deep-sea drill rig MeBo (Meeresboden-Bohrgerät),
1791   Scientific Drilling, 23, 29-37, https://doi.org/10.5194/sd-23-29-2017.

1792 Petersen, C. J., Bünz, S., Hustoft, S., Mienert, J., & Klaeschen, D. (2010). High-resolution P-Cable 3D seismic
1793   imaging of gas chimney structures in gas hydrated sediments of an Arctic sediment drift. Marine and Petroleum
1794   Geology, 27(9), 1981-1994. https://doi.org/10.1016/j.marpetgeo.2010.06.006.

1795 Picozzi, M., Parolai, S., & Bindi, D. (2010). Deblurring of frequency–wavenumber images from small-scale seismic
1796   arrays. Geophysical Journal International, 181(1), 357-368. https://doi.org/10.1111/j.1365-246X.2009.04471.x.

1797 Planke, S., Eriksen, F. N., Berndt, C., Mienert, J., & Masson, D. G. (2009). P-Cable high-resolution seismic.
1798   Oceanography, 22(1), 85. https://doi.org/10.5670/oceanog.2009.09.

1799 Plaza-Faverola, A., Bünz, S., & Mienert, J. (2010). Fluid distributions inferred from P-wave velocity and reflection
1800   seismic amplitude anomalies beneath the Nyegga pockmark field of the mid-Norwegian margin. Marine and
1801   Petroleum Geology, 27(1), 46-60. https://doi.org/10.1016/j.marpetgeo.2009.07.007.

1802 Plaza-Faverola, A., Bünz, S., & Mienert, J. (2011). Repeated fluid expulsion through sub-seabed chimneys offshore
1803   Norway in response to glacial cycles. Earth and Planetary Science Letters, 305(3-4), 297-308.
1804   https://doi.org/10.1016/j.epsl.2011.03.001.

1805 Plaza-Faverola, A., Bünz, S., Johnson, J. E., Chand, S., Knies, J., Mienert, J., & Franek, P. (2015). Role of tectonic
1806   stress in seepage evolution along the gas hydrate-charged Vestnesa Ridge, Fram Strait. Geophysical Research
1807   Letters, 42(3), 733-742. https://doi.org/10.1002/2014GL062474.

1808 Plaza-Faverola, A., Vadakkepuliyambatta, S., Hong, W.L., Mienert, J., Bünz, S., Chand, S. & Greinert, J., (2017).
1809   Bottom-simulating reflector dynamics at Arctic thermogenic gas provinces: An example from Vestnesa Ridge,
1810   offshore west Svalbard, Journal of Geophysical Research: Solid Earth, 122, 4089-4105.
1811   https://doi.org/10.1002/2016jb013761.

1812 Prieux, V., Brossier, R., Operto, S., & Virieux, J. (2013). Multiparameter full waveform inversion of multicomponent
1813   ocean-bottom-cable data from the Valhall field. Part 1: Imaging compressional wave speed, density and
1814   attenuation. Geophysical Journal International, 194(3), 1640-1664. https://doi.org/10.1093/gji/ggt177.

1815 Provenzano, G., Vardy, M. E., & Henstock, T. J. (2018). Decimetric-resolution stochastic inversion of shallow
1816   marine seismic reflection data: dedicated strategy and application to a geohazard case study. Geophysical
1817   Journal International, 214(3), 1683-1700. https://doi.org/10.1093/gji/ggy221.

1818 Räss, L., Simon, N.S.C. & Podladchikov, Y.Y. (2018). Spontaneous formation of fluid escape pipes from subsurface
1819   reservoirs. Scientific Reports, 8, 11116. https://doi.org/10.1038/s41598-018-29485-5.

1820 Reinardy, B. T., Hjelstuen, B. O., Sejrup, H. P., Augedal, H., & Jørstad, A. (2017). Late Pliocene-Pleistocene
1821   environments and glacial history of the northern North Sea. Quaternary Science Reviews, 158, 107–126.
1822   https://doi.org/10.1016/j.quascirev.2016.12.022.

1823 Resnick, J. R. (1990). Stratigraphic filtering. Pure and Applied Geophysics, 132(1-2), 49-65.
1824   https://doi.org/10.1007/BF00874357.

1825 Riboulot, V., Thomas, Y., Berné, S., Jouet, G., & Cattaneo, A. (2014). Control of Quaternary sea-level changes on
1826   gas seeps. Geophysical Research Letters, 41(14), 4970-4977. https://doi.org/10.1002/2014GL060460.

1827 Roberts, J. J., Wilkinson, M., Naylor, M., Shipton, Z. K., Wood, R. A., & Haszeldine, R. S. (2017). Natural CO_2
1828   sites in Italy show the importance of overburden geopressure, fractures and faults for CO_2 storage performance
1829   and risk management. Geological Society, London, Special Publications, 458(1), 181-211.
1830   https://doi.org/10.1144/sp458.14.

1831 Roche, B., Bull, J. M., Marin-Moreno, H., Leighton, T., Falcon-Suarez, I. H., White, P. R., Provenzano, G., Tholen,
1832   M., Lichtschlag, A., Li, J., & Faggetter, M. (in review, this volume) Time-lapse imaging of CO_2 migration within
1833   near-surface sediments during a controlled sub-seabed release experiment.

1834 Ross, J. A., Peakall, J., & Keevil, G. M. (2014). Facies and flow regimes of sandstone-hosted columnar intrusions:
1835   Insights from the pipes of Kodachrome Basin State Park. Sedimentology, 61(6), 1764-1792.
1836   https://doi.org/10.1111/sed.12115.

Rost, S., & Thomas, C. (2009). Improving seismic resolution through array processing techniques. Surveys in Geophysics, 30(4-5), 271-299. https://doi.org/10.1007/s10712-009-9070-6.

Rutqvist, J. (2015), Fractured rock stress-permeability relationships from in situ data and effects of temperature and chemical-mechanical couplings, Geofluids, 15(1-2), 48-66, https://doi.org/10.1111/gfl.12089.

Saleem, U. (2020), Numerical Modeling of Two-Phase flow through porous media into water column. Chapter 6. PhD Thesis, Heriot-Watt University, Edinburgh, UK

Schmidt, M. (2019), RV POSEIDON Cruise Report POS534 STEMM-CCS: Strategies for Environmental Monitoring of Marine Carbon Capture and Storage Leg 1: Kiel (Germany) – Aberdeen (United Kingdom) 01.05. – 22.05.2019 Leg 2: Aberdeen (United Kingdom) – Bremerhaven (Germany) 23.05. – 29.05.2019.

Schneider von Deimling, J. S., Greinert, J., Chapman, N. R., Rabbel, W., & Linke, P. (2010). Acoustic imaging of natural gas seepage in the North Sea: Sensing bubbles controlled by variable currents. Limnology and Oceanography: Methods, 8(5), 155-171. https://doi.org/10.4319/lom.2010.8.155

Seeberg-Elverfeldt J., Schlueter M., Feseker T. & Kolling M. (2005). Rhizon sampling of porewaters near the sediment-water interface of aquatic systems. Limnol. Oceanogr.: Methods 3, 361–371. https://doi.org/10.4319/lom.2005.3.361.

Sirgue, L., Barkved, O. I., Dellinger, J., Etgen, J., Albertin, U., & Kommedal, J. H. (2010). Thematic set: Full waveform inversion: The next leap forward in imaging at Valhall. First Break, 28(4), 65-70. https://doi.org/10.3997/1365-2397.2010012

Shapiro, S. A., & Hubral, P. (1995). Frequency-dependent shear-wave splitting and velocity anisotropy due to elastic multilayering. Journal of Seismic Exploration, 4, 151-168. https://doi.org/10.1190/1.1444567.

Sinha, M. C., Patel, P. D., Unsworth, M. J., Owen, T. R. E., & MacCormack, M. R. G. (1990). An active source electromagnetic sounding system for marine use. Marine Geophysical Researches, 12(1-2), 59-68. https://doi.org/10.1007/BF00310563.

Smith, A. J., Mienert, J., Bünz, S., & Greinert, J. (2014). Thermogenic methane injection via bubble transport into the upper Arctic Ocean from the hydrate-charged Vestnesa Ridge, Svalbard. Geochemistry, Geophysics, Geosystems, 15(5), 1945-1959. https://doi.org/10.1002/2013GC005179.

Smithyman, B., Pratt, R. G., Hayles, J., & Wittebolle, R. (2009). Detecting near-surface objects with seismic waveform tomography. Geophysics, 74(6), WCC119-WCC127. https://doi.org/10.1190/1.3223313.

Stewart, M. A., & Lonergan, L. (2011). Seven glacial cycles in the middle-late Pleistocene of northwest Europe: Geomorphic evidence from buried tunnel valleys. Geology, 39(3), 283-286. https://doi.org/10.1130/g31631.1.

Stoker, M. S., Balson, P. S., Long, D., & Tappin, D. R. (2011). An overview of the lithostratigraphical framework for the Quaternary deposits on the United Kingdom continental shelf, British Geological Survey Research Report, RR/11/03. 48pp, http://nora.nerc.ac.uk/id/eprint/15939/1/RR11003.pdf

Sun, Q. L., Cartwright, J., Wu, S. G., & Chen, D. X. (2013). 3D seismic interpretation of dissolution pipes in the South China Sea: Genesis by subsurface, fluid induced collapse, Marine Geology, 337, 171-181. https://doi.org/10.1016/j.margeo.2013.03.002.

Tape, C., Liu, Q., Maggi, A., & Tromp, J. (2009). Adjoint tomography of the southern California crust. Science, 325(5943), 988-992. https://doi.org/10.1126/science.1175298.

Tary, J. B., Géli, L., Guennou, C., Henry, P., Sultan, N., Çağatay, N., & Vidal, V. (2012). Microevents produced by gas migration and expulsion at the seabed: a study based on sea bottom recordings from the Sea of Marmara. Geophysical Journal International, 190(2), 993-1007. https://doi.org/10.1111/j.1365-246X.2012.05533.x.

Taylor, P., Stahl, H., Vardy, M.E., Bull, J.M., Akhurst, M., Hauton, C., James, R.H., Lichtschlag, A., Long, D., Aleynik, D. & Toberman, M., 2015. A novel sub-seabed CO2 release experiment informing monitoring and impact assessment for geological carbon storage. International Journal of Greenhouse Gas Control, 38, pp.3-17. https://doi.org/10.1016/j.ijggc.2014.09.007.

Thomsen, L. (1995). Elastic anisotropy due to aligned cracks in porous rock1. Geophysical Prospecting, 43(6), 805-829. https://doi.org/10.1111/j.1365-2478.1995.tb00282.x.

Tóth, J. (1980). Cross-formational gravity-flow of groundwater: A mechanism of the transport and accumulation of petroleum (the generalized hydraulic theory of petroleum migration). Problems of Petroleum Migration, 121-167. https://doi.org/10.1306/St10411C8.

1887 Tóth, Z., Spiess, V., Mogollón, J. M., & Jensen, J. B. (2014). Estimating the free gas content in Baltic Sea sediments
1888   using compressional wave velocity from marine seismic data. Journal of Geophysical Research: Solid Earth,
1889   119(12), 8577-8593. https://doi.org/10.1002/2014JB010989.

1890 Tóth, Z., Spiess, V. & Keil, H. (2015). Frequency dependence in seismoacoustic imaging of shallow free gas due to
1891   gas bubble resonance, Journal of Geophysical Research: Solid Earth, 120, 8056–8072.
1892   https://doi.org/10.1002/2015JB012523.

1893 Tucker, P. M., & Yorston, H. J. (1973). Pitfalls in Seismic Interpretation, Geophysical Monograph Series, pp57.
1894   https://doi.org/10.1190/1.9781560802365.

1895 Vardy, M. E. (2015). Deriving shallow-water sediment properties using post-stack acoustic impedance inversion.
1896   Near Surface Geophysics, 13(2), 143-154. https://doi.org/10.3997/1873-0604.2014045.

1897 Vardy, M. E., Vanneste, M., Henstock, T. J., Clare, M. A., Forsberg, C. F., & Provenzano, G. (2017). State-of-the-
1898   art remote characterization of shallow marine sediments: the road to a fully integrated solution. Near Surface
1899   Geophysics, 15(4), 387-402. https://doi.org/10.3997/1873-0604.2017024.

1900 Varela, I., Nasser, M., Chapman, M. and Liu, E. (2006). Anisotropic azimuthal attenuation as an indicator of fracture
1901   properties, a case study on time-lapse walkaround VSP data. 68th EAGE Annual Conference and Technical
1902   Exhibition, Vienna, Paper P146. https://doi.org/10.3997/2214-4609.201402333.

1903 Virieux, J., and Operto, S. (2009). An overview of full-waveform inversion in exploration geophysics. Geophysics,
1904   74(6), WCC1-WCC26. https://doi.org/10.1190/1.3238367.

1905 Waage, M., Bünz, S., Landrø, M., Plaza-Faverola, A., & Waghorn, K. A. (2019). Repeatability of high-resolution
1906   3D seismic data. Geophysics, 84(1), B75-B94. https://doi.org/10.1190/geo2018-0099.1.

1907 Watson, T. L., & Bachu, S. (2009). Evaluation of the Potential for Gas and CO2 Leakage Along Wellbores. Society
1908   of Petroleum Engineers. https://doi.org/10.2118/106817-PA.

1909 Watts, G. F. T., Jizba, D., Gawith, D. E., & Gutteridge, P. (1996). Reservoir monitoring of the Magnus Field through
1910   4D time-lapse seismic analysis. Petroleum Geoscience, 2(4), 361-372. https://doi.org/10.1144/petgeo.2.4.361.

1911 Werner, U., & Shapiro, S. A. (1999). Frequency-dependent shear-wave splitting in thinly layered media with intrinsic
1912   anisotropy. Geophysics, 64(2), 604-608. https://doi.org/10.1190/1.1444567.

1913 White, J. E. (1975). Computed seismic speeds and attenuation in rocks with partial gas saturation. Geophysics, 40(2),
1914   224-232. https://doi.org/10.1190/1.1440520.

1915 White, R. S. (1977). Seismic bright spots in the Gulf of Oman. Earth and Planetary Science Letters, 37(1), 29–37.
1916   https://doi.org/10.1016/0012-821X(77)90143-1.

1917 Whiteside, W., Wang, B., Bondeson, H., & Li, Z. (2013). 3D imaging from 2D seismic data, an enhanced
1918   methodology. In SEG Technical Program Expanded Abstracts 2013 (pp. 3618-3622). Society of Exploration
1919   Geophysicists. http://dx.doi.org/10.1190/segam2013-1148.1.

1920 Whitesides, G. (2006) The origins and the future of microfluidics. Nature 442, 368–373.
1921   https://doi.org/10.1038/nature05058.

1922 Worthington, M.H. & Hudson, J.A. (2000). Fault properties from seismic Q, Geophysical Journal International, 143,
1923   937-944. https://doi.org/10.1046/j.1365-246X.2000.00315.x.

1924 Yao, H., van Der Hilst, R. D., & De Hoop, M. V. (2006). Surface-wave array tomography in SE Tibet from ambient
1925   seismic noise and two-station analysis—I. Phase velocity maps. Geophysical Journal International, 166(2), 732-
1926   744. https://doi.org/10.1111/j.1365-246X.2006.03028.x.

1927 Zelt, C. A., & Barton, P. J. (1998). Three-dimensional seismic refraction tomography: A comparison of two methods
1928   applied to data from the Faeroe Basin. Journal of Geophysical Research: Solid Earth, 103(B4), 7187–7210.
1929   https://doi.org/10.1029/97JB03536.

1930 Zelt, C. A., Sain, K., Naumenko, J. V., & Sawyer, D. S. (2003). Assessment of crustal velocity models using seismic
1931   refraction and reflection tomography. Geophysical Journal International, 153(3), 609-626.
1932   https://doi.org/10.1046/j.1365-246X.2003.01919.x